



Ministério da
**Ciência, Tecnologia
e Inovação**



sid.inpe.br/mtc-m21b/2014/09.03.12.43-TDI

THEORETICAL ANALYSIS OF DIFFUSION FLAME ESTABLISHED IN AN INERT POROUS MEDIUM

Max Akira Endo Kokubun

Doctorate Thesis Course Graduate
in Engineering and Space Technol-
ogy/Combustion and Propulsion,
guided by Dr. Fernando Fachini
Filho, approved in September 19,
2014.

URL of the original document:

<<http://urlib.net/8JMKD3MGP5W34M/3GUMQDH>>

INPE
São José dos Campos
2014

PUBLISHED BY:

Instituto Nacional de Pesquisas Espaciais - INPE

Gabinete do Diretor (GB)

Serviço de Informação e Documentação (SID)

Caixa Postal 515 - CEP 12.245-970

São José dos Campos - SP - Brasil

Tel.:(012) 3208-6923/6921

Fax: (012) 3208-6919

E-mail: pubtc@sid.inpe.br

BOARD OF PUBLISHING AND PRESERVATION OF INPE INTELLECTUAL PRODUCTION (RE/DIR-204):**Chairperson:**

Marciana Leite Ribeiro - Serviço de Informação e Documentação (SID)

Members:

Dr. Gerald Jean Francis Banon - Coordenação Observação da Terra (OBT)

Dr. Amauri Silva Montes - Coordenação Engenharia e Tecnologia Espaciais (ETE)

Dr. André de Castro Milone - Coordenação Ciências Espaciais e Atmosféricas (CEA)

Dr. Joaquim José Barroso de Castro - Centro de Tecnologias Espaciais (CTE)

Dr. Manoel Alonso Gan - Centro de Previsão de Tempo e Estudos Climáticos (CPT)

Dr^a Maria do Carmo de Andrade Nono - Conselho de Pós-Graduação

Dr. Plínio Carlos Alvalá - Centro de Ciência do Sistema Terrestre (CST)

DIGITAL LIBRARY:

Dr. Gerald Jean Francis Banon - Coordenação de Observação da Terra (OBT)

DOCUMENT REVIEW:

Maria Tereza Smith de Brito - Serviço de Informação e Documentação (SID)

Yolanda Ribeiro da Silva Souza - Serviço de Informação e Documentação (SID)

ELECTRONIC EDITING:

Maria Tereza Smith de Brito - Serviço de Informação e Documentação (SID)

André Luis Dias Fernandes - Serviço de Informação e Documentação (SID)



Ministério da
**Ciência, Tecnologia
e Inovação**



sid.inpe.br/mtc-m21b/2014/09.03.12.43-TDI

THEORETICAL ANALYSIS OF DIFFUSION FLAME ESTABLISHED IN AN INERT POROUS MEDIUM

Max Akira Endo Kokubun

Doctorate Thesis Course Graduate
in Engineering and Space Technol-
ogy/Combustion and Propulsion,
guided by Dr. Fernando Fachini
Filho, approved in September 19,
2014.

URL of the original document:

<<http://urlib.net/8JMKD3MGP5W34M/3GUMQDH>>

INPE
São José dos Campos
2014

Cataloging in Publication Data

Kokubun, Max Akira Endo.

K829t Theoretical analysis of diffusion flame established in an inert porous medium / Max Akira Endo Kokubun. – São José dos Campos : INPE, 2014.

xviii + 124 p. ; (sid.inpe.br/mtc-m21b/2014/09.03.12.43-TDI)

Thesis (Doctorate in Engineering and Space Technology/Combustion and Propulsion) – Instituto Nacional de Pesquisas Espaciais, São José dos Campos, 2014.

Guiding : Dr. Fernando Fachini Filho.

1. Diffusion flames 2. Porous materials 3. Liquid fuels
I.Título.

CDU 544.452



Esta obra foi licenciada sob uma Licença [Creative Commons Atribuição-NãoComercial 3.0 Não Adaptada](https://creativecommons.org/licenses/by-nc/3.0/).

This work is licensed under a [Creative Commons Attribution-NonCommercial 3.0 Unported License](https://creativecommons.org/licenses/by-nc/3.0/).

Aprovado (a) pela Banca Examinadora
em cumprimento ao requisito exigido para
obtenção do Título de **Doutor(a)** em
Engenharia e Tecnologia
Espaciais/Combustão e Propulsão

Dr. Fernando Fachini Filho



Presidente / Orientador(a) / INPE / Cachoeira Paulista - SP

Dr. Wladimir Mattos da Costa Dourado



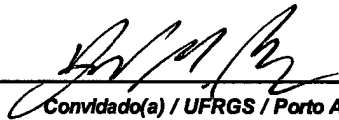
Membro da Banca / IAE/DCTA / São José dos Campos - SP

Dr. Marcio Teixeira de Mendonça



Membro da Banca / IAE/DCTA / SJCampos - SP

Dr. Fernando Marcelo Pereira



Convidado(a) / UFRGS / Porto Alegre - RS

Dr. Alexey Maylybaev



Convidado(a) / IMPA / Rio de Janeiro - RJ

Este trabalho foi aprovado por:

maioria simples

unanimidade

Aluno (a): **Max Akira Endo Kokubun**



São José dos Campos, 19 de Setembro de 2014

“The science of today is the technology of tomorrow.”

EDWARD TELLER

“Research is what I’m doing when I don’t know what I’m doing.”

WERNHER VON BRAUN

“Don’t believe a result unless you understand it.”

FORMAN A. WILLIAMS

ACKNOWLEDGEMENTS

This thesis could not be done without the help and support of some people. Particularly, I acknowledge the contribution of the following people:

Professors Márcio Teixeira Mendonça (IAE) and Fernando Marcelo Pereira (UFRGS), whom helped me greatly with the numerical method and with physical discussions regarding the problems treated in this thesis.

My colleagues and friends from LCP, who along the years were important in the everyday-life at INPE.

My family, that always taught me the importance of a good education.

My friends across Brazil and across the world, whom are fundamental part of my life, in good and in bad moments. “SEMPRE DE BOA”.

Professor Moshe Matalon, from the University of Illinois at Urbana-Champaign, whom welcomed me in his group during my stay in USA and with whom I’ve learned a lot regarding combustion theory. The results presented in the Appendix were obtained during my stay at Urbana-Champaign.

My advisor Fernando Fachini, whom along the five-years-period that I’ve stayed at INPE taught me and encouraged me in a field of research that I knew nothing.

At last, I thank with all my heart the patience, friendship and love of my girlfriend Grazi, who was by my side during most part of this long journey. Her support and companionship was essential to my life in the last years. This thesis is dedicated to her.

ABSTRACT

In this work we analyze a steady, planar diffusion flame established in an inert porous matrix. The geometry under consideration is a stagnation-point flow against a condensed (liquid) phase, with all the system (gas and liquid) immersed in an inert porous matrix. In order to better understand the coupled physical processes that occur in this confined problem, we divide the present work in three distinct, but closely related, parts. In the first part we analyze the frozen impinging flow against a hot, impermeable wall (the gas is confined in an inert porous matrix). This configuration allows us to study the heat transfer problem occurring inside the porous matrix. In the second part we replace the impermeable wall by a pool of liquid and analyze the steady vaporization regime that is established when the impinging flow is at a higher temperature than the liquid boiling temperature. In this case, the heat and mass transfer confined problem is analyzed. Then, in the third part we consider the impinging jet to be oxidant and the liquid to be fuel. By considering that the conditions are such that a diffusion flame is established, we analyze the influence of the porous matrix in the overall flame properties. Finally, in the Appendix we perform an asymptotic analysis of the extinction of a diffusion flame established in an inert porous chamber. This analysis is made in order to shed some light on how the gas-solid heat exchange modifies the extinction limits of such confined flames.

ANÁLISE TEÓRICA DE UMA CHAMA DIFUSIVA ESTABELECIDAE EM UM MEIO POROSO INERTE

RESUMO

Nesse trabalho, nós analisamos uma chama difusiva estacionária e plana, estabelecida dentro de uma matriz porosa inerte. A geometria considerada é a de um escoamento de ponto de estagnação contra uma fase líquida. Todo o sistema é considerado imerso na matriz porosa. Para que os processos físicos acoplados que ocorrem dentro da matriz porosa possam ser melhor compreendidos, o presente problema é dividido em três partes distintas, mas relacionadas. Na primeira parte, analisamos o escoamento congelado que impinge contra uma parede quente impermeável. O escoamento ocorre dentro da matriz porosa. Essa configuração nos permite estudar o problema de transferência de calor entre gás e sólido no do escoamento estabelecido dentro da matriz porosa inerte. Na segunda parte, substituímos a parede impermeável por uma piscina de líquido e analisamos o regime estacionário de evaporação que se estabelece quando o gás impingente está a uma temperatura maior do que a temperatura de ebulição do líquido. Nesse caso, os processos de transporte de massa e calor do problema confinado são analisados. Na terceira parte, consideramos que o jato impingente é oxidante e o líquido é combustível. Então, considerando que as condições são tais que uma chama difusiva é estabelecida, analisamos a influência da matriz porosa nas propriedades gerais da chama. No Apêndice, apresentamos uma análise assintótica da extinção de uma chama difusiva estabelecida dentro de uma câmara porosa. Essa análise foi realizada para que se possa elucidar como a interação térmica entre gás e sólido afeta os limites de extinção de tal chama confinada.

LIST OF FIGURES

	<u>Pág.</u>
1.1 Heat recirculation in a premixed flame established in an inert porous medium.	1
1.2 Chemical and thermal speed (S_F and S_T , respectively) in a porous tube.	2
1.3 Transport processes for diffusion flames established in porous media. . .	4
1.4 Problem analyzed by Raju and Tien.	5
1.5 Problem analyzed Chao <i>et al.</i>	6
1.6 Geometry of the present problem.	7
1.7 Diffusion flame established in a porous chamber.	9
2.1 Local (pore-level) problem.	12
2.2 Schematic of the REV approach	14
2.3 Schematic of the present problem.	18
2.4 Schematic of the bubble formation for increasing heat fluxes.	21
3.1 Schematic of the problem.	31
3.2 Vertical velocities with and without thermal expansion with $\beta^* = 1.08$, $Pr = \varphi = 0.7$, $N_g = 1.0$, $T_0 = \{1.6, 2.0, 10.0\}$ and $\Gamma = 50.0$	33
3.3 Horizontal velocities with and without thermal expansion with $\beta^* = 1.08$, $Pr = \varphi = 0.7$, $N_g = 1.0$, $T_0 = \{1.6, 2.0, 10.0\}$ and $\Gamma = 50.0$	34
3.4 Temperature profiles with and without thermal expansion with $\beta^* =$ 1.08 , $Pr = \varphi = 0.7$, $N_g = 1.0$, $T_0 = 1.6$ and $\Gamma = 50.0$	35
3.5 Pressure profiles with and without thermal expansion with $\beta^* = 1.08$, $Pr = \varphi = 0.7$, $N_g = 1.0$, $T_0 = 1.6$ and $\Gamma = 50.0$ $T_0 = 1.6$	36
3.6 Velocity overshoot for different porosities and with $\beta^* = 1.08$, $Pr = 0.7$, $N_g = 1.0$, $T_0 = 1.6$ and $\Gamma = 50.0$ $T_0 = 1.6$	37
3.7 Temperatures difference with and without thermal expansion with $\beta^* =$ 1.08 , $Pr = \varphi = 0.7$, $N_g = 1.0$, $T_0 = 1.6$ and $\Gamma = 50.0$	38
3.8 Pressure profiles for $\varphi = 0.3$ with $\beta^* = 1.08$, $Pr = 0.7$, $N_g = 1.0$, $T_0 = 1.6$ and $\Gamma = 50.0$	39
3.9 Wall shear \times wall temperature, for different porosities with $\beta^* = 1.08$, $Pr = 0.7$, $N_g = 1.0$ and $\Gamma = 50.0$	40
3.10 Heat transfer at the wall \times wall temperature, for different porosities with $\beta^* = 1.08$, $Pr = 0.7$, $N_g = 1.0$ and $\Gamma = 50.0$	41
3.11 Heat transfer at the wall \times porosity, for different wall temperatures with $\beta^* = 1.08$, $Pr = 0.7$, $N_g = 1.0$ and $\Gamma = 50.0$	42

3.12	Wall shear \times porosity, for different wall temperatures with $\beta^* = 1.08$, $Pr = 0.7$, $N_g = 1.0$ and $\Gamma = 50.0$	43
3.13	Heat transfer at the wall $\times N_g$ with $\beta^* = 1.08$, $Pr = 0.7$, $\varphi = 0.7$, $T_0 = 1.6$ and $\Gamma = 50.0$	44
3.14	Temperature difference for $N_g = 1.0$ and $N_g = 5.0$ with $\beta^* = 1.08$, $Pr = \varphi = 0.7$, $T_0 = 1.6$ and $\Gamma = 50.0$	45
3.15	Heat transfer at the wall $\times \Gamma$ with $\beta^* = 1.08$, $Pr = \varphi = 0.7$, $N_g = 1.0$ and $T_0 = 1.6$	46
3.16	$\eta_{TBL} \times (1 - \varphi)$ with $\beta^* = 1.08$, $Pr = 0.7$, $N_g = 1.0$, $T_0 = 1.6$ and $\Gamma = 50.0$	46
4.1	Schematic of the problem.	49
4.2	Temperature profiles with and without thermal expansion for $\beta^* = 1.08$, $N_g = N_l = L_F = 1.0$, $Pr = \varphi = 0.7$, $\Gamma = 50.0$ and $T_B = 0.333$	54
4.3	Velocities profiles with and without thermal expansion for $\beta^* = 1.08$, $N_g = N_l = L_F = 1.0$, $Pr = \varphi = 0.7$, $\Gamma = 50.0$ and $T_B = 0.333$	55
4.4	Vapor mass fraction profiles with and without thermal expansion for $\beta^* = 1.08$, $N_g = N_l = L_F = 1.0$, $Pr = \varphi = 0.7$, $\Gamma = 50.0$ and $T_B = 0.333$	56
4.5	$\{\dot{m}, Y_{F0}\} \times N_l$ with $\beta^* = 1.08$, $N_g = L_F = 1.0$, $Pr = \varphi = 0.7$, $\Gamma = 50.0$ and $T_B = 0.333$	57
4.6	Temperature profiles for $N_l = \{1.0, 100.0\}$, with $\beta^* = 1.08$, $N_g = L_F =$ 1.0 , $Pr = \varphi = 0.7$, $\Gamma = 50.0$ and $T_B = 0.333$	58
4.7	$\{\dot{m}, T_{s0}, Y_{F0}\} \times \varphi$, with $\beta^* = 1.08$, $N_g = N_l = L_F = 1.0$, $Pr = 0.7$, $\Gamma = 50.0$ and $T_B = 0.333$	59
4.8	$\{Q_g, Q_s\} \times \varphi$, with $\beta^* = 1.08$, $N_g = N_l = L_F = 1.0$, $Pr = 0.7$, $\Gamma = 50.0$ and $T_B = 0.333$	60
4.9	$\{\dot{m}, T_{s0}, Y_{F0}\} \times (1 - T_B)$, with $\beta^* = 1.08$, $N_g = N_l = L_F = 1.0$, $Pr =$ $\varphi = 0.7$ and $\Gamma = 50.0$	61
4.10	$\{\dot{m}, T_{s0}, Y_{F0}\} \times \Gamma$, with $\beta^* = 1.08$, $N_g = N_l = L_F = 1.0$, $Pr = \varphi = 0.7$ and $T_B = 0.333$	62
4.11	$\{Q_g, Q_s\} \times \Gamma$, with $\beta^* = 1.08$, $N_g = N_l = L_F = 1.0$, $Pr = \varphi = 0.7$ and $T_B = 0.333$	63
4.12	$\{\dot{m}, T_{s0}, Y_{F0}\} \times N_g$, with $\beta^* = 1.08$, $N_l = L_F = 1.0$, $Pr = \varphi = 0.7$, $T_B = 0.333$ and $\Gamma = 50.0$	64
4.13	$\{Q_g, Q_s\} \times N_g$ with $\beta^* = 1.08$, $N_l = L_F = 1.0$, $Pr = \varphi = 0.7$, $T_B = 0.333$ and $\Gamma = 50.0$	65
4.14	$Y_{F0} \times L_F$, with $\beta^* = 1.08$, $N_g = N_l = 1.0$, $Pr = \varphi = 0.7$, $T_B = 0.333$ and $\Gamma = 50.0$	66
5.1	Schematic of the present problem.	70

5.2	Temperature and mass fraction profiles for $\beta^* = 1.08$, $N_g = N_l = L_F = L_O = 1.0$, $l = 4.32$, $\phi = 8.0$, $Pr = \varphi = 0.7$, $q = 100.0$, $Da = 10^7$, $\Gamma = 50.0$ and $T_B = 2.5$	74
5.3	Velocities profiles for $\beta^* = 1.08$, $N_g = N_l = L_F = L_O = 1.0$, $l = 4.32$, $\phi = 8.0$, $Pr = \varphi = 0.7$, $q = 100.0$, $Da = 10^7$, $\Gamma = 50.0$ and $T_B = 2.5$	75
5.4	Velocities profiles for $\varphi = \{0.5, 0.7, 1.0\}$ and $\beta^* = 1.08$, $N_g = N_l = L_F = L_O = 1.0$, $l = 4.32$, $\phi = 8.0$, $Pr = 0.7$, $q = 100.0$, $Da = 10^7$, $\Gamma = 50.0$ and $T_B = 2.5$	76
5.5	Velocity profile and Darcy resistance for $\varphi = 0.7$, $\beta^* = 1.08$, $N_g = N_l = L_F = L_O = 1.0$, $l = 4.32$, $\phi = 8.0$, $Pr = 0.7$, $q = 100.0$, $Da = 10^7$, $\Gamma = 50.0$ and $T_B = 2.5$	77
5.6	Darcy resistance \times porosity, for $\beta^* = 1.08$, $N_g = N_l = L_F = L_O = 1.0$, $l = 4.32$, $\phi = 8.0$, $Pr = 0.7$, $q = 100.0$, $Da = 10^7$, $\Gamma = 50.0$ and $T_B = 2.5$	78
5.7	Flame position and stagnation-point position $\times \varphi$ for $\beta^* = 1.08$, $N_g = N_l = L_F = L_O = 1.0$, $l = 4.32$, $\phi = 8.0$, $Pr = 0.7$, $q = 100.0$, $Da = 10^7$, $\Gamma = 50.0$ and $T_B = 2.5$	79
5.8	Temperature and mass fraction profiles for $\varphi = \{0.5, 1.0\}$ and $\beta^* = 1.08$, $N_g = N_l = L_F = L_O = 1.0$, $l = 4.32$, $\phi = 8.0$, $Pr = 0.7$, $q = 100.0$, $Da = 10^7$, $\Gamma = 50.0$ and $T_B = 2.5$	80
5.9	$\{T_f, \dot{m}\} \times \varphi$ for $\beta^* = 1.08$, $N_g = N_l = L_F = L_O = 1.0$, $l = 4.32$, $\phi = 8.0$, $Pr = 0.7$, $q = 100.0$, $Da = 10^7$, $\Gamma = 50.0$ and $T_B = 2.5$	81
5.10	$\{Q_g, Q_s\} \times \varphi$ for $\beta^* = 1.08$, $N_g = N_l = L_F = L_O = 1.0$, $l = 4.32$, $\phi = 8.0$, $Pr = 0.7$, $q = 100.0$, $Da = 10^7$, $\Gamma = 50.0$ and $T_B = 2.5$	82
5.11	Expected variations of flame temperature and vaporization rate with respect to the porosity φ	83
A.1	Schematic of the present problem.	97
A.2	Representative profiles in the two length-scales.	100
A.3	Temperature profiles in the far field.	114
A.4	Profiles in the consumption zone.	115
A.5	Porosity influence.	116
A.6	$\{N, K\} \times \varphi$	117
A.7	$\{T_f, T_f^g, T_{sf}\} \times \bar{V}$	119
A.8	Reactants leakage $\times \varphi$ for $\bar{V} = 20, 100, 500 \text{ mm/s}$	120
A.9	$\{\gamma, \eta_f\} \times \varphi$ for $\bar{V} = 20, 100, 500 \text{ mm/s}$	121
A.10	$\{T_f, D\} \times \bar{V}$ for $\varphi = 0.7$	122
A.11	Reactants leakage $\times N^{1/(m'-1)}$	122
A.12	$\{\gamma, \eta_f\} \times N^{1/(m'-1)}$	123
A.13	Low-velocity extinction points.	123

A.14 High-velocity extinction points for $N^{1/(m'-1)}$ 124

CONTENTS

	<u>Pág.</u>
1 INTRODUCTION	1
2 MATHEMATICAL FORMULATION	11
2.1 General conservation equations and the local-average method	11
2.2 Semi-heuristic formulation	16
2.3 Formulation for the present work	17
2.3.1 Variable change and non-dimensional formulation	22
2.3.2 Numerical method	26
2.4 Physical discussion	26
3 HEAT AND MOMENTUM TRANSFER PROBLEM: STAGNATION-POINT FLOW AGAINST AN IMPERME- ABLE WALL	29
3.1 Physical problem	30
3.2 Mathematical formulation	32
3.3 Results	33
3.4 Conclusions	41
4 PHASE CHANGE PROBLEM: STAGNATION-POINT FLOW AGAINST A LIQUID POOL	47
4.1 Physical problem	49
4.2 Mathematical formulation	50
4.2.1 Liquid-solid region	52
4.3 Results	53
4.4 Conclusions	59
5 REACTIVE PROBLEM: DIFFUSION FLAME ESTABLISHED IN A STAGNATION-POINT FLOW CONFIGURATION	67
5.1 Physical problem	69
5.2 Mathematical formulation	71
5.3 Results	73
5.4 Conclusions	81
6 CONCLUSIONS	85

6.1	Future works	87
	REFERENCES	89
	APPENDIX A: ASYMPTOTIC ANALYSIS OF EXTINCTION OF A DIFFUSION FLAME IN A POROUS CHAMBER	97
A.1	Mathematical formulation	98
A.2	Far-field, convective region	104
A.3	Convective-diffusive region	106
A.4	Burke-Schumann limit	113
A.5	Reactant leakage curves	116
A.6	Conclusions	120

1 INTRODUCTION

Since the work of [Takeno and Sato \(1979\)](#), in which they applied Weinberg's pioneering idea of heat recirculation ([WEINBERG, 1971](#)), combustion in porous media has attracted much attention from scientists and engineers. Applications ranging from compact combustion chambers, food baking, drying of paper and wood ([HOWELL et al., 1996](#); [MUJEEBU et al., 2010](#)), heavy-oil thermal recovery ([BRANCH, 1979](#); [ALI, 2003](#); [CASTANIER; BRIGHAM, 2003](#); [AKKUTLU; YORTSOS, 2003](#); [MAILYBAEV et al., 2011](#)), stability of solid propellants decomposition ([TELENGATOR et al., 2000](#)) and attenuation of detonations ([RADULESCU; MAXWELL, 2011](#)) are some examples of the wide range of possibilities for combustion in porous media. The heat recirculation caused by the solid-phase conduction ([BARRA; ELLZEY, 2004](#)) enhances the pre-heating of reactants, which may lead to an increase in the flame temperature and the possibility of burning ultra-lean mixtures for premixed flames ([WOOD; HARRIS, 2008](#); [PEREIRA et al., 2010](#)). It has been shown also that when an impinging premixed flame is established in an inert porous medium, stretch may extend the low flammability limit even further ([KOKUBUN et al., 2013](#)), a result opposed to what is observed for free flames. In [Fig. 1.1](#) a schematic of the heat recirculation feature present in premixed flames propagating in inert porous media is shown.

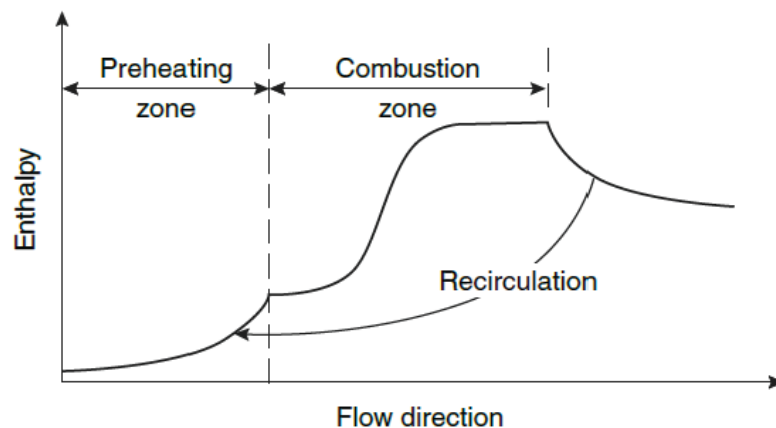


Figure 1.1 - Heat recirculation in a premixed flame established in an inert porous medium. SOURCE: [Vafai \(2005\)](#)

The increase on the flame temperature due to pre-heating of reactants leads to an increase on the flame speed, because of the exponential dependence of the flame speed

with the flame temperature, as flame structure analyses show (YARIN; SUKHOV, 1992; KAKUTKINA, 2006; LAEVSKII; BABKIN, 2008; PEREIRA et al., 2009). If the constant flame speed is different from the constant flow speed, there is a speed associated with the heating of the solid, i.e., thermal speed. When the flame speed and the thermal speed have the same constant value, the superadiabatic effect (flame temperature above the adiabatic value) is maximum because these processes sustain each other. If the problem is stationary or if the characteristic time of the thermal speed is very short, the solid is considered to be instantaneously heated in the flame propagation time scale. A schematic of the propagating processes is shown in Fig. 1.2 for an idealized planar, adiabatic premixed flame propagating in an infinitely long porous tube ¹.

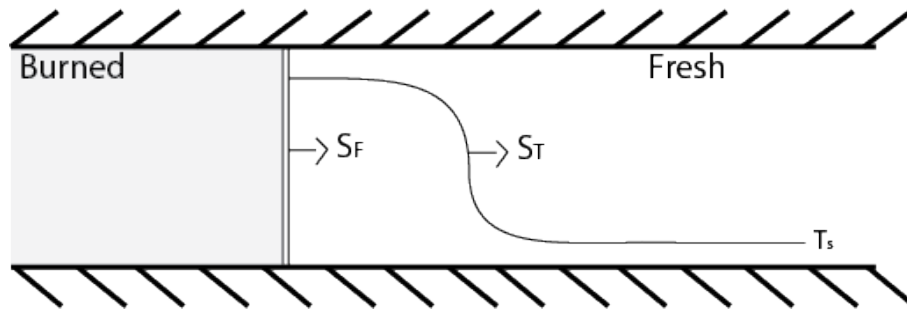


Figure 1.2 - Chemical and thermal speed (S_F and S_T , respectively) in a porous tube.

An interesting effect is observed if the flame speed is small, or if the thermal speed is faster than the flame speed: in those cases, the flame temperature may be lower than the adiabatic value, i.e., subadiabatic combustion occurs (ZHDANOK et al., 1995). In a more general way, subadiabatic flame temperatures may be achieved when the balance between heat release, recirculation and loss does not favor heat recirculation (here, heat loss means any heat not recovered by the reactants). Burning in low flame temperatures may be desirable because of the possibility of lowering emissions of pollutants and nocive compounds (one must carefully weight this feature with the possibility of unburned fuel passing through the flame, which may form soot). Extinction is shown to occur if the velocity is small enough, because in this case the flame heat-losses are high (ROY et al., 2014).

¹Flames propagating in tubes are not planar, as they suffer the effects of viscosity near the wall. Even though the porous tube homogenizes the flow up to some extent, the flame is still curved. The curvature of the flame front induces a myriad of physical effects, such as an increase on the burning rate and usually there is the development of instabilities.

When it comes to nonpremixed combustion in porous media, the literature is not vast as for premixed flames. The first attempts on modelling liquid fuel burning in porous media focused on droplet injection inside the solid matrix (TSENG; HOWELL, 1996). For burning of liquid fuels, the intense radiation field generated by the heated solid enhances the evaporation of fuel droplets in the confined medium. For situations such that the droplets vaporize and mix with oxidant prior to the combustion zone (MARTYNENKO et al., 1998; KAYAL; CHAKRAVARTY, 2005), essentially a premixed flame is established. Liquid-fuel-fired porous burners (non-spraying) were proposed as a way of burning liquid fuels without resorting to injection nozzles (which are energy-consuming) (JUJGAI et al., 2002; JUJGAI; POLMART, 2003; JUGJAI; PONGSAI, 2007). Such burners have the advantage of compactness and efficiency when compared to the usual spray configuration. Low emissions of pollutants are also described for such burners.

One of the reasons of the low pollutant emission is the possibility of burning contents at low temperatures, when compared to free flames. In non-premixed (diffusion) flames, this happens because the porous matrix redistributes the heat from the flame to the surroundings, as shown in Fig. 1.3, where a schematic of the transport processes that occur in a diffusion flame established in an inert porous medium is presented. In a premixed flame the heat removed from the reaction region is recirculated to the fresh gases (unburned) region, which increases the temperature of the incoming reactants. This increase on the reactants temperature increases the flame temperature, which consequently increase its speed. Then, if one wishes to keep the flame at a stationary position, one must increase the mass flux of reactants. This process enhances the input power to the reaction region, which then increases the flame temperature (PEREIRA et al., 2009; PEREIRA et al., 2010; PEREIRA et al., 2011), except when the flame speed is very low or when the thermal speed is fast when compared to the flame speed (in that case, subadiabatic temperatures may be achieved). In a non-premixed flame, mass diffusion of reactants towards the flame sheet is the rate-controlling physical process (in contrast to the reactants mass flux in premixed flames) and no thermal speed exist because there is no flame-front propagation. Then, even though the incoming reactants are heated (increase of the mass flux towards the sheet), the heat distributed by the porous matrix may cool the flame, lowering its temperature. If the heat exchange between gas and solid is high enough, this heat distribution may extinguish the flame. When a one-equation formulation is considered (local thermal equilibrium between gas and solid phases), such lowering in the flame temperature is attributed to a high value of the effective Lewis number (CHAO et al., 1994), which makes heat extraction from the flame more

intense than mass reactants transport to the flame sheet. The effective Lewis number is considered as the ratio between the effective thermal diffusivity and the mass diffusivity. Since the effective thermal diffusivity is the sum of the gas and solid thermal diffusivities, the effective Lewis number is usually high.

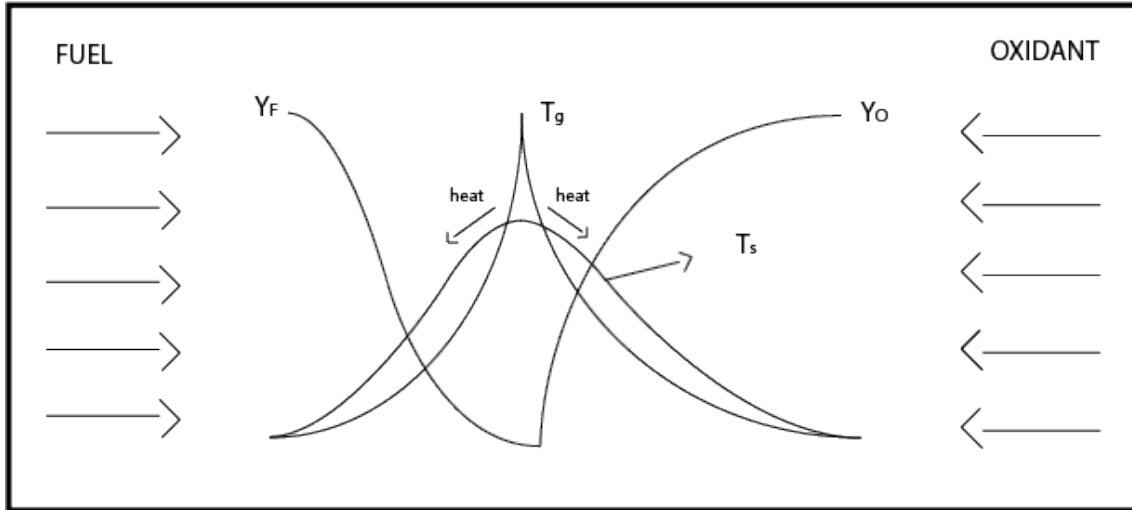


Figure 1.3 - Transport processes for diffusion flames established in porous media.

The difficulty in having optical access inside porous material makes it a challenge to obtain experimental measurements. One can insert a thermocouple inside the matrix if the porous material is carefully constructed, however, it is impossible to distinguish between gas and solid temperature profiles because the thermocouple will measure an average temperature. Some works have used laser measurements, also depending on a carefully constructed porous matrix, but in these works only the gas temperature could be measured (STELZNER et al., 2014). Indirect measurements as combustion products emission and overall temperature profiles are usually made (MITAL et al., 1997; JUJGAI et al., 2002; JUJGAI; POLMART, 2003; KAMAL; MOHAMAD, 2006; JUGJAI; PONGSAI, 2007) in experimental works. In this scenario, theoretical works are important in order to better understand the confined physical processes, to shed some light on the results that are obtained experimentally and to even provide guidance to future experiments.

Raju and T'ien (2007) studied a one-dimensional stagnation-point diffusion flame established next to a porous wick filled with liquid fuel, as depicted in Fig. 1.4. They analyzed the heat and mass transport processes inside the wetted wick. The

diffusion flame imposes a heat flux towards the porous wick, which then is used on the liquid-fuel phase change. Conceptually, two regimes may exist in the porous wick: funicular, in which a two-phase vapor-liquid region exist above a purely liquid region, and evaporative, in which a single phase vapor region exist, followed by the two-phase region above the purely liquid fuel region. Intuitively, the evaporative regime must occur for high heat fluxes. It has been shown that this regime is unstable (ZHAO; LIAO, 2000). Also, in their work, Raju and T'ien (2007) showed that some fraction of liquid vapor that does not goes to combustion condensates inside the porous wick, creating a liquid-vapor counterflow right below the wick surface. This happens because they considered liquid ethanol. Since their focus was on the transport processes in the two-phase region, a confined flame was not considered.

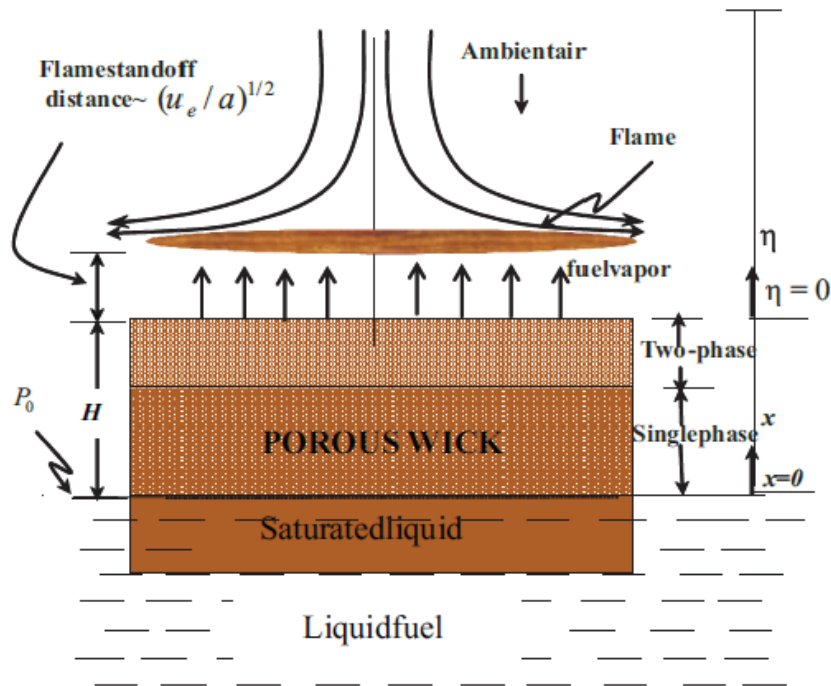


Figure 1.4 - Problem analyzed by Raju and Tien.
SOURCE: Raju and T'ien (2007)

Chao et al. (1994) analyzed the problem of a free-convective flame sheet established in a porous medium, as shown in Fig. 1.5. The condensed phase was not confined, but the gas phase was inside an inert porous matrix. In this case, the flow in the gas-solid region was governed by the Darcy equation with a buoyancy term. Local thermal

equilibrium was considered, such that a one-equation model was used. They showed, by using an infinitely thin flame sheet approximation, that the flame temperature is reduced due to the high value of the effective Lewis number, which takes into account the thermal conductivity of the solid as well as the gas thermal conductivity. An interesting result obtained by the authors was that when the gas density and viscosity were allowed to vary in such a way that $\bar{\rho}\bar{\mu} = \text{constant}$, the velocity presents a minimum at the flame-sheet, rather than a maximum, as in non-confined problems. They argued that this was a result of the competition between the Darcy term (which is a resistance force to the flow) and the buoyancy term (which increases velocity due to thermal expansion). When density and viscosity were considered as constants, no such effect was observed.

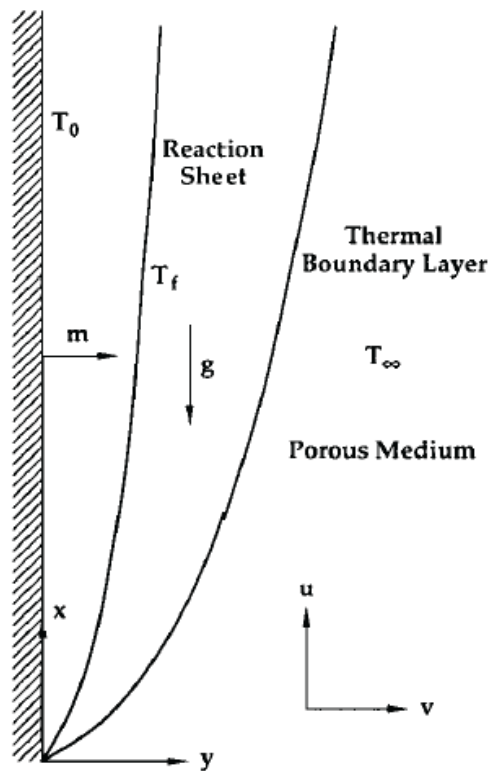


Figure 1.5 - Problem analyzed by Chao *et al.*
SOURCE: Chao *et al.* (1994)

More than just the distinct geometries in Raju and Tien and Chao *et al* works, an important difference was that the former considered the condensed phase to be confined (inside the porous matrix) and the flame not, while the latter considered the

opposite, i.e., a confined flame and a non-confined condensed phase. In the present work, we consider both gas and liquid to be immersed in an inert porous matrix. The configuration is that of Raju and Tien's work: a stagnation-point flow against a condensed phase, but with a confined flame as well. In Fig. 1.6 we present a schematic of the configuration to be studied. The coupling between the physical processes that occur in the confined medium render new features to the problem, when compared to the non-confined case (no porous matrix). With the use of a non-Darcean model for the flow and a local thermal non-equilibrium model for the energy equations, we analyze how the fluid-solid interaction modifies the physical features of such flames.

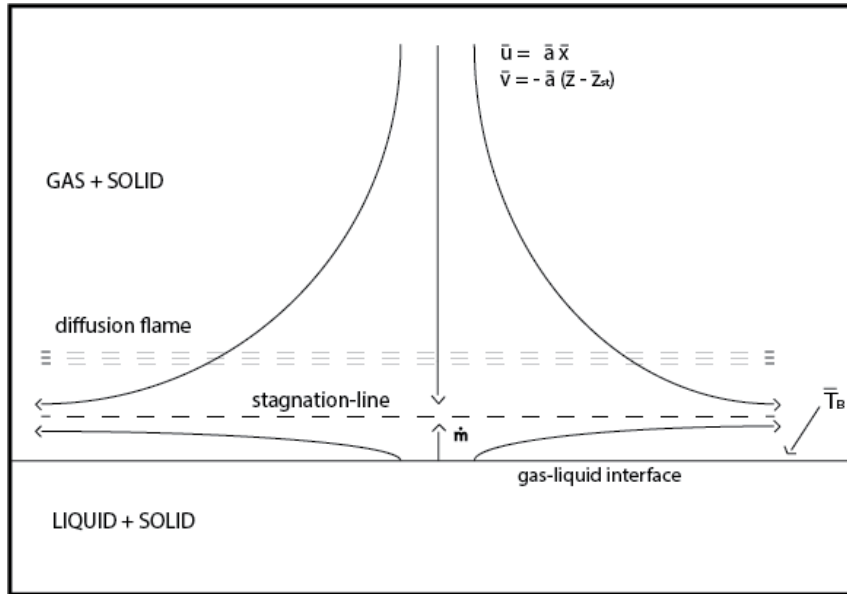


Figure 1.6 - Geometry of the present problem.

We divide the present problem in three parts in order to obtain a more clear physical understanding. In the first part we consider a stagnation-point, non-reactive, flow established in a porous medium against an impermeable hot wall. Under such conditions, we are interested in observe the heat transfer process in a confined medium. In the second part we replace the impermeable wall by a liquid pool immersed in a porous matrix, with the injected gas being at a high temperature. This configuration allows to analyze the heat and mass transfer (phase change) problem and it may be viewed as a frozen flow case. Then, in the third part we consider the liquid to be fuel and the incoming jet to be oxidant such that a diffusion flame is established. In

this third configuration we are able to study heat and mass transfer in reacting flows inside an inert porous medium. Therefore, the division of the problem in three parts allows for a deeper level of physical insight into the coupled processes that occur in the presence of the inert porous matrix. In each Chapter we present a specific introduction and physical discussion.

In the context of an incompressible flow (constant-density) and in the limit of an asymptotically large solid-to-gas thermal conductivities ratio (defined as $\Gamma \equiv \bar{\lambda}_s/\bar{\lambda}_g \gg 1$), these three problems were analyzed previously (KOKUBUN; FACHINI, 2011; KOKUBUN; FACHINI, 2012; KOKUBUN; FACHINI, 2013). In those cases, a Darcy flow was considered to be the leading-order flow equation and thermal equilibrium between phases was admitted for the leading-order temperature equations. The consideration of an asymptotically large Γ leads to well separated length-scales due to the very large difference between the phases thermal conductivities. Then, in those cases, analytical profiles were obtained in each length-scale and matched in order to build the complete solution for each problem. Despite some minor changes in the assumptions made, the present work can be viewed as a natural extension of these previous works. The consideration of variables fluid properties is more realistic and allow us to obtain a clearer picture of the physical processes that occur in these confined problems, while the consideration of general values of Γ allow us to assess more precisely the influence of the solid-to-gas thermal conductivities ratio on the overall aspects of each problem. For instance, for the case where we consider a stagnation-point against an impermeable wall, thermal expansion greatly modifies wall properties, which are of interest of Engineering, such as wall shear and wall heat flux. Consideration of thermal expansion (coupling between flow and energy equations) and general values of Γ demands a numerical solution for the present problem.

Since the three problems to be considered are closely related, their mathematical formulations are similar. In the next Chapter we develop the complete mathematical formulation (dimensional and non-dimensional) to be used in this work. Then, in the subsequent Chapters the appropriate formulation for each problem is given and their solutions are obtained and discussed.

In Appendix A we present an asymptotic analysis of the extinction limits of a diffusion flame in a porous chamber. The geometry studied is shown in Fig. 1.7. The general asymptotic formulation derived by Cheatham and Matalon (2000) for diffusion flames applicable to this case is used. This analysis is made in order to clarify how

the heat exchange between gas and solid lowers the flame temperature in the non-premixed configuration, a characteristic that eventually leads to flame extinction. Particularly, the asymptotic analysis identifies two distinct extinction points for the injection velocity, one associated with kinetic extinction, and the other associated with a high heat removal through the solid-phase (high gas-solid heat exchange). This dual-point extinction behavior was recognized previously in the literature and it was associated with heat losses (MATALON et al., 1979; MATALON; LUDFORD, 1979; CHAO; LAW, 1993; WANG et al., 2007).

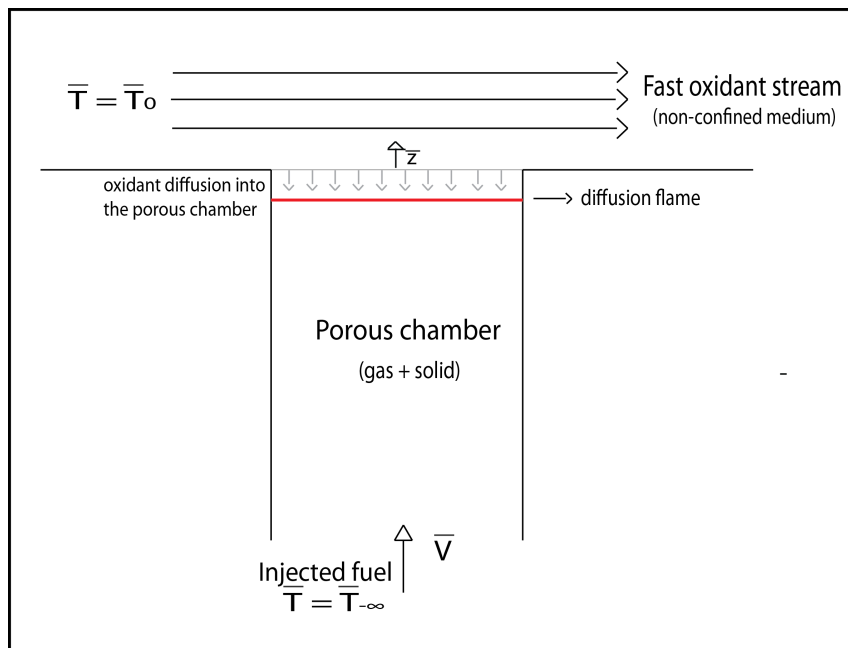


Figure 1.7 - Diffusion flame established in a porous chamber.

2 MATHEMATICAL FORMULATION

In this Chapter we present the mathematical formulation to be used in this work. The fundamental equations in the pore-scale (with the usual simplifications) are first presented and the difficulties that arise in solving the complete problem are exhibited. Then, the local-average procedure is briefly explained, and in the light of such, the semi-heuristic formulation is shown. At last, the further simplifications made in order to study the present problem are stated and the general formulation is given.

The notation used is defined right after its first appearance. Throughout this manuscript some symbols are repeated, but they should be clear from the context, such that no confusion is expected.

2.1 General conservation equations and the local-average method

The conservation equations that govern the behavior of reactive flows are well-established (WILLIAMS, 1985). In the presence of a porous matrix, these governing equations are still valid at the pore-scale, but the energy equation in the solid phase must be taken into account. At the interface between fluid and solid a diversity of effects occurs, such as heat exchange, elimination of radicals, viscous attachment, etc.

Consider the local (pore-level) problem as shown in Fig. 2.1.

In Fig. 2.1 A_{gs} is the surface area between fluid and solid and $\dot{w}_{r,i}$ is a source/sink of chemical species. Also, the solid phase is chemically inert and impermeable to the fluid phase.

The simplifications to be made are the following: low-Mach number (deflagration limit), neglect of Soret and Dufour effects (mass diffusion due to temperature gradient and energy flux due to mass gradient, respectively), a dilute mixture (with an inert gas as the abundant specie), Fourier law for the gas-phase heat-flux, negligible radiation from the gas-phase, Fick's law for mass diffusion, neglect of body forces and constant solid-phase properties. Then, the conservation equations governing this local stationary problem are given by

$$\nabla \cdot (\bar{\rho}_g \bar{\mathbf{u}}) = 0, \quad (2.1)$$

$$\bar{\rho}_g \bar{\mathbf{u}} \cdot \nabla \bar{\mathbf{u}} = -\nabla \bar{p} + \nabla \cdot \sigma, \quad (2.2)$$

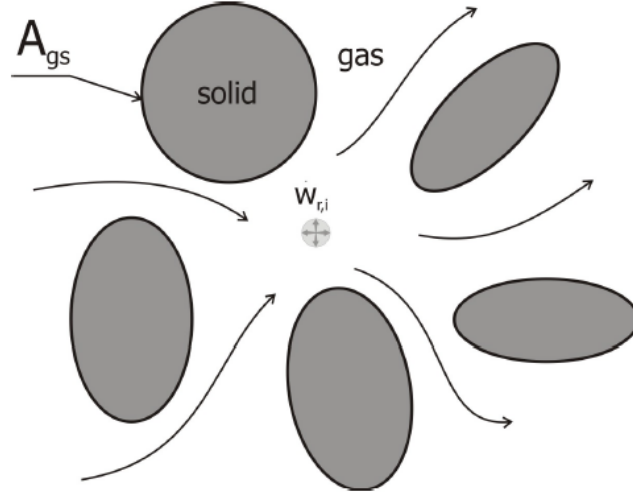


Figure 2.1 - Local (pore-level) problem.
SOURCE: Pereira (2009)

$$\bar{\rho}_g \bar{\mathbf{u}} \cdot \nabla Y_i = \nabla \cdot (\bar{\rho}_g \bar{D}_i \nabla Y_i) + \dot{w}_{r,i}, \quad (2.3)$$

$$(\bar{\rho} c_p)_g \bar{\mathbf{u}} \cdot \nabla \bar{T}_g = \nabla \cdot (\bar{\lambda}_g \nabla \bar{T}_g) - \sum_{i=1}^{N_s} h_i \dot{w}_{r,i}, \quad (2.4)$$

$$0 = \bar{\lambda}_s \nabla^2 \bar{T}_s, \quad (2.5)$$

where $\bar{\rho}_g$ is the fluid density, $\bar{\mathbf{u}}$ is the fluid velocity, \bar{p} is the fluid pressure, σ is the stress tensor, Y_i is the i -specie mass fraction, \bar{D}_i is the i -specie mass diffusion coefficient, c_p is the fluid specific heat at constant pressure, \bar{T}_g is the fluid temperature, $\bar{\lambda}_g$ is the fluid thermal conductivity, h_i is i -specie enthalpy of formation, $\bar{\lambda}_s$ is the solid thermal conductivity and \bar{T}_s is the solid temperature.

If we consider a perfect gas, the state equation is given by

$$\bar{p} = \frac{R}{M} \bar{\rho}_g \bar{T}_g, \quad (2.6)$$

where R is the universal gas constant and M is the molecular weight (assumed constant).

Boundary conditions to be applied at the fluid-solid interface A_{gs} are: (1) impermeable solid with no surface reactions (neglect of radical elimination at the wall ¹)

¹For combustion problems, elimination of radicals at the wall is important, even when an inert

and no-slip conditions

$$-\bar{\rho}_g \bar{D}_i \nabla Y_i = 0 \quad \text{and} \quad \bar{\mathbf{u}} = 0, \quad (2.7)$$

and (2) continuity of temperature and heat flux

$$\bar{T}_g = \bar{T}_s, \quad \text{and} \quad \bar{\lambda}_g \nabla \bar{T}_g \cdot \hat{n}_{gs} = (-\bar{\lambda}_s \nabla \bar{T}_s - \dot{\mathbf{q}}_{r,s}) \cdot \hat{n}_{gs}, \quad (2.8)$$

where \hat{n}_{gs} is the unitary normal vector on A_{gs} pointing to the solid-phase and $\dot{\mathbf{q}}_{r,s}$ is the radiant heat flux at the solid surface, that is due to the radiation exchange between solid surfaces. The equality of fluid-solid temperatures at the surface is justified by the zero-velocity boundary condition at the pore walls.

A priori, one can solve the above set of equations and account for the solid-fluid interaction at the pore walls. However, with the exception of the consideration of simple geometries, this task demands an enormous computational effort. In this case, a Direct Numerical Simulation (DNS) must be performed.

The DNS approach becomes unpractical for most cases because of the small-scale processes imposed by the pores. Then, the method more frequently utilized is the application of the volume averaging, in which we obtain a set of conservation equations averaged over certain representative volume containing both fluid and solid phases. In this method, the conservation equations are averaged over some representative elementary volume (REV), or, the smallest volume that represents the local average properties, such that addition of more pores in this volume does not change the system properties.

Consider Fig. 2.2.

The idea of the method is to average the property of interest in the REV, using the local coordinate system \vec{y} (microscopic coordinate), and to relate the result to the general coordinate system \vec{x} (macroscopic coordinate).

The volume average of a property ϕ is defined as (KAVIANY, 1995)

$$\langle \phi \rangle = \frac{1}{V} \int_V \phi dV, \quad (2.9)$$

medium is considered, as they may lower the reaction rate and have a direct influence on the overall flame properties. Since in the present problem we consider a single-step mechanism, radicals play no role, such that this effect may be ignored.

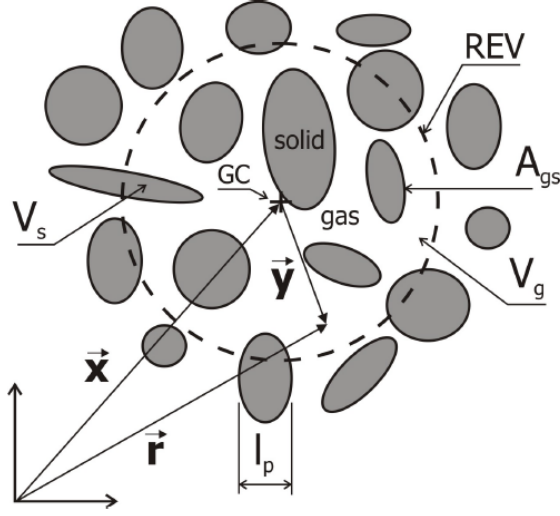


Figure 2.2 - Schematic of the REV approach
SOURCE: Pereira (2009)

where V is the volume of the REV. Then, the average of a gas-phase property ϕ_g over the gas-phase volume (gas-phase intrinsic volume average) is

$$\langle \phi_g \rangle^g = \frac{1}{V_g} \int_{V_g} \phi_g dV = \langle \phi_g \rangle / \varphi. \quad (2.10)$$

Where $\varphi \equiv V_g / (V_g + V_s)$ is the porosity, or the void volume, ranging from 0 to 1.

The theorem of the intrinsic volume-averaging of the gradient of a function ϕ_g is (KAVIANY, 1995)

$$\langle \nabla \phi_g \rangle^g = \nabla \langle \phi_g \rangle^g + \frac{1}{V_g} \int_{A_{gs}} \phi_g dA. \quad (2.11)$$

Analogously, the theorem of the intrinsic volume-averaging of the divergent of a vector \mathbf{b}_g is

$$\langle \nabla \cdot \mathbf{b}_g \rangle^g = \nabla \cdot \langle \mathbf{b}_g \rangle^g + \frac{1}{V_g} \int_{A_{gs}} \mathbf{b}_g \cdot \hat{n}_{gs} dA. \quad (2.12)$$

One important key-point to the volume-averaging treatment is the requirement of scales separation, which can be stated as

$$l_p \ll l_{REV} \ll L, \quad (2.13)$$

in which l_p is the pore characteristic length scale, l_{REV} is the REV characteristic

length scale and L is the largest characteristic scale of the problem. Also, phenomenological scales have to be separated as well. For example, for conductive heat transfer, it is required that

$$\Delta T_{l_p} \ll \Delta T_{l_{REV}} \ll \Delta T_L, \quad (2.14)$$

where ΔT represents the maximum temperature difference across the respective length-scale. This condition represents a severe limitation to the volume-averaging modelling of combustion in porous media. It is usually not possible to define a REV that fulfills the separation of scales requirement since flames are characterized by a narrow region where the fuel is consumed and the chemical energy is released (the flame thickness) that is often of the order of a fraction of the length-scale of a single pore.

However, despite of this limitation, with these theorems one can proceed to evaluate the averaged conservation equations. This lengthy process is not to be reproduced here, as it is not our focus. Relevant works are given by [Kaviany \(1995\)](#), [Vafai \(2005\)](#), [Duval et al. \(2004\)](#) and [Whitaker \(1996\)](#).

From the theorems, it is easy to see that several terms will appear from the area integrals. These terms can be grouped into coefficients that are to be obtained from DNS calculations or experimental correlations. For instance, the volume-averaged gas-phase energy equation is given by

$$\begin{aligned} \mathbf{v}_{gg} \cdot \nabla \langle \bar{T}_g \rangle^g + \mathbf{v}_{gs} \cdot \nabla \langle \bar{T}_s \rangle^s = \nabla \cdot \mathbf{D}_{gg} \cdot \nabla \langle \bar{T}_g \rangle^g + \\ \nabla \cdot \mathbf{D}_{gs} \cdot \nabla \langle \bar{T}_s \rangle^s + \frac{A_{gs}}{V_g} \frac{h_c}{(\bar{\rho}c_p)_g} (\langle \bar{T}_s \rangle^s - \langle \bar{T}_g \rangle^g) + \langle \dot{s}_r \rangle^g, \end{aligned} \quad (2.15)$$

where the convective velocity vectors \mathbf{v}_{gg} and \mathbf{v}_{gs} are the coefficients of the terms containing the first-order derivatives, the total thermal diffusivity tensors \mathbf{D}_{gg} and \mathbf{D}_{gs} are the coefficients of the terms containing second-order derivatives, h_c is the interfacial conduction heat transfer coefficient, that is independent from the fluid velocity, and $\langle \dot{s}_r \rangle^g$ is an energy source term.

The derivation of the volume-averaged momentum conservation equation in a form equivalent to the Navier-Stokes equation is still an open problem. Some simplified forms are proposed in the literature ([KAVIANY, 1995](#)).

Since the conservation equations obtained from the volume-averaging procedure still depends on DNS calculations or experimental correlations and are quite compli-

cated, it is common to resort to a semi-heuristic approach. In this approach, the conservation equations take into account the fluid-solid interaction through physical arguments, but can not be obtained from the first principles. Although less complete, this semi-heuristic approach is useful in capturing the relevant physical aspects of the fluid-solid interaction. For instance, the superadiabatic temperatures achieved in combustion in porous media have been reproduced with the aid of such semi-heuristic formulation (PEREIRA et al., 2009; PEREIRA et al., 2010; PEREIRA et al., 2011; KOKUBUN et al., 2013). Such superadiabatic temperatures enhance the flammability limit of premixed flames, allowing burning of ultra-lean mixtures (WOOD; HARRIS, 2008). In opposition to the superadiabatic flames, so-called subadiabatic flames have been predicted theoretically (MIN; SHIN, 1991) and later obtained experimentally (VOGEL; ELLZEY, 2005). Low flame temperatures in the diffusion-flame regime were also predicted theoretically with the use of a simple semi-heuristic formulation (CHAO et al., 1994). Burning in low flame temperatures is a useful feature in lowering emissions of pollutants and formation of hazardous compounds, like NO_x , for instance (JUGJAI; PONGSAI, 2007; JUGJAI; PHOTHIYA, 2007).

2.2 Semi-heuristic formulation

The semi-heuristic equations of mass, mass fractions and energies are given by

$$\nabla \cdot \bar{\rho}_g \bar{\mathbf{u}} = 0, \quad (2.16)$$

$$\bar{\rho}_g \bar{\mathbf{u}} \cdot \nabla Y_i = \varphi \nabla \cdot (\bar{\rho}_g \mathbf{D}_i \cdot \nabla Y_i) - \varphi \dot{w}_{r,i}, \quad (2.17)$$

$$\bar{\rho}_g c_{p,g} \bar{\mathbf{u}} \cdot \nabla \bar{T}_g = \varphi \nabla \cdot (\lambda_g \cdot \nabla \bar{T}_g) + h_g (\bar{T}_s - \bar{T}_g) + \varphi \dot{w}_{r,i}, \quad (2.18)$$

$$0 = (1 - \varphi) \nabla \cdot (\lambda_s \cdot \nabla \bar{T}_s) - h_g (\bar{T}_s - \bar{T}_g) + \nabla \cdot \dot{\mathbf{q}}_r, \quad (2.19)$$

in which \mathbf{D}_i is the mass diffusivity tensor of specie i , which contains mass dispersion effects, λ_g is the thermal conductivity tensor of the gas-phase, which contains thermal dispersion effects, $\dot{\mathbf{q}}_r$ is the radiant heat flux vector and h_g is the volumetric interphase heat exchange coefficient.

For simplicity, it is usual to model the reaction source term as measured with its averaged properties. Hence, for a single-step, second order reaction-rate, we have

$$\dot{w}_{r,F} = B \bar{\rho}_g^2 \bar{T}_g^a \bar{Y}_F \bar{Y}_O \exp\left(-\frac{E_a}{R \bar{T}_g}\right), \quad (2.20)$$

where E_a is the activation energy, B is the frequency factor and a is a constant (that

will be taken as $a = 1$ in Chapters 2 and 5, and as $a = 0$ in Appendix A).

The semi-heuristic momentum conservation equation is written as

$$\bar{\rho}_g \bar{\mathbf{u}} \cdot \nabla \bar{\mathbf{u}} = -\varphi \nabla p + \nabla (\mu \nabla \bar{\mathbf{u}}) - \varphi \frac{\mu}{\bar{\mathbf{K}}} \bar{\mathbf{u}} - \varphi \frac{C_E}{\bar{\mathbf{K}}^{1/2}} \bar{\rho}_g |\bar{\mathbf{u}}| \bar{\mathbf{u}}, \quad (2.21)$$

where $\bar{\mathbf{K}}$ is the permeability tensor and C_E is the Ergun constant. The left-hand side are the macroscopic inertia forces. The first term in the right-hand-side is the pore pressure gradient, the second term is the macroscopic shear stress diffusion term (Brinkman viscous term), the third term is the microscopic viscous shear stress (Darcy term) and the fourth term is the microscopic inertial force term (Ergun inertial term).

For closure, the ideal gas equation of state is given by

$$\bar{p} = \frac{R}{M} \bar{\rho}_g \bar{T}_g. \quad (2.22)$$

This set of equations is simpler than that obtained from the rigorous application of the volume average method to the local problem. Here, the effects of the many coefficients that appear in the original equations are accounted for using fewer coefficients, namely the thermal conductivity tensors of both phases, the mass diffusion tensor and the superficial convection heat transfer coefficient. For the momentum conservation equation, the resistance force due to the tortuous porous channels is accounted through the last two terms in Eq. 2.21.

2.3 Formulation for the present work

In the present work we consider a stagnation-point flow of oxidant against a pool of liquid fuel, with the whole system immersed in an inert porous medium. In the region where the mass fluxes are nearly in a stoichiometric proportion, a diffusion flame is established. A schematic of the problem is shown in Fig. 2.3.

To solve this problem we consider some additional simplifications in order to obtain the set of equations to be used. These simplifications are

- Two-dimensional problem;
- Boundary-layer approximation;
- Neglect of the Ergun term;

- Isotropic and homogeneous porous medium;
- Rosseland approximation.

The consideration of an isotropic and homogeneous porous medium makes the thermal conductivities and permeability to be zero order tensors. The Rosseland approximation makes the radiation field to be considered as an effective heat conduction. Neglect of the Ergun term is justified when the flow velocity is small. The boundary-layer approximation makes the analysis to be made near the stagnation-point (inside the viscous layer formed near the liquid surface) and the properties variation along the stagnation-line to be much larger than variations normal to it.

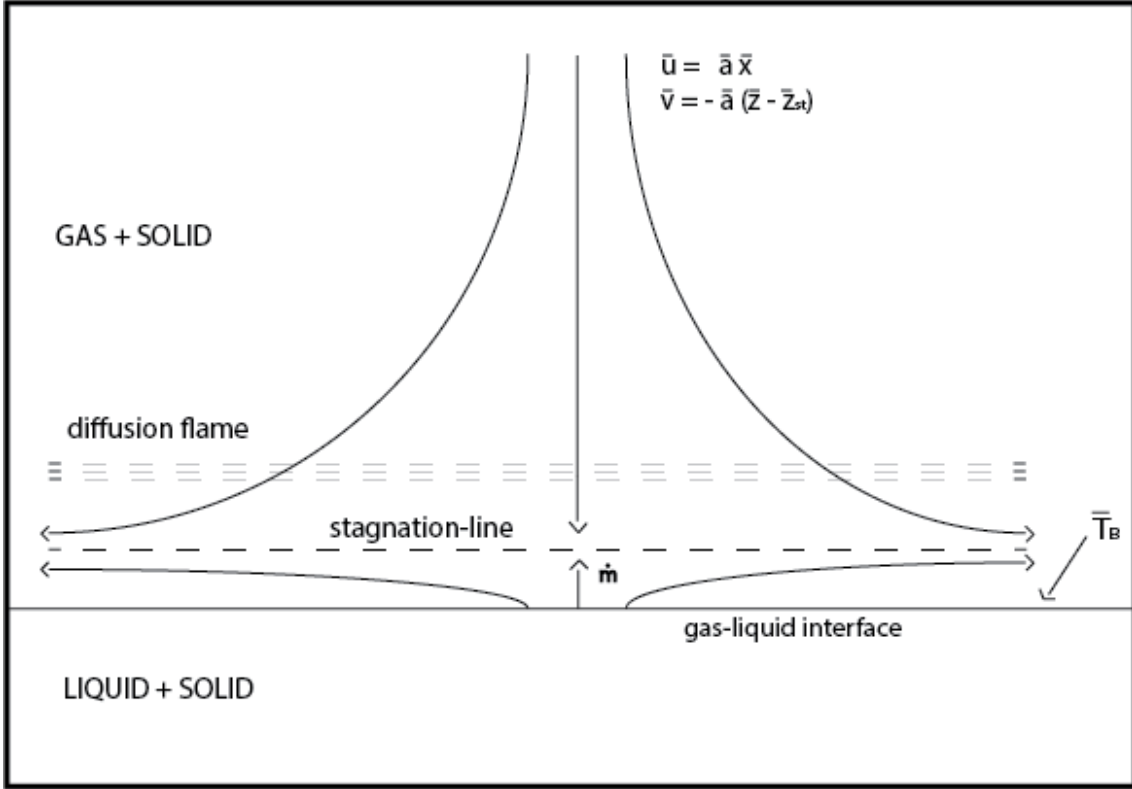
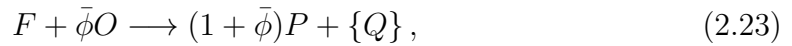


Figure 2.3 - Schematic of the present problem.

A one-step irreversible chemical reaction is considered through



where $\bar{\phi}$ mass units of oxidant are consumed for each mass unit of fuel, generating

$(1 + \bar{\phi})$ mass units of product and releasing an amount Q of heat.

The two spatial coordinates are \bar{x} (tangential to the liquid surface) and \bar{z} (normal to the liquid surface). Below $\bar{z} = 0$ the porous matrix is filled with liquid fuel.

For $\bar{z} > 0$ we have a pure gas flow and the conservation equations, with the simplifications stated previously, are given by

$$\bar{\rho} \frac{\partial \bar{u}}{\partial \bar{x}} + \frac{\partial \bar{\rho} \bar{v}}{\partial \bar{z}} = 0, \quad (2.24)$$

$$\bar{\rho} \bar{u} \frac{\partial \bar{u}}{\partial \bar{x}} + \bar{\rho} \bar{v} \frac{\partial \bar{u}}{\partial \bar{z}} = -\varphi \frac{\partial \bar{p}}{\partial \bar{x}} + \frac{\partial}{\partial \bar{z}} \left(\bar{\mu} \frac{\partial \bar{u}}{\partial \bar{z}} \right) - \varphi \bar{\mu} \frac{\bar{u}}{\bar{K}}, \quad (2.25)$$

$$\bar{\rho} \bar{u} \frac{\partial \bar{v}}{\partial \bar{x}} + \bar{\rho} \bar{v} \frac{\partial \bar{v}}{\partial \bar{z}} = -\varphi \frac{\partial \bar{p}}{\partial \bar{z}} + \frac{\partial}{\partial \bar{z}} \left(\bar{\mu} \frac{\partial \bar{v}}{\partial \bar{z}} \right) - \varphi \bar{\mu} \frac{\bar{v}}{\bar{K}}, \quad (2.26)$$

$$\bar{\rho} \bar{v} \frac{d\bar{Y}_F}{d\bar{z}} - \varphi \frac{d}{d\bar{z}} \left(\bar{\rho} \bar{D}_F \frac{d\bar{Y}_F}{d\bar{z}} \right) = -\varphi B \bar{\rho}^2 \bar{T}_g \bar{Y}_F \bar{Y}_0 e^{-E_a/R\bar{T}_g}, \quad (2.27)$$

$$\bar{\rho} \bar{v} \frac{d\bar{Y}_O}{d\bar{z}} - \varphi \frac{d}{d\bar{z}} \left(\bar{\rho} \bar{D}_O \frac{d\bar{Y}_O}{d\bar{z}} \right) = -\varphi \bar{\phi} B \bar{\rho}^2 \bar{T}_g \bar{Y}_F \bar{Y}_0 e^{-E_a/R\bar{T}_g}, \quad (2.28)$$

$$\bar{\rho} \bar{v} c_p \frac{d\bar{T}_g}{d\bar{z}} - \varphi \frac{d}{d\bar{z}} \left(\bar{\lambda}_g \frac{d\bar{T}_g}{d\bar{z}} \right) = \varphi Q B \bar{\rho}^2 \bar{T}_g \bar{Y}_F \bar{Y}_0 e^{-E_a/R\bar{T}_g} + h_g (\bar{T}_s - \bar{T}_g), \quad (2.29)$$

$$- (1 - \varphi) \bar{\lambda}_s \frac{d^2 \bar{T}_s}{d\bar{z}^2} = -h_g (\bar{T}_s - \bar{T}_g), \quad (2.30)$$

where \bar{u} and \bar{v} are the Darcy velocities, related with the local velocities \bar{u}_{lo} and \bar{v}_{lo} through $\{\bar{u}, \bar{v}\} = \varphi \{\bar{u}_{lo}, \bar{v}_{lo}\}$, where φ is the porosity.

The relation between the permeability \bar{K} and the porosity φ depends on the model utilized for the porous matrix. In the present work we consider a bed of particles, or fibers, which gives the permeability \bar{K} as (KAVIANY, 1995)

$$\bar{K} = \frac{\bar{d}_p^2}{180} \frac{\varphi^3}{(1 - \varphi)^2}, \quad (2.31)$$

where \bar{d}_p is the mean particle diameter.

For simplicity, we consider the liquid fuel to be at its boiling temperature, such that $\bar{T}_l = \bar{T}_B$ and the only equations needed in the liquid-solid region, $\bar{z} < 0$, are the mass conservation and the solid energy equation, given by

$$\bar{\rho}_l \bar{v}_l = \bar{\dot{m}}, \quad (2.32)$$

$$-(1 - \varphi)\bar{\lambda}_s \frac{d^2\bar{T}_s}{d\bar{z}^2} = -h_l(\bar{T}_s - \bar{T}_B). \quad (2.33)$$

For $\bar{z} \rightarrow +\infty$ (far from the viscous boundary-layer) the flow is potential-like, gas and solid phases are at thermal equilibrium and only oxidant is observed. Those conditions are expressed as

$$\bar{u} = \bar{a}\bar{x}, \quad \bar{v} = -\bar{a}(\bar{z} - \bar{z}_{st}), \quad \bar{T}_g = \bar{T}_s = \bar{T}_\infty, \quad \bar{Y}_O = \bar{Y}_{O\infty}, \quad \bar{Y}_F = 0, \quad (2.34)$$

in which \bar{a} is the strain-rate and \bar{z}_{st} is the position of the stagnation-point (which is determined by the vaporization rate \bar{m}).

The boundary conditions for the liquid-fuel reservoir, $\bar{z} \rightarrow -\infty$, are given by

$$\bar{v}_l = \bar{v}_{l-\infty}, \quad \bar{T}_s = \bar{T}_B. \quad (2.35)$$

The injection velocity $\bar{v}_{l-\infty}$ is such that the interface remains fixed at $\bar{z} = 0$.

At the liquid-gas interface, $\bar{z} = 0$, we consider $\bar{\rho}/\bar{\rho}_l \ll 1$ such that the no-slip condition $\bar{u} = 0$ may be used, as shown previously (SESHADRI et al., 2008). The vertical velocity $\bar{v}(0)$ is an unknown related with the vaporization rate \bar{m} . We assume that gas and liquid are at equilibrium at the interface, such that $\bar{T}_g(0^+) = \bar{T}_B$. The solid conducts heat from the gas-solid region and at the interface it is at a higher temperature than the gas, at $\bar{T}_s(0) > \bar{T}_B$.

Since the liquid is at its boiling temperature and the solid temperature is higher ($\bar{T}_s(0) > \bar{T}_B$), below the gas-liquid interface there is a three-phase (liquid-gas-solid) region with a high heat flux from above imposed by the flame sheet. Zhao and Liao (2000) have shown that for low heat flux, the evaporation process occurs uniformly at the surface. For increasing heat fluxes, a three-phase region is observed below the surface. This three-phase region is characterized by the appearance of gaseous bubbles at the pore walls, which decreases the effective heat transfer from solid to liquid. A schematic of the bubble formation in the three-phase region, when the heat flux is high, is shown in Fig. 2.4.

Modeling this three-phase region is quite complicated, with the need of considering the interaction between gas, liquid and solid in this zone (RAJU; TIEN, 2007). Since our focus is mainly on how the porous medium affect the flame, when compared to the non-confined case, a detailed model of this three-phase region is not needed. For our purposes it is enough to model this phase-change region, denoted as boiling

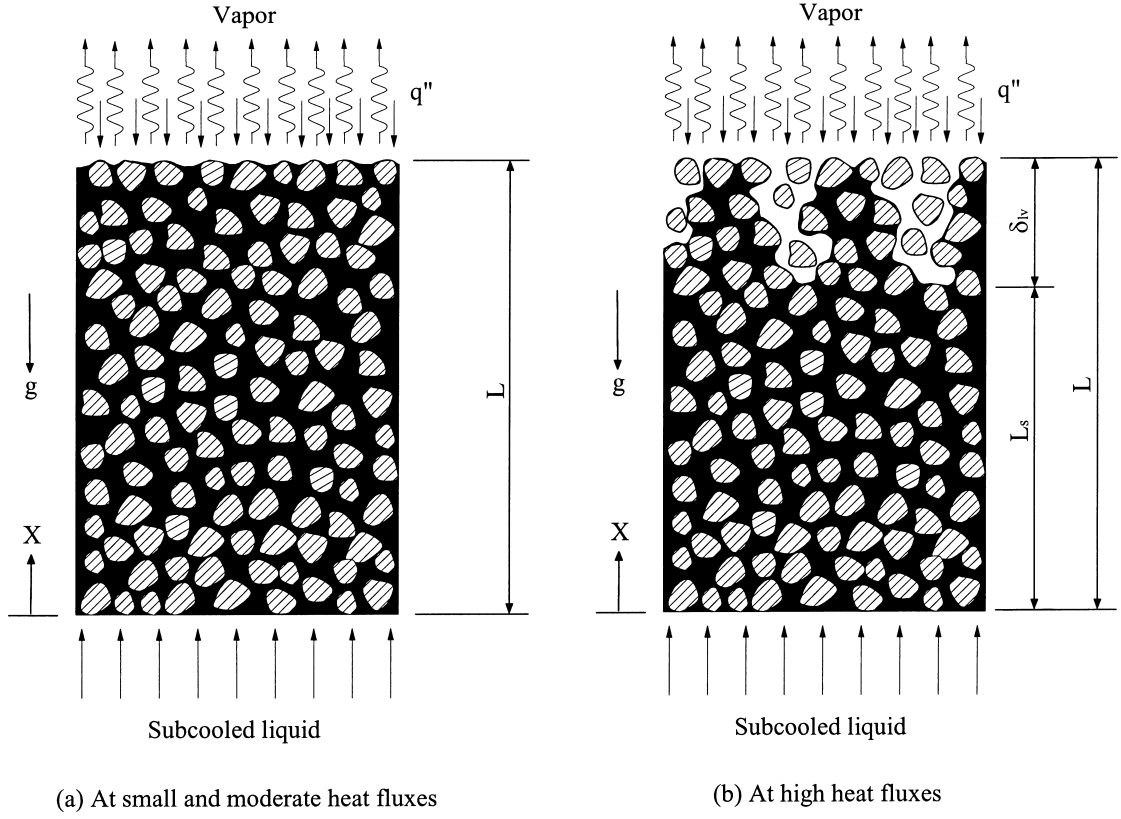


Figure 2.4 - Schematic of the bubble formation for increasing heat fluxes.
SOURCE: Zhao and Liao (2000).

zone, through a simple energy balance

$$\varphi \bar{\lambda}_g \left. \frac{d\bar{T}_g}{d\bar{z}} \right|_{0^+} + h_l \int_{-\infty}^{0^-} (\bar{T}_s - \bar{T}_B) d\bar{z} = \bar{m}L, \quad (2.36)$$

where L is the latent heat of vaporization of the liquid fuel. The energy balance in the phase-change region states that heat is introduced from the gas phase and from the heat exchange between solid and liquid. Since $\bar{T}_l = \bar{T}_B$ everywhere in the liquid-solid region, all the heat delivered to the liquid fuel goes to the phase-change process.

The velocity of the gas at the liquid surface \bar{v}_0^+ is related with the vaporization rate \bar{m} through

$$\bar{\rho} \bar{v}(0^+) = \bar{\rho}_l \bar{v}_l(0^-) = \bar{m}, \quad (2.37)$$

and the velocities $\bar{v}(0^+)$ ($\equiv \bar{v}(0)$) and $\bar{v}_l(0^-)$ ($\equiv \bar{v}_l(0)$) represent the velocities of vapour and liquid at the interface; the subscripts $+$ and $-$ denote the gas and liquid

sides of the interface, respectively.

At the interface, integration of Eq. 2.27 gives the fuel mass fraction conservation as

$$\varphi \bar{\rho} \bar{D}_F \left. \frac{d\bar{Y}_F}{d\bar{z}} \right|_{0^+} = - (1 - \bar{Y}_{F0}) (\bar{\rho} \bar{v})|_{0^+}. \quad (2.38)$$

For closure of the problem, we have the state equation

$$\bar{p} = \bar{\rho} R \bar{T}_g. \quad (2.39)$$

2.3.1 Variable change and non-dimensional formulation

The non-dimensional variables are defined as $u \equiv \bar{u}/\bar{v}_c$, $v \equiv \bar{v}/\bar{v}_c$, $p \equiv \bar{p}/(\bar{\rho}_\infty \bar{v}_c^2)$, $\rho \equiv \bar{\rho}/\bar{\rho}_\infty$, $\rho_l \equiv \bar{\rho}_l/\bar{\rho}_\infty$, $x \equiv \bar{x}/l_c$, $z \equiv \bar{z}/l_c$, $T_g \equiv \bar{T}_g/\bar{T}_\infty$, $T_s \equiv \bar{T}_s/\bar{T}_\infty$, $T_l \equiv \bar{T}_l/\bar{T}_\infty$ and $Y_O \equiv \bar{Y}_O/\bar{Y}_{O\infty}$, $Y_F \equiv \bar{Y}_F$, in which $\bar{v}_c \equiv \bar{a} l_c$ is a characteristic velocity of the problem related with the characteristic length scale $l_c \equiv \bar{\lambda}_{g\infty}/(\bar{\rho}_\infty c_p \bar{v}_c)$. The characteristic length scale l_c is then given by $l_c = \sqrt{\bar{\lambda}_{g\infty}/(\bar{\rho}_\infty c_p \bar{a})}$.

For $\bar{z} \rightarrow +\infty$, momentum equations with 2.34 give the pressure distribution as

$$\bar{p}_0 - \bar{p} = \frac{\bar{\rho}_\infty \bar{a}^2}{2\varphi} [\bar{x}^2 + (\bar{z} - \bar{z}_{st})^2] + \frac{\bar{a} \bar{\mu}_\infty}{2\bar{K}} [\bar{x}^2 - (\bar{z} - \bar{z}_{st})^2]. \quad (2.40)$$

For the limit $\varphi \rightarrow 1$ we recover the usual pressure distribution for the non-confined stagnation-point flow (SCHLICHTING, 1968). From the model used for the permeability, Eq. 2.31, $\varphi \rightarrow 1$ leads to $\bar{K} \rightarrow \infty$. The second term in the right-hand side of the expression 2.40 is the modification on the pressure distribution due to the presence of the porous matrix. Note that the lower the medium permeability, the higher the influence of the porous medium on the pressure field.

We introduce the following transformed variables in the gas-solid region

$$u = xU(\eta), \quad \rho v = -f(\eta), \quad \eta = \int \rho dz,$$

$$p_0 - p = \frac{1}{2\varphi} [x^2 + 2F(\eta)] + \frac{Pr}{2K} [x^2 - 2F(\eta)], \quad (2.41)$$

where Pr is the Prandtl number, assumed constant, $K \equiv \bar{K}/l_c^2$ is the non-dimensional permeability (Darcy number) and η is a mass-weighted coordinate. We consider a temperature dependence of the viscosity, gas-phase thermal conductivity

and mass diffusion such that $\rho\bar{\mu}/\bar{\mu}_\infty = \rho\bar{\lambda}_g/\bar{\lambda}_{g\infty} = \rho^2\bar{D}_i/\bar{D}_{i\infty} = 1$. This temperature-dependence was chosen to simplify the analysis, but extension to more realistic dependences can be easily considered. The first two variable transformations in 2.41 satisfies the mass conservation equation through $U = df/d\eta$.

Non-dimensional governing equations are then given by

$$Pr \frac{d^3 f}{d\eta^3} + f \frac{d^2 f}{d\eta^2} - \left(\frac{df}{d\eta} \right)^2 - \beta T_g^2 \frac{df}{d\eta} = -T_g (1 + \beta), \quad (2.42)$$

$$Pr \frac{d^2(fT_g)}{d\eta^2} + f \frac{d(fT_g)}{d\eta} - \beta T_g^3 f = (1 - \beta) \frac{dF}{d\eta}, \quad (2.43)$$

$$-f \frac{dY_F}{d\eta} - \frac{\varphi}{L_F} \frac{d^2 Y_F}{d\eta^2} = -\varphi Da Y_F Y_O e^{-T_a/T_g}, \quad (2.44)$$

$$-f \frac{dY_O}{d\eta} - \frac{\varphi}{L_O} \frac{d^2 Y_O}{d\eta^2} = -\varphi \phi Da Y_F Y_O e^{-T_a/T_g}, \quad (2.45)$$

$$-f \frac{dT_g}{d\eta} - \varphi \frac{d^2 T_g}{d\eta^2} = \varphi q Da Y_F Y_O e^{-T_a/T_g} + T_g N_g (T_s - T_g), \quad (2.46)$$

$$-\Gamma(1 - \varphi) \frac{d}{d\eta} \left(\frac{1}{T_g} \frac{dT_s}{d\eta} \right) = -T_g N_g (T_s - T_g), \quad (2.47)$$

where we defined $N_g \equiv h_g/(\bar{\rho}_\infty c_p \bar{a})$, $\beta \equiv \varphi Pr/K$ (inversely proportional to the Darcy number), $\Gamma \equiv \bar{\lambda}_s/\bar{\lambda}_{g\infty}$, $Da \equiv A\bar{Y}_{O\infty}\bar{p}_c/(\bar{a}R)$ (Damkohler number, where \bar{p}_c is some characteristic pressure), $T_a \equiv E_a/(R\bar{T}_\infty)$, $\phi \equiv \bar{\phi}/\bar{Y}_{O\infty}$, $q \equiv Q/(c_p\bar{T}_\infty)$ and if we assume that the average molecular weight is constant in our domain, we have $\rho = 1/T_g$, i.e., variations in pressure are higher-order.

Since we consider $T_l = T_B$ everywhere in the liquid region, the only equation needed is the solid energy equation, which is given by

$$-\Gamma(1 - \varphi) \frac{d^2 T_s}{dz^2} = -N_l (T_s - T_B), \quad (2.48)$$

where $N_l \equiv h_l/(\bar{\rho}_\infty c_p \bar{a})$. Note that in the liquid-solid region the spatial coordinate is only made non-dimensional. This is because the flow in the liquid-solid region is trivial.

Boundary conditions for $\eta \rightarrow \infty$ become

$$\frac{df}{d\eta} = 1, \quad T_s = T_g = 1, \quad Y_F = 0, \quad Y_O = 1. \quad (2.49)$$

At the surface $\eta = 0$, we have

$$\frac{df}{d\eta} = 0, \quad T_g = T_B, \quad Y_O = 0. \quad (2.50)$$

The relation between velocities at the interface and the liquid mass conservation gives

$$-f(0) = \dot{m}, \quad (2.51)$$

where $\dot{m} \equiv \bar{m}/(\bar{\rho}_\infty \sqrt{\bar{a}\alpha_g})$ is the vaporization rate, which determines the mass flux $f(0)$ at the interface $\eta = 0^+$. The solid temperature at the surface $T_s(0) > T_B$ is an unknown to be obtained from the continuity of the solid phase heat flux at the gas-liquid interface, given by

$$\frac{1}{T_B} \frac{dT_s}{d\eta} \Big|_{0^+} = \frac{dT_s}{dz} \Big|_{0^-}. \quad (2.52)$$

The term $1/T_B$ appears in the left-hand side of the above equality because of the use of different spatial coordinates in the gas-solid and in the liquid-solid regions. Note that $T_B = T_g(0)$.

Reservoir condition, $z \rightarrow -\infty$, is given by

$$T_s = T_B. \quad (2.53)$$

At the interface $\eta = z = 0$, fuel mass fraction and energy conservation gives

$$\frac{\varphi}{L_F} \frac{dY_F}{d\eta} \Big|_0 = (1 - Y_{F0})f(0), \quad (2.54)$$

$$\varphi \frac{dT_g}{d\eta} \Big|_{0^+} + N_l \int_{-\infty}^{0^-} (T_s - T_B) dz = \dot{m} l T_B, \quad (2.55)$$

where $l \equiv L/(c_p \bar{T}_B)$ is the dimensionless latent heat of vaporization. The effective latent heat is given by $l T_B$ because we define l with \bar{T}_B instead of \bar{T}_∞ . Species conservation at the interface 2.54 determines Y_{F0} , while energy conservation 2.55 determines the vaporization rate \dot{m} .

From the definition of β and the model used for K we have

$$\beta = 180 \left(\frac{\delta^2}{\bar{d}_p^2} \right) \left(\frac{1 - \varphi}{\varphi} \right)^2, \quad (2.56)$$

where $\delta = \sqrt{\bar{\nu}/\bar{a}}$ is the thickness of the macroscopic viscous boundary-layer, with $\bar{\nu} = \bar{\mu}_\infty/\bar{\rho}_\infty$ the gas kinematic viscosity far from the boundary-layer. Hence, β is proportional to the square of the ratio between the thickness of the macroscopic viscous boundary-layer δ and the mean particle diameter \bar{d}_p and to the square of the ratio between the solid phase volume $(1-\varphi)$ and the gas phase volume φ . With some modifications, this discussion for β was made by [Wu et al. \(2005\)](#), who also showed that for low enough permeability (high enough β), convective effects are negligible and in this case the flow is determined by a balance between the Darcy pressure term and viscous effect. For simplification, we define $\beta^* \equiv 180\delta^2/\bar{d}_p^2$, which results in $\beta = \beta^*[(1-\varphi)/\varphi]^2$. Then, β varies with the porosity, but β^* no.

If $\beta \gg 1$, then the flow is leading-order governed by the Darcy equation (modified in order to account for thermal expansion). On the other hand, if $\beta \ll 1$, then the Darcy term is a correction to the flow. In the energy conservation equations, if $N_g \gg 1$, then leading-order thermal equilibrium between gas and solid is observed. In this case, thermal non-equilibrium will be restricted to small regions near the gas-liquid surface and around the flame sheet. If $N_g \ll 1$, then gas and solid phases have a weak thermal coupling. The same discussion is valid for N_l .

From the momentum equation, [Eq. 2.43](#), we can see that $\beta = 1$ represents a turning point for the pressure distribution. For $\beta > 1$ we observe a maximum pressure above the stagnation-point, while for $\beta < 1$ the maximum pressure is at the stagnation-point, as in a non-confined problem. This feature was discussed previously ([WU et al., 2005](#)) and the explanation was that for $\beta > 1$ the fiber-level viscous dissipation was high, such that a higher pressure could be achieved above the stagnation-point. When $\beta = 1$, [Eq. 2.41](#) shows that $p_0 - p = \varphi x^2(1 + \beta)/2$. Particularly, at $x = 0$, $p = p_0$, which shows that no flow would occur for $\beta = 1$, as the pressure is constant along the stagnation-line. By examining [Eq. 2.43](#) we see that $\beta = 1$ is a singular point. Hence, we do not consider it in our calculations. This result suggest that the model may not be valid for $\beta \geq 1$.

The term $1/T_g$ in the left-hand side of [Eq. 2.47](#) appears from the coordinate transformation $\eta = \int \rho dz$. Then, this transformation leads to an effective solid thermal conductivity $\Gamma(1-\varphi)/T_g$ in the η plane. When $T_g < 1$, the solid has a larger effective thermal conductivity in the transformed coordinate η , while the opposite holds when $T_g > 1$. This happens because η is a mass-weighted coordinate, and when $T_g > 1$, from the state equation $\rho = 1/T_g$, $\eta < z$, while for $T_g < 1$, $\eta > z$. Then, in order to correctly account for the solid thermal conductivity, a correction must be made

for the solid energy equation in the η plane. Far enough from the surface, when $T_g \sim 1$, $\eta \sim z$, such that the solid thermal conductivity in the η plane is equal to the conductivity on the physical z plane.

The term T_g in the right-hand side of Eqs. 2.46 and 2.47 is also a consequence of the coordinate transformation. When $\eta > z$ ($T_g < 1$), the flow residence time in the η plane is greater than in the physical z plane, increasing the interphase heat exchange. The opposite holds when $\eta < z$ ($T_g > 1$). In order to correctly account for the heat exchange term, the T_g appears in the governing equations in the η plane.

2.3.2 Numerical method

In order to numerically solve the set of conservation equations, we use a finite-difference method with a pseudo-time marching technique. We first guess initial profiles that satisfies the boundary conditions and then add a fictitious unsteady term to the equations and the steady-state solution is obtained by marching in the pseudo-time (we use an explicit method for the pseudo-time derivatives). Convergence is said to be achieved when the transient terms $\partial/\partial t$ are less than 10^{-5} . We solve the flow for $U = df/d\eta$ and then obtain f by integrating the solution for U (TIEN et al., 1978). The conservation equation for U is second-order, then easily integrated.

For the first problem (Hiemenz flow), a higher-order central difference scheme is used for the first derivatives, such that the error $\sim \Delta\eta^2$, where $\Delta\eta$ is the constant mesh spacing. For the two remaining problems (vaporization and combustion), an upwind scheme is used for the convective terms, such that care must be taken when $f < 0$. The free stream is considered to be achieved when $dT_s/d\eta \sim 10^{-4}$, i.e., there is no heat flux to outside the domain.

The constant mesh spacing for the first two problems is considered as $\Delta\eta = 0.05$, while for the third part we consider $\Delta\eta = 2.5 \times 10^{-2}$. For the first part we compare our results (with the appropriate parameters) with the results obtained by Howarth (1938), and it was shown that $\Delta\eta = 0.05$ gives an error of less than 1%. For the second and third part, the constant mesh spacing was such that lowering this value in half showed no significant variation in the vaporization rate (burning rate) $-f(0)$.

2.4 Physical discussion

The interaction between gas, liquid and solid renders complexities to the problem. The tortuous channels of the porous matrix imposes a resistive force to the flow.

This resistance force imposed to the flow by the porous matrix is accounted through the parameter β in Eqs. 2.42 and 2.43. Thermal expansion of the gas increases the gas velocity, which increases the Darcy resistance force. This feature is accounted through the term T_g^2 in Eq. 2.42. When $\varphi \rightarrow 1$, $\beta \rightarrow 0$ and if $N \rightarrow 0$ the usual reactive boundary-layer equations for the non-confined stagnation-point flow are recovered.

If $\beta \gg 1$, the flow is leading-order given by the Darcy equation (modified in order to account for thermal expansion). For the model used for K , the limit of $\beta \gg 1$ can be achieved for low porosities - see Eq. 2.56. In this case, a high pressure gradient must be imposed in order to establish a flow due to the low value of the medium permeability (recall that $\beta \sim 1/K$). Then, when $\beta \gg 1$, high hydraulic losses are expected. Also, when the pores are large, the Rosseland approximation is no longer valid and in this case one must consider heat transport through radiation by the solid phase.

In the energy equations, the coupling is given by the heat exchange between phases (right-hand side of Eqs. 2.46 and 2.47). When a heat source is present (in the present case, such heat source is the flame), considering the local thermal non-equilibrium between phases is essential. Heat is released at the flame sheet by the exothermic reaction and is conducted away from the sheet by the gas, which then exchanges it with the solid. Since the solid has a higher thermal conductivity, when compared to the gas, the heat is transported to large regions from the flame sheet, and in the process, it heats the incoming reactants. However, as discussed in the previous Section, the heat distribution by the solid matrix cools the flame, as the rate-controlling process for this flame is mass diffusion, rather than mass flux as in premixed flames.

3 HEAT AND MOMENTUM TRANSFER PROBLEM: STAGNATION-POINT FLOW AGAINST AN IMPERMEABLE WALL

In this Chapter we analyze a stagnation-point flow established in an inert porous medium with heat exchange. We consider an impinging jet against an impermeable hot wall. Then, only the frozen equations for $\eta > 0$ are necessary (Eqs. 2.42, 2.43, 2.46 and 2.47), such that the reaction term in the gas energy equation is set to zero. Liquid equations are not necessary. The equations for Y_F and Y_O are neglected (Y_F does not exist in this case, and the equation for Y_O does not add any relevant information).

The influence of the wall temperature T_0 , porosity φ , gas-solid heat exchange N_g and solid-to-gas thermal conductivities ratio Γ on the wall properties and profiles is analyzed. The results presented here have applications on the context of heat exchangers.

Porous media that have a higher permeability whilst having a large thermal conductivity (compared to the gas thermal conductivity), are widely used as heat exchangers as they increase heat dissipation (VAFAI; KIM, 1990; JENG; TZENG, 2007). This enhancement occurs due to the heat conduction through the solid phase and the gas-solid heat exchange. While the majority of heat transfer problems in porous media consider local thermal equilibrium, such that a single energy conservation equation is used, porous heat exchangers must be analyzed with the use of the two-equation formulation: gas and solid are at thermal non-equilibrium. The local thermal non-equilibrium feature is essential in determining the characteristics and to assess the efficiency of heat exchangers.

When a non-isothermal problem is considered, heat and momentum transfer are coupled. If a constant-density model is used, the temperature field is obtained a posteriori from the flow field. Attia (2007) studied the effect of the porosity in a stagnation-point flow impinging on a permeable surface by using a porosity parameter (inversely proportional to the porosity). At the impermeable wall, suction or injection could be admitted as the boundary condition for the velocity. Results indicated that increasing the porosity parameter, i.e., reducing the medium porosity, causes a decrease on the thickness of both thermal and velocity boundary-layers and an increase in the heat transfer at the permeable surface.

For simple geometries and flows, analytical solutions may be obtained. Lee and

Vafai (1999) provided an extensive analytical characterization of forced convective flow through a channel filled with a porous material. A heated wall was considered to provide heat flux transversely to the flow. They obtained exact solutions for the transverse temperature profiles of solid and fluid phases, and classified heat transfer characteristics into three regimes, each of them dominated by a different physical heat transfer mechanism: fluid conduction, solid conduction and internal heat exchange between solid and fluid phases. Based on the results obtained, a complete electrical thermal network representative of transport through porous media was established.

Kokubun and Fachini (2011) analyzed a stagnation-point flow in a porous medium against an impermeable wall with heat exchange with a constant-density model, and hence, obtained analytical solutions for the profiles. The asymptotic limit of $\Gamma \equiv \bar{\lambda}_s/\bar{\lambda}_g \gg 1$ (large solid-to-gas thermal conductivities ratio) was considered. In that limit, two regions of interest exist: a large, outer region, in which the flow is potential and an inner region, near-wall, where viscous effect balance the Darcy pressure term. The interphase heat exchange was considered of the order of Γ , i.e., very large, such that in the outer region thermal equilibrium was admitted, with thermal non-equilibrium being observed only in the inner region.

For non-isothermal problems the constant-density assumption is not realistic. The deviations in the density field modifies the flow field, which may result in errors in the calculation of the parameters of interest, such as the wall heat transfer and the wall shear. The disparity between gas and solid thermal conductivities also adds complexity to the problem, as heat transfer may occur in different length scales for each phase, as discussed previously (KOKUBUN; FACHINI, 2011).

Here, we extend the previous results (KOKUBUN; FACHINI, 2011) by allowing gas thermal expansion (variable density) and general values of Γ . Hence, a numerical solution is sought to the coupled heat and momentum transfer problem.

3.1 Physical problem

The geometry to be studied is a two-dimensional stagnation-point flow established in an inert porous medium against an impermeable wall at a constant temperature \bar{T}_0 , higher than \bar{T}_∞ (temperature of the incoming jet). Due to the hot wall, thermal expansion decreases the gas density and couples flow and energy equations. A schematic of the problem is shown in Fig. 3.1, where \bar{x} is the spatial coordinate tangential to the impermeable wall and \bar{z} is the normal coordinate. The impermeable

wall is located at $\bar{z} = 0$.

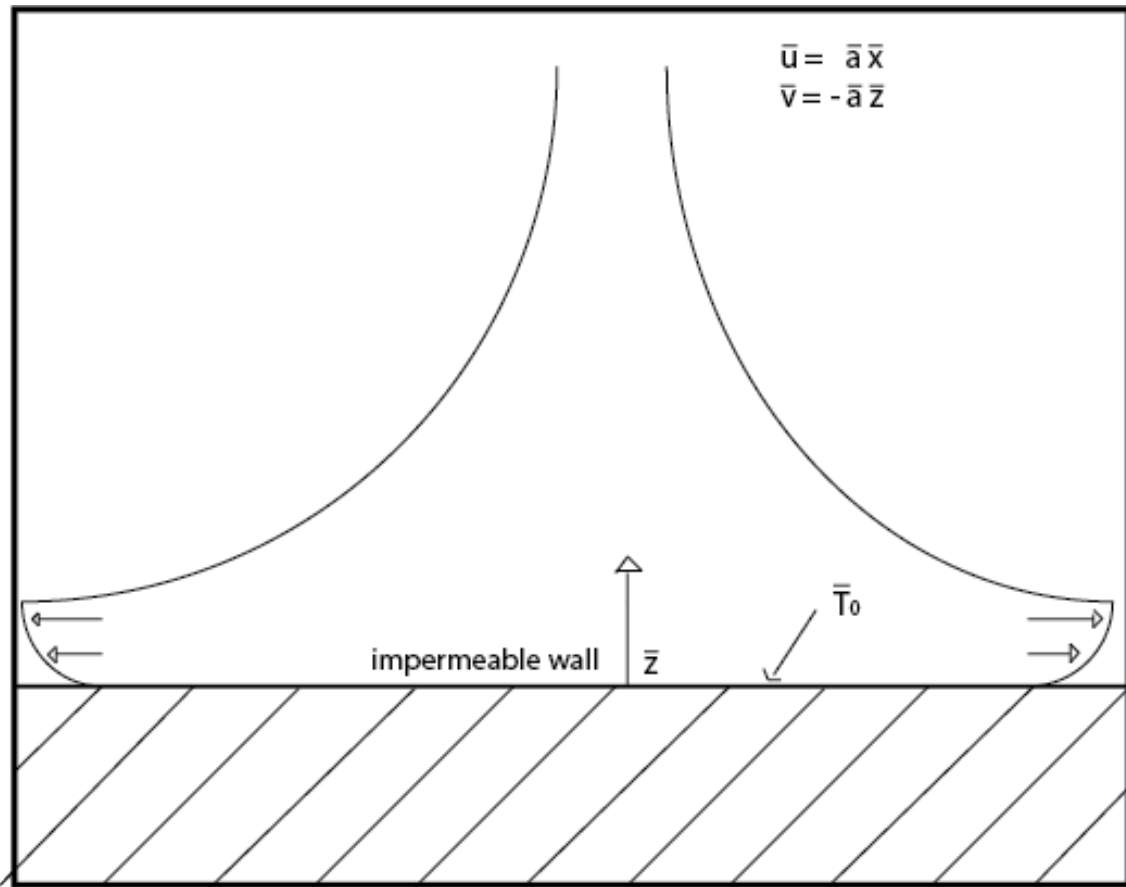


Figure 3.1 - Schematic of the problem.

Three different heat transport mechanisms exist: convection and conduction through the gas, and conduction through the solid. The solid temperature is influenced directly only by the local gas temperature. Since we consider a hot wall, the gas temperature is higher in the present problem when compared to an incompressible flow, because of the very low velocity close to the impermeable wall.

Thermal expansion modifies the velocity field as it induces a resistance force against the incoming flow, lowering the local vertical velocity. The horizontal velocity, on the other hand, increases with thermal expansion because of the boundary-layer assumption $\rho = \rho(z)$. The Darcy resistance term is proportional to the flow velocity. Then, thermal expansion decreases the Darcy term in the normal direction and increases in the tangential direction.

3.2 Mathematical formulation

The following set of non-dimensional governing equations is valid for this problem

$$Pr \frac{d^3 f}{d\eta^3} + f \frac{d^2 f}{d\eta^2} - \left(\frac{df}{d\eta} \right)^2 - \beta T_g^2 \frac{df}{d\eta} = -T_g (1 + \beta), \quad (3.1)$$

$$Pr \frac{d^2(fT_g)}{d\eta^2} + f \frac{d(fT_g)}{d\eta} - \beta T_g^3 f = (1 - \beta) \frac{dF}{d\eta}, \quad (3.2)$$

$$-f \frac{dT_g}{d\eta} - \varphi \frac{d^2 T_g}{d\eta^2} = T_g N_g (T_s - T_g), \quad (3.3)$$

$$- \Gamma (1 - \varphi) \frac{d}{d\eta} \left(\frac{1}{T_g} \frac{dT_s}{d\eta} \right) = -T_g N_g (T_s - T_g). \quad (3.4)$$

Injection conditions for $\eta \rightarrow \infty$ are given by

$$\frac{df}{d\eta} = 1, \quad T_s = T_g = 1. \quad (3.5)$$

At the impermeable wall, $\eta = 0$, we have

$$f = \frac{df}{d\eta} = 0, \quad T_s = T_g = T_0. \quad (3.6)$$

In this particular problem we have four parameters of interest: φ , T_0 , N_g and Γ . The first is the porosity (volume occupied by the gas phase), the second is the constant wall temperature, the third quantifies the strength of the heat exchange between gas and solid, while the fourth is the solid-to-gas thermal conductivities ratio. There are also correlations between N_g , φ and Γ , which can be modeled or obtained empirically. For the sake of simplicity we do not consider such correlations and vary N_g , φ and Γ independently.

The numerical scheme is validated by comparing the results for $\rho = \varphi = Pr = T_0 = 1.0$ and $N_g = 0$ with the results of [Howarth \(1938\)](#). The set of parameters used for comparison defines an incompressible, isothermal flow in a non-confined medium, which is the problem analyzed by [Howarth \(1938\)](#). For $\Delta\eta = 0.05$, the calculated wall shear is $f''(0) = 1.2327$, while Howarth's result gives $f''(0) = 1.2326$, an error of less than 0.01%. Hence, we use $\Delta\eta = 0.05$ as our constant mesh spacing.

3.3 Results

We analyze the influence of φ , T_0 , N_g and Γ on the present problem. A mean pore diameter $\bar{d}_p = 5 \text{ mm}$ is considered. The impinging gas is air, with its properties evaluated at 293 K . Then, characteristic profiles of temperatures, velocities and pressure are obtained for $Pr = \varphi = 0.7$, $\Gamma = 50.0$, $T_0 = 1.6$, $\beta^* = 1.08$ and $N_g = 1.0$ and shown in Figs. 3.2, 3.3, 3.4 and 3.5, where we also compare results with the constant-density model ($\rho = 1$). Profiles are plotted in the physical z plane.

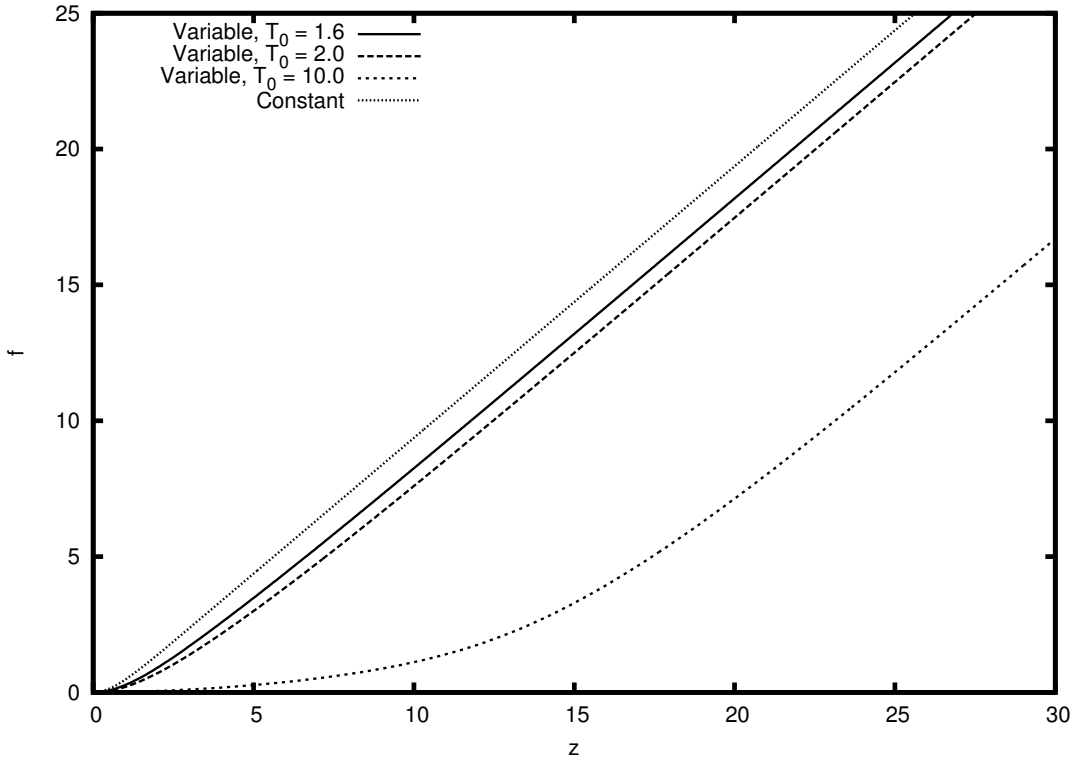


Figure 3.2 - Vertical velocities with and without thermal expansion with $\beta^* = 1.08$, $Pr = \varphi = 0.7$, $N_g = 1.0$, $T_0 = \{1.6, 2.0, 10.0\}$ and $\Gamma = 50.0$.

The presence of a hot wall induces thermal expansion on the flow right above the stagnation-point, leading to a resistive force, which lowers the local flow velocity f , as seen in Fig. 3.2, where f is shown for $T_0 = \{1.6, 2.0, 10.0\}$ and compared with f for the incompressible case. If the wall temperature is very high, then a stagnant-region near the wall exists due to the high value of the resistive force induced by thermal expansion. Since in the direction tangential to the impermeable wall no resistive force other than Darcy exists (no incoming flow), thermal expansion enhances the

horizontal velocity f' when compared to the incompressible case, as seen in Fig. 3.3.

The existence of a velocity overshoot in the boundary-layer occurs if there is a temperature inside the boundary-layer higher than the free stream temperature. In the context of an impinging, compressible flow against a heated wall this was first analyzed by [Cohen and Reshotko \(1955\)](#). This velocity overshoot is more prominent for higher values of T_0 . If the porosity is low enough, this velocity overshoot is smoothed due to the high magnitude of the Darcy resistance term. This can be seen in Fig. 3.6, where we show f' for different porosities.

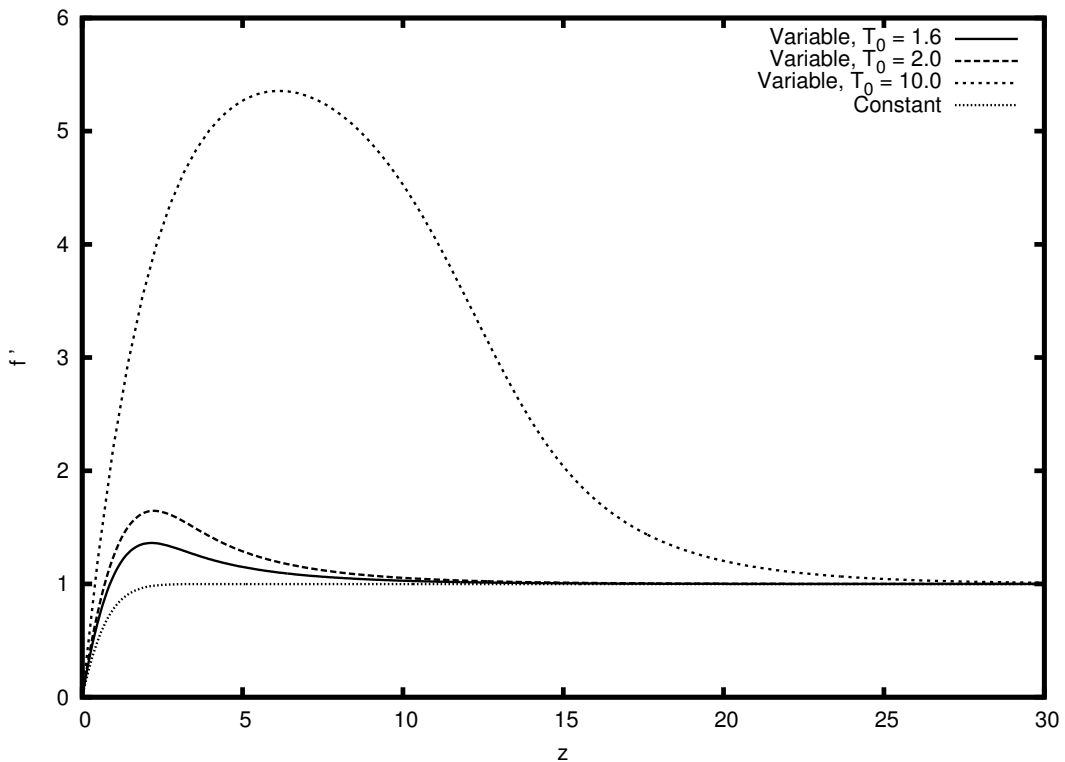


Figure 3.3 - Horizontal velocities with and without thermal expansion with $\beta^* = 1.08$, $Pr = \varphi = 0.7$, $N_g = 1.0$, $T_0 = \{1.6, 2.0, 10.0\}$ and $\Gamma = 50.0$.

Temperatures are also higher when thermal expansion is considered, as seen in Fig. 3.4. The lower f field due to the resistive force induced by thermal expansion makes the gas temperature increase, which also increase the solid temperature, since they are thermally coupled. This also makes the length of the region of thermal influence larger. In Fig. 3.7 the difference between phases temperature is shown for the compressible and incompressible cases. Near the wall the higher interphase heat exchange

due to thermal expansion minimizes temperatures difference. However, as the region of thermal influence is larger in such case, this difference in the incompressible case goes to zero before than in the compressible case. From Figs. 3.2, 3.3 and 3.4 (cases in which $T_0 = 1.6$ for the velocities) we can see that the thickness of the viscous boundary-layer is around $\eta = 5.0$, while the region of thermal influence is around $\eta = 20.0$. This disparity, that occurs even considering $Pr = O.7$, exist because of the existence of heat conduction through the solid phase, which is measured by $\Gamma(1 - \varphi)$ (effective solid phase thermal conductivity). When $\Gamma(1 - \varphi) = O(1)$ (high porosity medium, or solid matrix with a thermal conductivity of the same order of the gas thermal conductivity), the thickness of the thermal layer is of the same order of the viscous boundary-layer if $Pr = O(1)$.

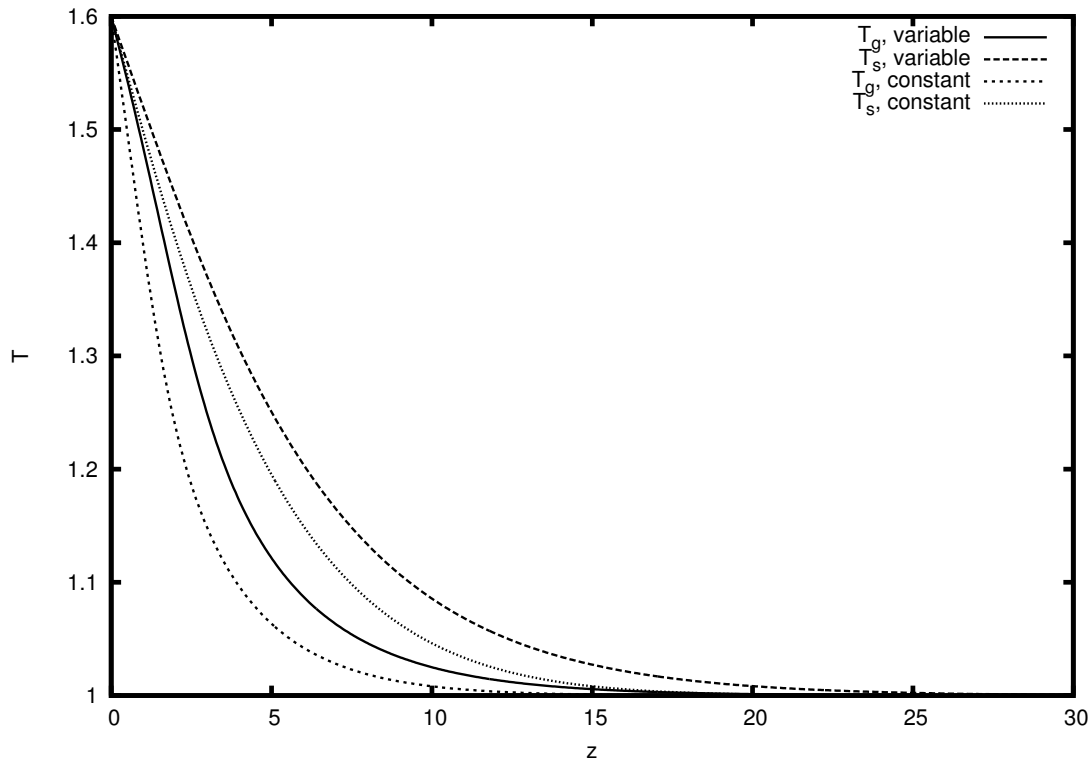


Figure 3.4 - Temperature profiles with and without thermal expansion with $\beta^* = 1.08$, $Pr = \varphi = 0.7$, $N_g = 1.0$, $T_0 = 1.6$ and $\Gamma = 50.0$.

Since Γ is large (large solid-to-gas thermal conductivities ratio), when the porosity is sufficiently far from unity, i.e., $(1 - \varphi) \gg \Gamma^{-1}$, Eq. 3.4 shows that the thermal conduction through the solid phase reaches a region far from the wall. Then, since gas and solid are thermally coupled, the gas temperature profile also has a larger region

of influence. For lower porosities the extent of this region is larger. The same trend is observed if Γ is increased, since, effectively, the term that govern the thickness of the thermal layer is $\sqrt{\Gamma(1-\varphi)}$. In Kokubun and Fachini (2011), the asymptotic limit of $\Gamma \gg 1$ with $(1-\varphi) = O(1)$ was explored with the aid of a constant-density model ($\rho = 1$). In this asymptotic limit (and when $\rho = 1$), two length-scales exist: an outer region, in which the flow is potential, and an inner, near-wall, region, in which viscous effects balance the Darcy pressure term.

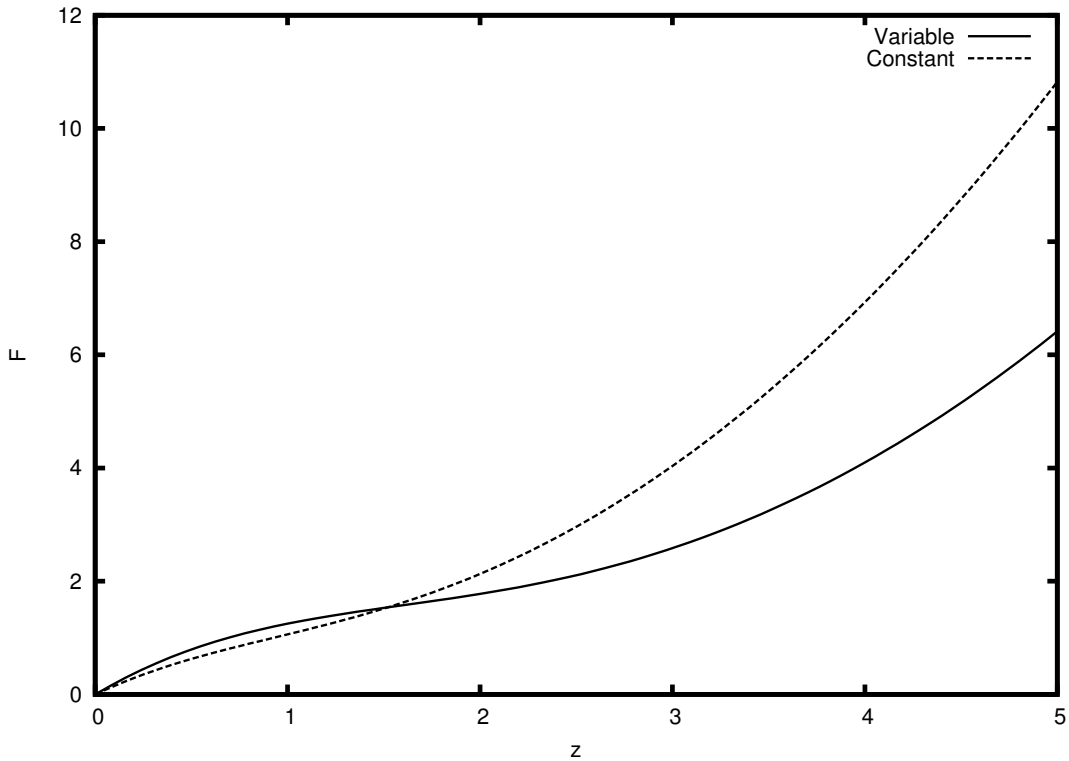


Figure 3.5 - Pressure profiles with and without thermal expansion with $\beta^* = 1.08$, $Pr = \varphi = 0.7$, $N_g = 1.0$, $T_0 = 1.6$ and $\Gamma = 50.0$ $T_0 = 1.6$.

The pressure recovery F along the stagnation line is shown in Fig. 3.5. Close to the wall the resistive force due to thermal expansion induces a decrease on the local pressure, increasing $F \sim p_0 - p$. Far from the wall the pressure recovery for the incompressible case is higher. The porous matrix induces an increase on the local pressure gradient due to the higher flow resistance. For $\beta^* = 1.08$ and $\varphi = 0.7$, $\beta \sim 0.198$. When $\varphi = 0.3$, we obtain $\beta \sim 5.88$. In this case, as discussed previously, the pressure field presents a maximum, $F < 0$, above the stagnation-point. This can be seen in Fig. 3.8, where we show the pressure profile for $\varphi = 0.3$ for the compressible

(variable density) and incompressible (constant density) case. The location of the maximum pressure point is found by setting $F' = 0$ in Eq. 3.2

$$\left\{ Pr \frac{d^2(fT_g)}{d\eta^2} + f \frac{d(fT_g)}{d\eta} - \beta T_g^3 f \right\} \Big|_{\eta_{max}} = 0 \quad (3.7)$$

where η_{max} is the location of the maximum pressure point. Then, thermal expansion plays a role in determining this maximum pressure position, while $\beta > 1$ determines its existence (as discussed phenomenologically by Wu et al. (2005) and shown mathematically in the previous section).

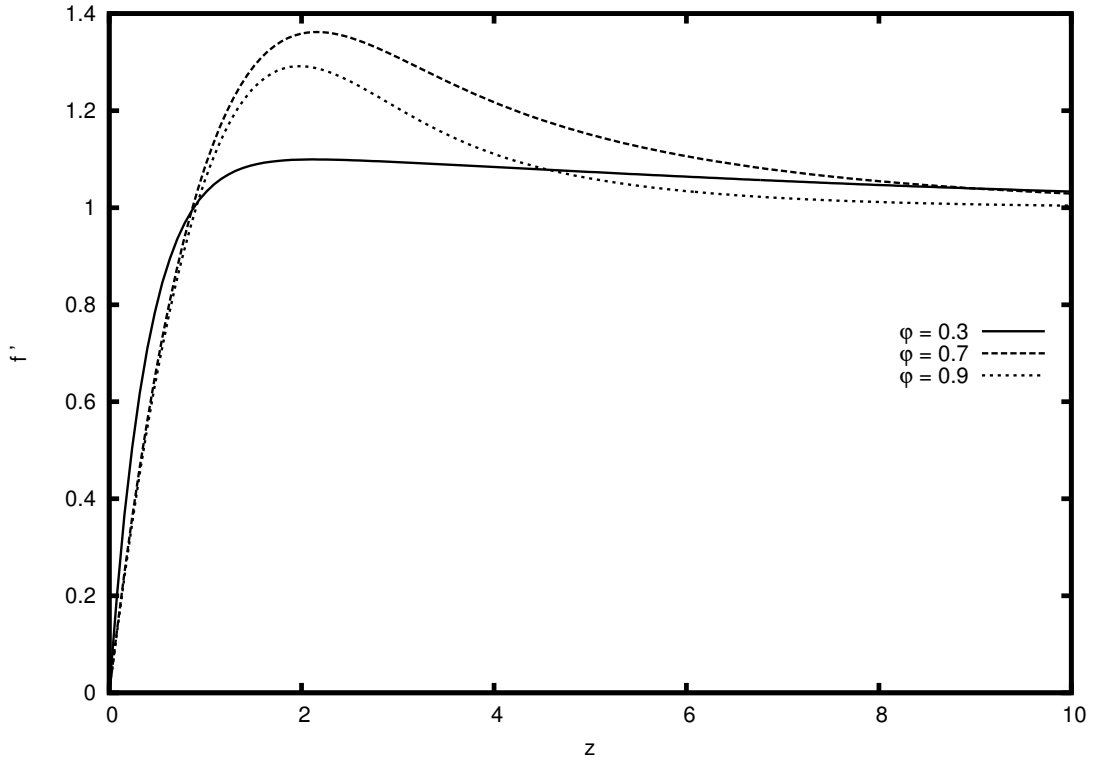


Figure 3.6 - Velocity overshoot for different porosities and with $\beta^* = 1.08$, $Pr = 0.7$, $N_g = 1.0$, $T_0 = 1.6$ and $\Gamma = 50.0$ $T_0 = 1.6$.

The wall shear $f''(0)$ variation with the wall temperature T_0 is shown in Fig. 3.9 for three different porosities φ . When the porosity is high ($\varphi = 0.9$), an increase on the wall temperature increases the wall shear. However, when the porosity is low ($\varphi = 0.3$), such that β is sufficiently higher than 1, the wall shear presents a maximum and then decreases with increasing wall temperatures. When $\beta > 1$, the Darcy term has a strong influence on the flow. Then, when β is sufficiently

higher than 1, the high Darcy resistance decreases the local flow velocity, leading to lower values of the wall shear $f''(0)$. As the wall temperature increases, this effect is stronger because the Darcy resistance is accounted effectively through the term βT_g^2 in Eq. 3.1, which decreases the wall shear. If β is sufficiently lower than 1, thermal expansion (enhancement of the local flow velocity) surpass the Darcy resistance, and the wall shear increases with the wall temperature, as one would expect in a non-confined (no porous matrix) problem. It is worth to note that this feature is dominated by β , therefore, even though we discuss it through variations in the porosity, the same trend is observed for different mean particle diameter \bar{d}_p or strain-rate \bar{a} (specifically, $\beta \sim 1/(\bar{a}\bar{d}_p^2)$).

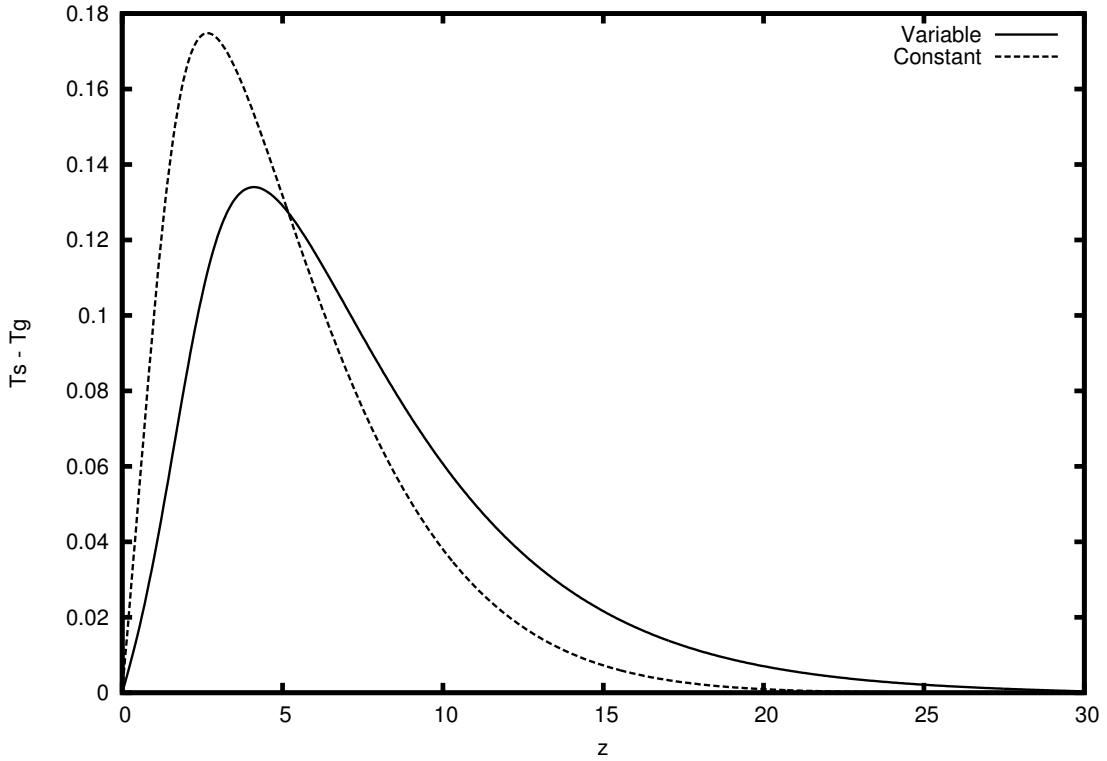


Figure 3.7 - Temperatures difference with and without thermal expansion with $\beta^* = 1.08$, $Pr = \varphi = 0.7$, $N_g = 1.0$, $T_0 = 1.6$ and $\Gamma = 50.0$

The heat transfer at the wall by gas Q_g and solid Q_s is computed, respectively, through

$$Q_g = -\varphi \left. \frac{dT_g}{d\eta} \right|_0, \quad Q_s = -\Gamma(1 - \varphi)T_0^{-1} \left. \frac{dT_s}{d\eta} \right|_0, \quad (3.8)$$

where the minus is introduced only to make $\{Q_g, Q_s\} > 0$. Both gas and solid heat

transfer at the wall increase for increasing wall temperatures, as expected. For higher porosities, the contact area between gas and the impermeable wall increases, which increases the gas heat transfer and decreases the solid heat transfer. These features can be seen in Figs. 3.10 and 3.11.

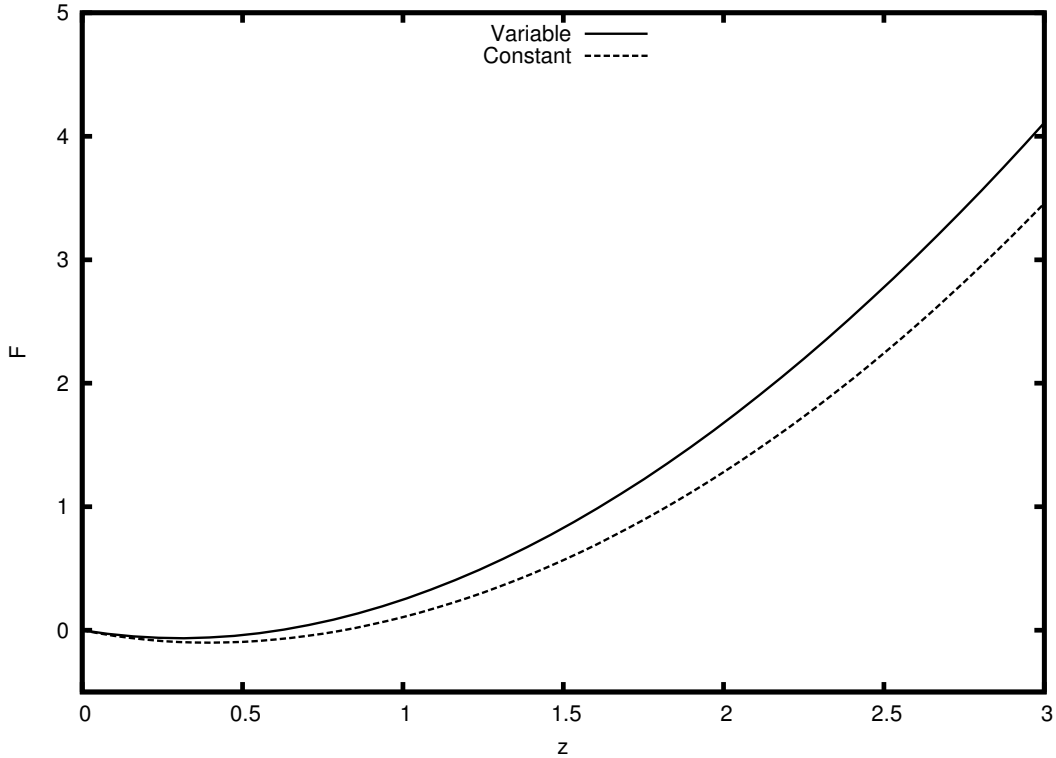


Figure 3.8 - Pressure profiles for $\varphi = 0.3$ with $\beta^* = 1.08$, $Pr = 0.7$, $N_g = 1.0$, $T_0 = 1.6$ and $\Gamma = 50.0$

The influence of the porosity φ on the wall shear $f''(0)$ for different wall temperatures T_0 is shown in Fig. 3.12. As the porosity increases, the wall shear decreases because of the lower influence of the Darcy resistance term (recall that $\beta \sim [(1-\varphi)/\varphi]^2$). For low porosities the wall shear is higher when the wall temperature is lower, opposed as what happens in a non-confined flow. This happens when $\beta > \beta_0$ (for the set of parameters considered, $\beta_0 \sim 7.5$, as seen in Fig. 3.12), and it is an effect of the lower local flow velocity induced by the high influence of the Darcy resistance term βT_g^2 . When $\beta < \beta_0$, thermal expansion surpass this resistance, and the flow accelerates, leading to a higher wall shear when the wall temperature is higher. If an incompressible flow is considered, higher wall temperatures will always lead to a higher wall shear.

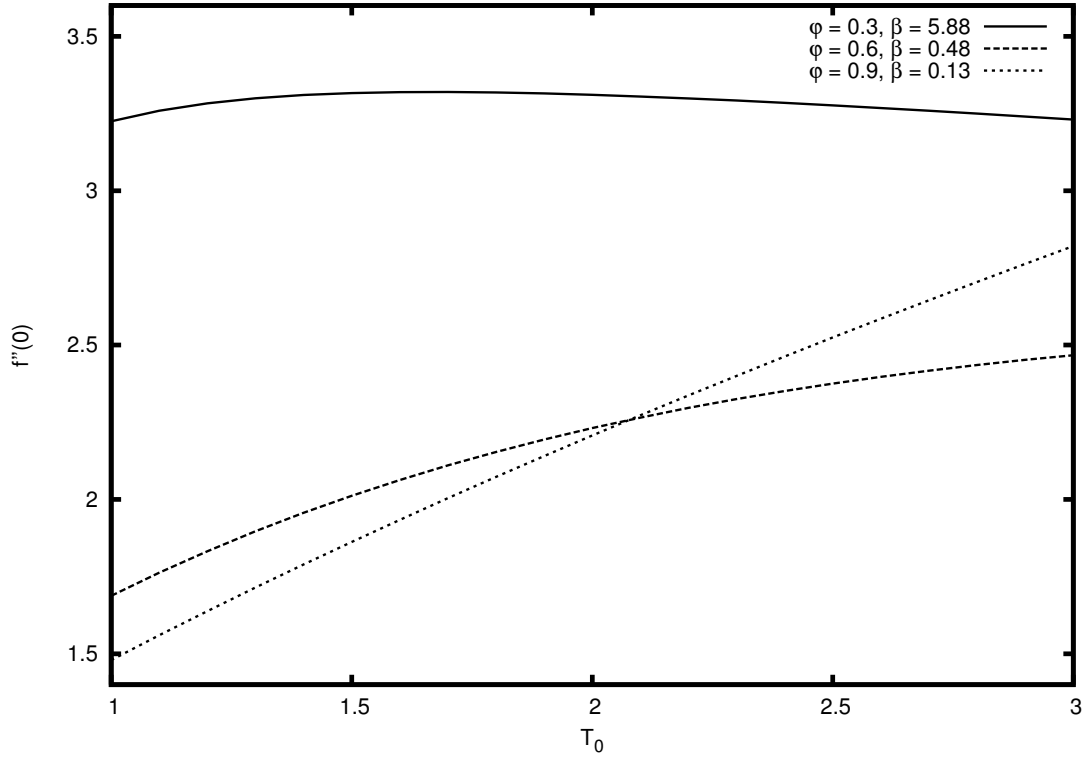


Figure 3.9 - Wall shear \times wall temperature, for different porosities with $\beta^* = 1.08$, $Pr = 0.7$, $N_g = 1.0$ and $\Gamma = 50.0$.

The effect of the magnitude of the interphase heat exchange N_g on the wall shear $f''(0)$ is minimum. For the set of parameters considered, a variation from $N_g = 0.1$ to $N_g = 10$ modifies $f''(0) = 1.946$ to $f''(0) = 2.014$, or approximately a 3.5% increase. The wall heat flux, on the other hand, changes significantly as one can see in Fig. 3.13. As N_g increases, the gas phase heat transfer at the wall diminishes, while the solid phase increases. When N_g is large, $T_s - T_g$ decreases, as one can see in Fig. 3.14.. Then, at the wall, the gas heat flux decreases while the solid heat flux increases for increasing values of N_g . Note that the solid is always at a higher temperature than the gas because of its higher thermal conductivity.

The wall shear variation with Γ is also negligible, as it goes from $f''(0) = 1.916$ to $f''(0) = 2.014$ when Γ changes from 10^{-3} to 100. The phases heat flux changes significantly, on the other hand. Figure 3.15 shows that increasing values of Γ increase the solid heat flux at the wall, while the gas heat flux decreases. Recalling that Γ is the solid-to-gas thermal conductivities ratio, this result is expected.

The solid matrix volume $(1 - \phi)$ influences the length of the thermal layer. For lower

porosities (larger solid volume), heat conduction through the solid phase becomes more relevant. In this case, heat is transported to larger regions and the extent of the thermal layer η_{TBL} increases. Its growth is proportional to $\sqrt{\Gamma(1-\varphi)}$ and if we define the length of this thermal layer as the position where $T = 1.05$ (a temperature rise of 5% when compared to the free stream temperature), this behavior can be seen in Fig. 3.16.

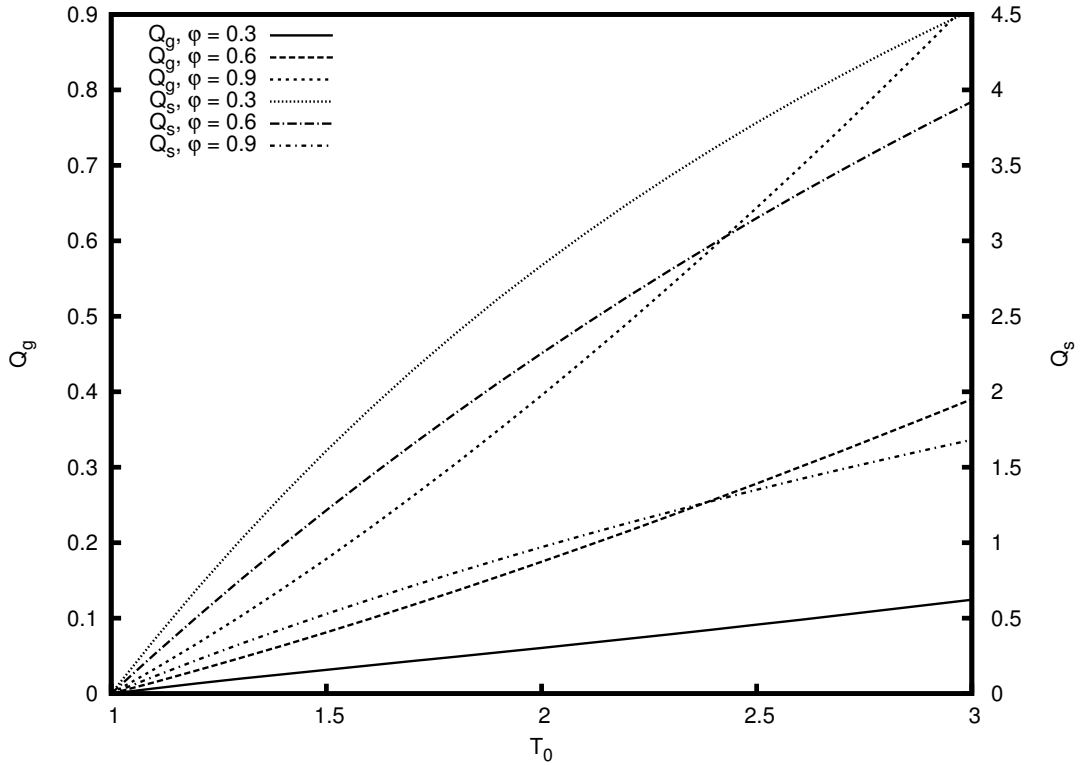


Figure 3.10 - Heat transfer at the wall \times wall temperature, for different porosities with $\beta^* = 1.08$, $Pr = 0.7$, $N_g = 1.0$ and $\Gamma = 50.0$.

3.4 Conclusions

We analyzed a stagnation-point flow established in a porous medium with interphase heat exchange. Through a semi-heuristic formulation we studied the coupled heat and momentum transfer problem. It was shown that thermal expansion decreases the vertical velocity f and increases the horizontal velocity f' . This happens because thermal expansion induces a resistive force against the incoming vertical mass flux, but the horizontal velocity has no such resistance, such that thermal expansion only increase the horizontal velocity component. The presence of a hot wall induces a

velocity overshoot in the boundary-layer. If the porosity is low enough, the high magnitude of the Darcy resistance term smooths this overshoot. The porous matrix enhances gas temperature, as it provides heat to the flow.

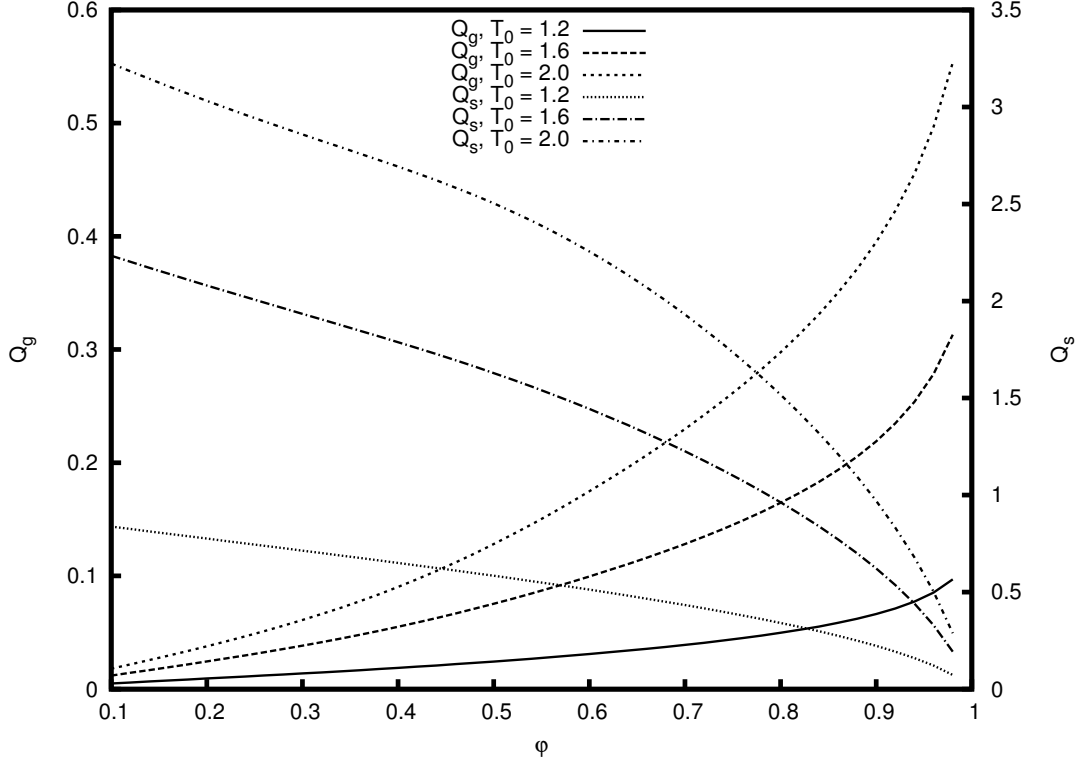


Figure 3.11 - Heat transfer at the wall \times porosity, for different wall temperatures with $\beta^* = 1.08$, $Pr = 0.7$, $N_g = 1.0$ and $\Gamma = 50.0$.

From the non-dimensionalization, the parameter β arises, which measures the square of the ratio between the thickness of the macroscopic viscous boundary-layer δ and the mean particle diameter \bar{d}_p (with the use of a bed-of-particles model for the permeability). This parameter, which was already recognized previously in the literature (WU et al., 2005), determines the existence of a maximum pressure above the stagnation-point. Thermal expansion determines its location, as seen in Eq. 3.7. The flow is influenced by the crossed effects of viscosity, inertia and Darcy resistance term. The magnitude of βT_g^2 determines the strength of the Darcy term in this dynamics, where the term T_g^2 comes from thermal expansion.

For β sufficiently lower than 1, an increase on the wall temperature leads to an increase on the wall shear due to the horizontal acceleration of the gas near the

wall. However, when β is sufficiently higher than 1, increasing wall temperatures first increase the wall shear and then decrease it. This is an effect of the increase of the Darcy resistance (which is proportional to the local flow velocity, and due to thermal expansion, also to the gas temperature), which lowers the local flow velocity. As discussed, the flow is influenced by the crossed effects of viscosity, inertia and Darcy resistance. When $\beta > 1$, the Darcy resistance has a strong influence on the flow. So, even though thermal expansion induces an acceleration on the flow velocity, the same effect induces a stronger flow resistance, which lowers the wall shear for increasing wall temperatures. This behavior is opposite to what is observed in non-confined mediums, as an increase on the wall temperature will always enhance wall shear in such cases. The existence of a maximum pressure above the stagnation-point when $\beta > 1$ is also an effect of this high resistance force, as discussed previously (WU et al., 2005).

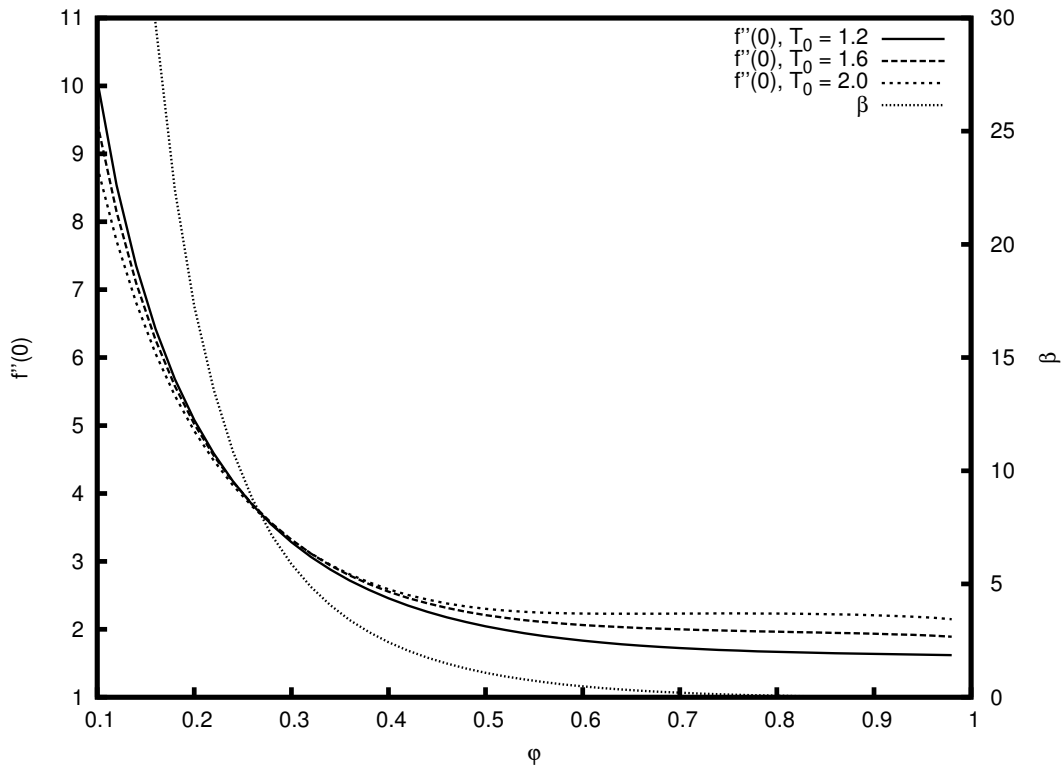


Figure 3.12 - Wall shear \times porosity, for different wall temperatures with $\beta^* = 1.08$, $Pr = 0.7$, $N_g = 1.0$ and $\Gamma = 50.0$.

Since the phases are thermally coupled, heat conduction through the solid phase enhances the thickness of the thermal layer for this problem. Its growth is pro-

portional to $\sqrt{\Gamma(1-\varphi)}$, as seen in Eq. 3.4 and Fig. 3.13. In the asymptotic limit $\Gamma \gg 1$ with $(1-\varphi) = O(1)$, an outer region arises, which is dominated by heat conduction through the solid phase. When an incompressible flow is considered, the flow is potential in this outer region (KOKUBUN; FACHINI, 2011). Since large values of $\sqrt{\Gamma(1-\varphi)}$ leads to thicker thermal layers, porous heat exchangers are more efficient in the low-porosity limit $\varphi \ll 1$, or for materials that have larger values of Γ . However, one must balance this gain with the consideration that flows in low-porosity mediums have high hydraulic losses (for low porosities, the imposed pressure gradient must be high).

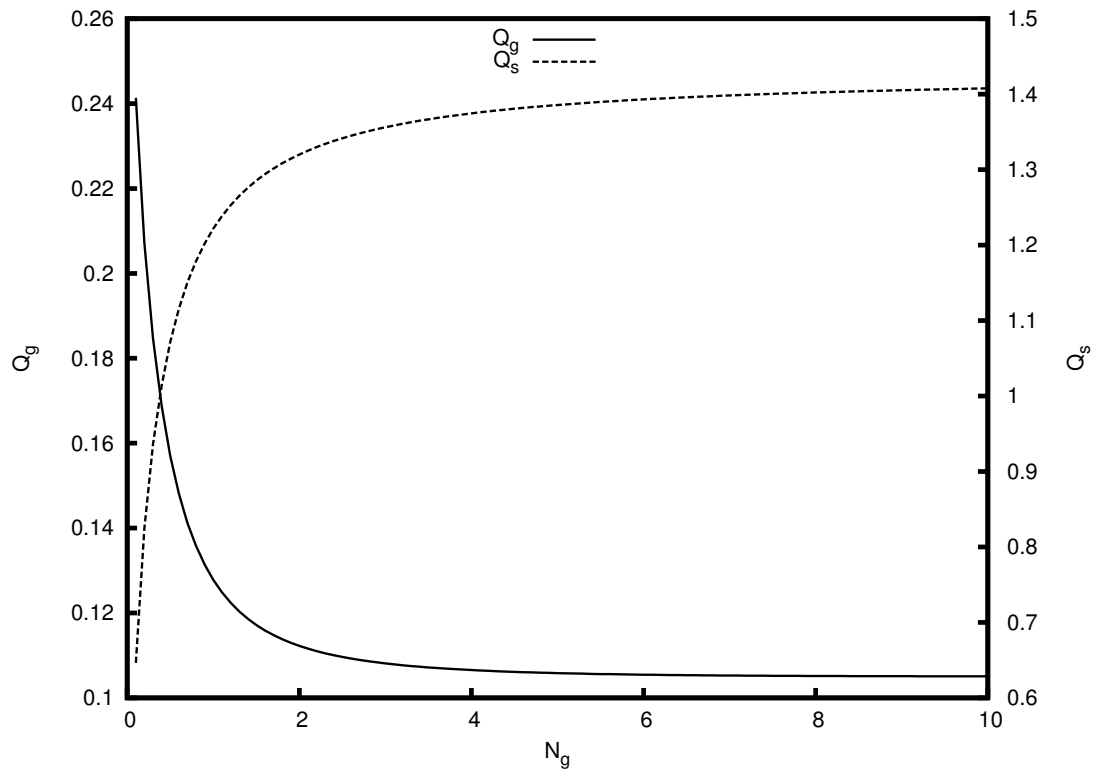


Figure 3.13 - Heat transfer at the wall $\times N_g$ with $\beta^* = 1.08$, $Pr = 0.7$, $\varphi = 0.7$, $T_0 = 1.6$ and $\Gamma = 50.0$.

The distinct flow behavior for different β must be considered for calculations of the wall heat exchange and wall shear. We utilized a bed-of-particles model for the porous matrix, such that $\beta \sim 1/(\bar{a}d_p^2)$. Generally speaking, $\beta \sim 1/K$, with K the dimensionless medium permeability (Darcy number). The existence of a singular point when $\beta = 1$ suggests that a different model for the pressure could be used in this case.

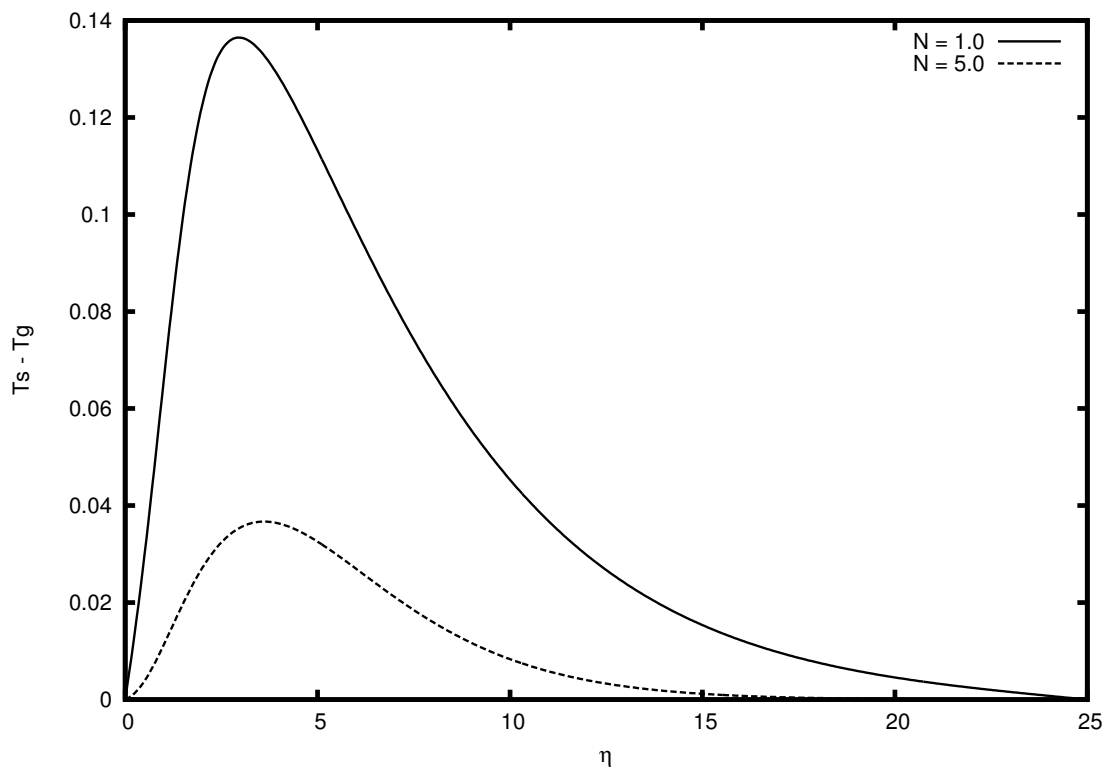


Figure 3.14 - Temperature difference for $N_g = 1.0$ and $N_g = 5.0$ with $\beta^* = 1.08$, $Pr = \varphi = 0.7$, $T_0 = 1.6$ and $\Gamma = 50.0$

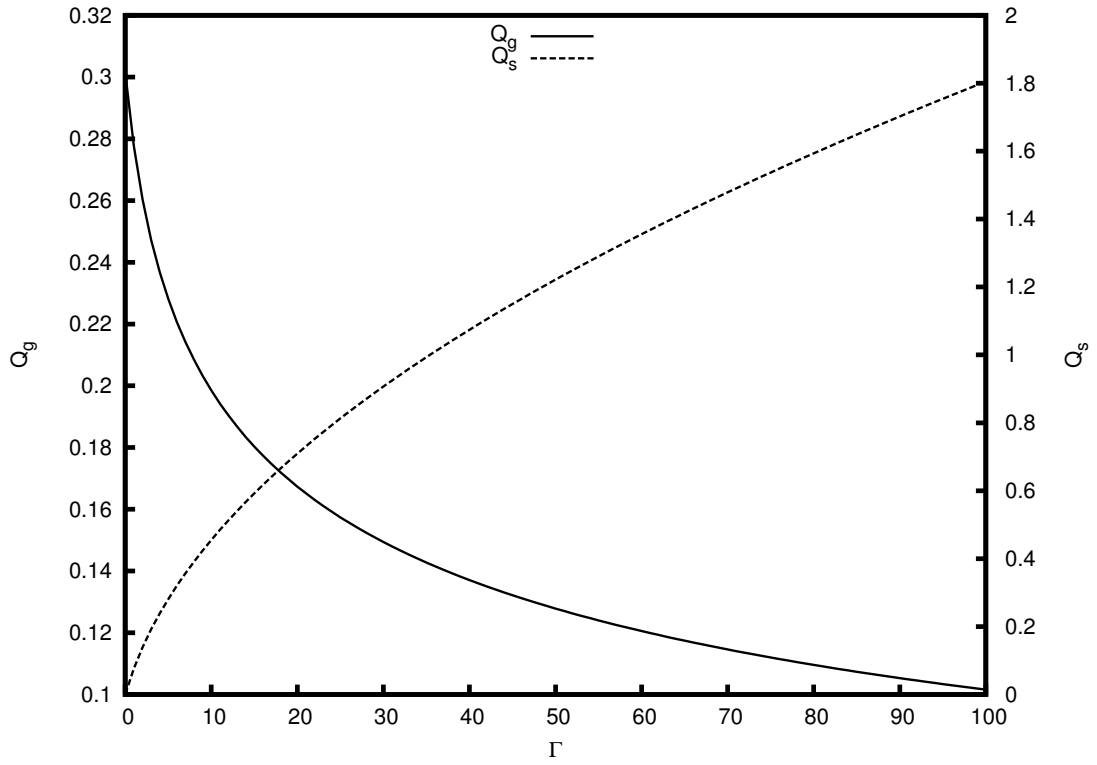


Figure 3.15 - Heat transfer at the wall $\times \Gamma$ with $\beta^* = 1.08$, $Pr = \varphi = 0.7$, $N_g = 1.0$ and $T_0 = 1.6$

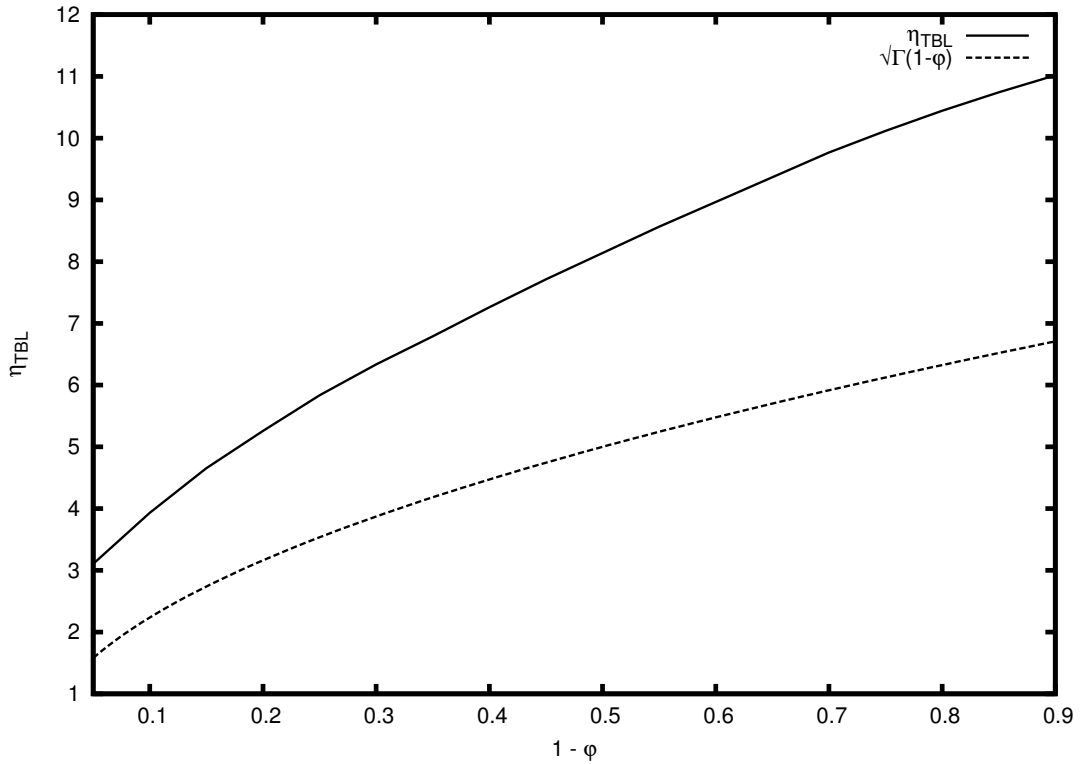


Figure 3.16 - $\eta_{TBL} \times (1 - \varphi)$ with $\beta^* = 1.08$, $Pr = 0.7$, $N_g = 1.0$, $T_0 = 1.6$ and $\Gamma = 50.0$

4 PHASE CHANGE PROBLEM: STAGNATION-POINT FLOW AGAINST A LIQUID POOL

In this Chapter we replace the impermeable wall by a pool of liquid. The injected gas is at a higher temperature than the liquid, that is at its boiling temperature. Then, a steady vaporization regime is analyzed. Since we do not consider chemical reaction to take place, the case analyzed here may be viewed as a frozen flow limit.

Studies concerning phase change in porous media are also extensively found in the literature due to its vast amount of possible applications (YORTSOS; STUBOS, 2001). Drying processes (DAURELLE et al., 1998), geothermal systems (WOODS, 1999) and nuclear safety issues are some examples of such system. The evaporation of a thin film of liquid water within a heated porous bed subjected to a stagnation-point flow was studied analytically (ZHAO, 1999). In that work, the coupled heat and mass transfer problem was analyzed in the proposed geometry. Local thermal equilibrium was considered, and the focus was on the parameters influence on the heat and mass transfer properties. The obtained results are of significance for the design of indirect evaporative air cooler systems.

Boiling in a saturated porous medium was analyzed by Ramesh and Torrance (1993) by considering a heat supply from below and a cooling from above. Using numerical methods, they analyzed the possible flow regimes with the consideration of a moving liquid/two-phase interface. The authors conducted a parametric study considering the liquid-phase Rayleigh number and the non-dimensional bottom heat flux. Their results recognized three different regimes: conduction-dominated for low Rayleigh number, convection-dominated for intermediary Rayleigh number, and oscillatory convection for high Rayleigh number. In the convection-dominated regime, as the non-dimensional bottom heat flux increases, transitions to multiple cell patterns were observed. The stability of the obtained solutions to perturbations was also conducted. The interphase heat exchange was considered fixed as a heat loss parameter.

Effects of local thermal non-equilibrium on the infiltration of a hot fluid into a cold porous medium was analyzed by Rees et al. (2008). In order to study this flow configuration, the moving thermal front resultant from the thermal non-equilibrium was analyzed. By performing a scale analysis and numerical simulations, the different manners in which the temperature fields evolve in time were discussed. It was found that the thickness of the thermal front is a function of the governing parameters (namely, the non-dimensional interphase heat transfer parameter, the

porosity-modified conductivity ratio and the diffusivity ratio). This has the implication that local thermal equilibrium is not equivalent to a single equation formulation of the energy equation. Their results for a large-time analysis showed that local thermal equilibrium is achieved in such limit, but in a solution different from that which would be obtained by an one-equation modeling. It was also observed the formation of a shock wave when the velocity of the infiltrating fluid was sufficiently large.

There is also a good amount of studies in the open literature concerning natural evaporation, specially concerning the analysis of drying of porous media. Such problem finds applications to areas such as wood, paper, and the textile industry. Il'ichev et al. (2008) studied the gravitational instability of the salinity profile during the evaporation of saline groundwater. The stability analysis concluded that the most significant effect controlling the stability is the permeability of the soil. The effects of the different characteristic length scales in the problem of evaporative drying of a porous medium was analyzed by Lehmann et al. (2008). By comparing the roles of gravity, capillarity and viscous dissipation forces, they deduced the characteristic length for the maximum hydraulically connected film region between the drying front and the surface. The characteristic lengths depend on the size range between the smallest and largest pores within the film region. For media with large pores sizes, the characteristic length is dominated by gravity and capillarity, and the viscous dissipation is negligible. For media with small pores sizes (fine-textured) it was shown that viscous dissipation may limit the maximum hydraulically connected distance between the drying front and the evaporating surface. The authors also conducted experiments with two types of sand in order to determine the characteristic lengths and the extent of the film region.

The situation when heat is supplied to the condensed phase by a hot impinging gas arise, for instance, in the steam injection process of thermal oil recovery (NARAYAN; WALSH, 1988; JABBOUR et al., 1996). When a well contains heavy oil, its recovery may be achieved by means of heat addition in the reservoir, increasing its temperature and lowering the oil viscosity and hence increasing its mobility. The initial (injection) temperature of the steam must be high.

Heavy-oils have low volatility, such that the enhancement of the vaporization rate caused by heat transport through the solid phase is the main responsible for its phase change. In the context of a constant-density model and in the limit $\Gamma \gg 1$ (asymptotically large solid-to-gas thermal conductivities ratio), a liquid of $l = O(\Gamma) \gg 1$ (very low volatility) was considered previously (KOKUBUN; FACHINI,

2012). It was shown that in this case, in order to have vaporization of the liquid, it was necessary that the difference between the injection temperature \bar{T}_∞ and the liquid boiling temperature \bar{T}_B is high. In that problem this condition was expressed as $(\bar{T}_\infty - \bar{T}_B)/\bar{T}_\infty = O(1)$.

In the present problem we consider $l = O(1)$, $\rho \neq 1$ (thermal expansion) and a large, but finite, value of Γ . These conditions are used in order to generalize the previous work (KOKUBUN; FACHINI, 2012) and it shown that the addition of a porous matrix enhances liquid vaporization, because it provides an additional heat source to the phase change process. This shows that porous-medium can be used to make vaporization of liquids more efficient (for instance, they can replace spraying-type nozzles, which are energy-consuming and requires larger volumes for operation).

4.1 Physical problem

Instead of an impermeable wall at $\eta = 0$ (as in Chapter 3), we have a pool of liquid as depicted in Fig. 4.1.

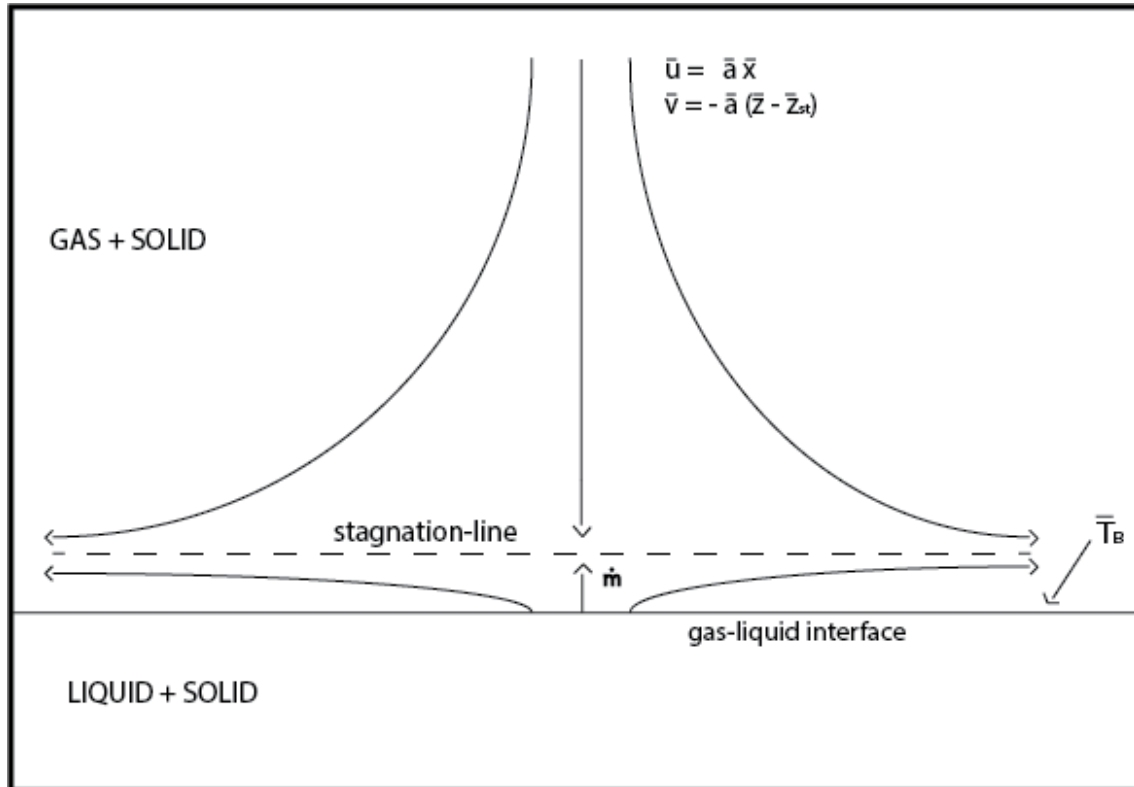


Figure 4.1 - Schematic of the problem.

The injected gas is at a high temperature, a condition that makes gas phase provide heat to the liquid phase-change. The existence of a solid phase enhances heat transport to larger regions, including to inside the liquid pool. Then, the heat exchange between liquid and solid below the gas-liquid interface is an additional heat source that enhances vaporization of the liquid.

In the present case, the coupling between flow and temperature fields due to thermal expansion enhances the heat fluxes near the surface, which enhances the liquid vaporization rate. Since the gas temperature decreases from injection to the surface, its density increases, a process that compresses the flow, increasing its vertical velocity and pushing the stagnation-point closer to the liquid surface. Velocity overshoot is not observed because it only occurs when there is a temperature in the viscous boundary-layer higher than the free stream temperature, a feature that happens for the previous case (hot wall) and for the next, when a flame sheet in the boundary-layer is accounted, but not for the present frozen flow.

4.2 Mathematical formulation

The governing equation for Y_O is not necessary, and the chemical reaction term in the equations for Y_F and T_g is set to zero. Then, the non-dimensional governing equations for this problem in the gas-solid region, $\eta > 0$, are given by

$$Pr \frac{d^3 f}{d\eta^3} + f \frac{d^2 f}{d\eta^2} - \left(\frac{df}{d\eta} \right)^2 - \beta T_g^2 \frac{df}{d\eta} = -T_g (1 + \beta), \quad (4.1)$$

$$Pr \frac{d^2(fT_g)}{d\eta^2} + f \frac{d(fT_g)}{d\eta} - \beta T_g^3 f = (1 - \beta) \frac{dF}{d\eta}, \quad (4.2)$$

$$-f \frac{dY_F}{d\eta} - \frac{\varphi}{L_F} \frac{d^2 Y_F}{d\eta^2} = 0, \quad (4.3)$$

$$-f \frac{dT_g}{d\eta} - \varphi \frac{d^2 T_g}{d\eta^2} = T_g N_g (T_s - T_g), \quad (4.4)$$

$$- \Gamma(1 - \varphi) \frac{d}{d\eta} \left(\frac{1}{T_g} \frac{dT_s}{d\eta} \right) = -T_g N_g (T_s - T_g). \quad (4.5)$$

For the liquid region, $z < 0$, since the liquid is at its boiling temperature, the only governing equation to be solved is the one for the solid, and it is given by

$$- \Gamma(1 - \varphi) \frac{d^2 T_s}{dz^2} = -N_l (T_s - T_B). \quad (4.6)$$

Injection conditions for $\eta \rightarrow \infty$ are given by

$$\frac{df}{d\eta} = 1, \quad T_s = T_g = 1, \quad Y_F = 0. \quad (4.7)$$

At the surface $\eta = 0$, we have the gas at thermal equilibrium with the liquid (both at the liquid boiling temperature T_B) and the no-slip condition (zero tangential velocity, which is valid when $\rho/\rho_l \ll 1$). Also, mass conservation relates the vertical component of the velocity with the vaporization rate. These conditions for $\eta = 0$ are given by

$$T_g = T_B, \quad \frac{df}{d\eta} = 0, \quad -f(0) = \dot{m}. \quad (4.8)$$

The solid temperature at the surface $T_{s0} > T_B$ is an unknown to be obtained from the continuity of the solid phase heat flux at the gas-liquid interface, given by

$$\frac{1}{T_B} \frac{dT_s}{d\eta} \Big|_{0^+} = \frac{dT_s}{dz} \Big|_{0^-}. \quad (4.9)$$

Reservoir condition, $z \rightarrow -\infty$, is given by

$$T_s = T_B. \quad (4.10)$$

At the interface $\eta = z = 0$, species and energy conservation gives

$$\frac{\varphi}{L_F} \frac{dY_F}{d\eta} \Big|_0 = (1 - Y_{F0})f(0), \quad (4.11)$$

$$\varphi \frac{dT_g}{d\eta} \Big|_{0^+} + N_l \int_{-\infty}^{0^-} (T_s - T_B) dz = \dot{m} l T_B, \quad (4.12)$$

where $l \equiv L/(c_p \bar{T}_B)$ is the dimensionless latent heat of vaporization. The definition of l with respect to \bar{T}_B instead of \bar{T}_∞ makes the effective latent heat of vaporization to be given by $l T_B$. This definition was made this way in order to keep l fixed for different injection temperatures.

Species conservation at the interface 4.11 determines Y_{F0} , while energy conservation 4.12 determines the vaporization rate \dot{m} .

4.2.1 Liquid-solid region

In the liquid-solid region, the solution for the solid temperature equation is straightforward obtained as

$$T_s(z) = T_B + b_0 e^{\sqrt{N_l/(\Gamma(1-\varphi))}z}, \quad (4.13)$$

where the condition $T_s \rightarrow T_B$ for $z \rightarrow -\infty$ was used and b_0 is determined from the continuity of the solid heat flux at the interface 4.9, such that

$$b_0 = \frac{1}{T_B} \left. \frac{dT_s}{d\eta} \right|_{0+} \sqrt{\frac{\Gamma(1-\varphi)}{N_l}}. \quad (4.14)$$

Then, the solid temperature in the liquid-solid region is given by

$$T_s(z) = T_B + \left(\frac{1}{T_B} \left. \frac{dT_s}{d\eta} \right|_{0+} \sqrt{\frac{\Gamma(1-\varphi)}{N_l}} \right) e^{\sqrt{N_l/(\Gamma(1-\varphi))}z}. \quad (4.15)$$

The temperature difference between solid and liquid at the surface ($T_{s0} - T_B$) is proportional to the solid heat flux from the gas-solid region $dT_s/d\eta|_{0+}$.

The solid temperature at the interface is then given by

$$T_{s0} = T_B + \frac{1}{T_B} \left. \frac{dT_s}{d\eta} \right|_{0+} \sqrt{\frac{\Gamma(1-\varphi)}{N_l}} \quad (4.16)$$

Using 4.16 in the energy conservation at the interface 4.12 gives the expression for the vaporization rate as

$$\dot{m} = \frac{T_B^{-1}}{l} \left\{ \varphi \left. \frac{dT_g}{d\eta} \right|_{0+} + \frac{\Gamma(1-\varphi)}{T_B} \left. \frac{dT_s}{d\eta} \right|_{0+} \right\}. \quad (4.17)$$

Note that the heat flux from the solid phase enhances the vaporization rate. This enhancement is proportional to the solid matrix volume $(1-\varphi)$ and to the solid-to-gas thermal conductivities ratio Γ . For $\varphi = 1$ we recover the result for a non-confined problem.

The expression 4.17 for the vaporization rate could be obtained by first integrating Eq. 4.6 from $z \rightarrow -\infty$ to $z = 0$. Noting that $dT_s/dz \rightarrow 0$ when $z \rightarrow -\infty$, we obtain

from the continuity of the solid phase heat flux at the surface 4.9 that

$$N_l \int_{-\infty}^{0^-} (T_s - T_B) dz = \frac{\Gamma(1 - \varphi)}{T_B} \frac{dT_s}{d\eta} \Big|_{0^+}, \quad (4.18)$$

which shows that all the heat provided to the liquid-solid region is given to the phase change of the liquid. Since we consider $T_l = T_B$ everywhere, this result is straight-forward.

Species conservation 4.11 determines the fuel mass fraction at the surface Y_{F0} as

$$Y_{F0} = 1 + \frac{\varphi}{L_F \dot{m}} \frac{dY_F}{d\eta} \Big|_0. \quad (4.19)$$

In order to numerically solve this problem, values for the eigenvalue \dot{m} and for the unknowns T_{s0} and Y_{F0} are first guessed and the profiles that obey these guessed values are obtained by marching in the pseudo-time until the steady-state is achieved (we consider the steady-state to be achieved when $\partial/\partial t \sim 10^{-5}$). Then, \dot{m} , T_{s0} and Y_{F0} are calculated through the discretized versions of Eqs. 4.16, 4.17 and 4.19. If the difference between the calculated and the guessed values is greater than 10^{-5} , the guesses are updated and a new iteration is made. A constant mesh spacing of $\Delta\eta = 0.05$ was used. Decreasing $\Delta\eta$ below this value showed no significant influence on the vaporization rate $-f(0)$, such that $\Delta\eta = 0.05$ was considered appropriated.

4.3 Results

In order to obtain characteristic profiles we consider the liquid to be water and an impinging air, with its properties evaluated at 293 K, such that $l = 5.826$. A mean pore diameter $\bar{d}_p = 5 \text{ mm}$ is considered. Then, characteristic profiles of temperatures, velocities and vapor mass fraction are obtained for $Pr = \varphi = 0.7$, $\Gamma = 50.0$, $T_B = 0.333$ (impinging jet at a temperature three times higher than the liquid boiling temperature), $\beta^* = 1.08$ and $N_g = N_l = L_F = 1.0$ and shown in Figs. 4.2, 4.3 and 4.4, respectively, where we also compare with results of the incompressible model (constant density). Profiles are given in the physical z plane.

From the state equation $\rho = 1/T_g$, the gas density increases from injection to the liquid surface, as the temperature decreases from injection to the liquid surface. This increase on the gas density compress the flow, enhancing its vertical velocity, when compared to the constant-density case, and pushing the stagnation-point closer to the surface. In addition, due to the high value of the temperature field, which en-

hances the heat flux at the surface, the vaporization rate for the compressible case is higher when compared to the incompressible case. For the set of parameters considered, we have $\dot{m} = 0.246$ and $\dot{m} = 0.185$ for the compressible and incompressible cases, respectively. Consequently, the vapor mass fraction at the surface is higher in the compressible case, as seen in Fig. 4.4. We obtain $Y_{F0} = 0.464$ and $Y_{F0} = 0.335$ for compressible and incompressible cases, respectively. The vapor is transported by convection and diffusion from the surface to the stagnation-point, and after that only by diffusion against the incoming flow. Since the flow velocity in the incompressible case is lower than in the case with thermal expansion, the vapor is able to diffuse more above the stagnation-point in the incompressible case, as one can see in Fig. 4.4.

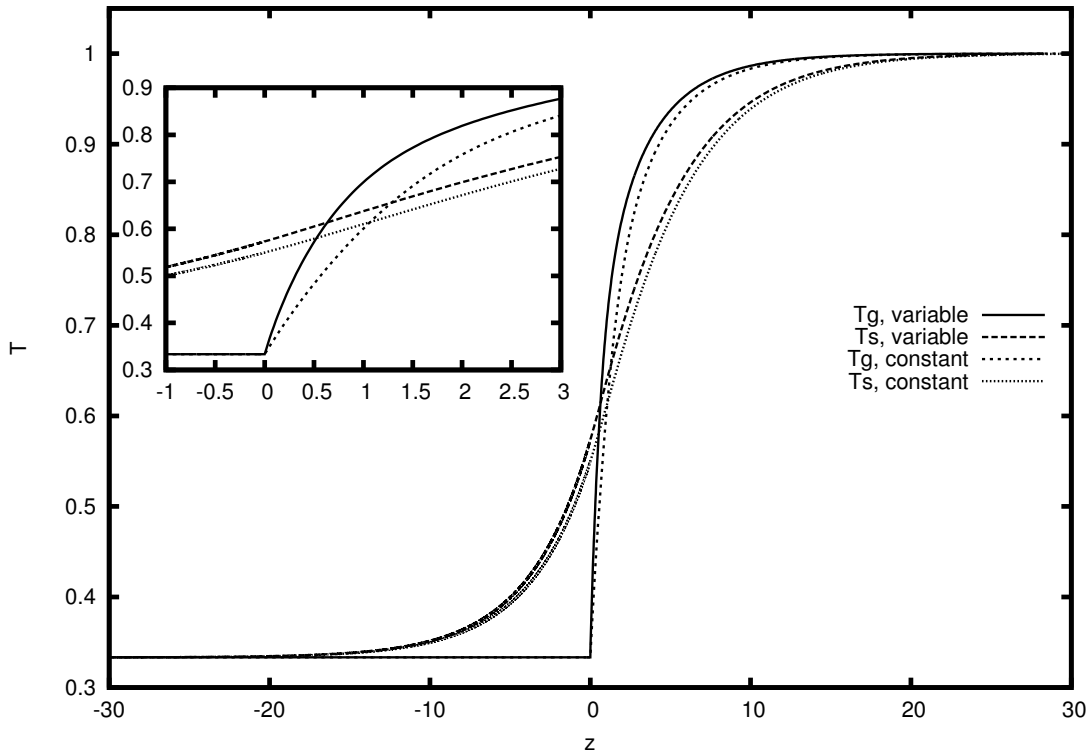


Figure 4.2 - Temperature profiles with and without thermal expansion for $\beta^* = 1.08$, $N_g = N_l = L_F = 1.0$, $Pr = \varphi = 0.7$, $\Gamma = 50.0$ and $T_B = 0.333$.

Physically, it is expected that $N_l > N_g$ because of the following: the contact time between gas and solid is smaller than the contact time between liquid and solid, the density, viscosity, heat capacity and thermal conductivity of the liquid are much higher than of the gas. The consideration of $N_l = N_g = 1.0$ is made to obtain char-

acteristic profiles, but the overall physical behavior will be the same if we consider the more realistic case of $N_l > N_g$. From the solid temperature in the liquid-solid region, Eq. 4.15, we can see that the thickness of the thermal non-equilibrium region is proportional to $\sqrt{N_l^{-1}}$, such that it decreases for increasing values of N_l . In the asymptotic limit $N_l \gg 1$, $T_s \rightarrow T_B$, such that no heat exchange between liquid and solid would occur. However, from the integral term in Eq. 4.12 we can see that the heat exchange between liquid and solid is linearly dependent on N_l . Then, in the asymptotic limit of $N_l \gg 1$ the vaporization rate scales with $\sqrt{N_l}$. This trend may be seen in Fig. 4.5, where we show the influence of N_l on the vaporization rate \dot{m} and fuel mass fraction at the surface Y_{F0} . Figure 4.6 shows the temperature profiles for $N_l = 1.0$ and $N_l = 100.0$, where one can see that the thickness of the thermal non-equilibrium region between liquid and solid when $N_l = 100.0$ is smaller than when $N_l = 1.0$.

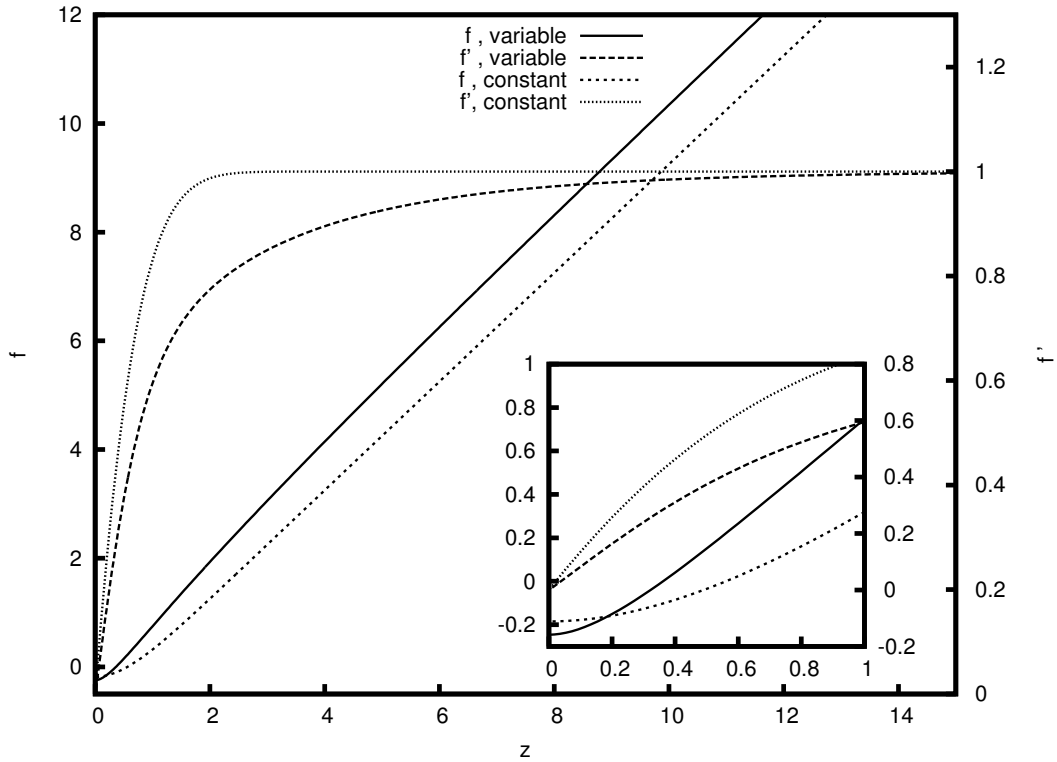


Figure 4.3 - Velocities profiles with and without thermal expansion for $\beta^* = 1.08$, $N_g = N_l = L_F = 1.0$, $Pr = \varphi = 0.7$, $\Gamma = 50.0$ and $T_B = 0.333$.

Gas and solid heat fluxes at the surface determines the vaporization rate (see Eq.

4.17) and they are given respectively by

$$Q_g = \varphi \left. \frac{dT_g}{d\eta} \right|_0, \quad Q_s = \Gamma \frac{(1 - \varphi)}{T_B} \left. \frac{dT_s}{d\eta} \right|_0. \quad (4.20)$$

A decrease on the medium porosity φ leads to an increase on the solid heat flux, which enhances T_{s0} , leading to higher values of the vaporization rate \dot{m} and, consequently, increasing the vapor mass fraction at the surface Y_{F0} . These features can be seen in Fig. 4.7, where we show \dot{m} , T_{s0} and Y_{F0} variations with the porosity φ . The increase on the gas heat flux at the surface Q_g and the decrease on the solid heat flux Q_s with the porosity φ is shown in Fig. 4.8.

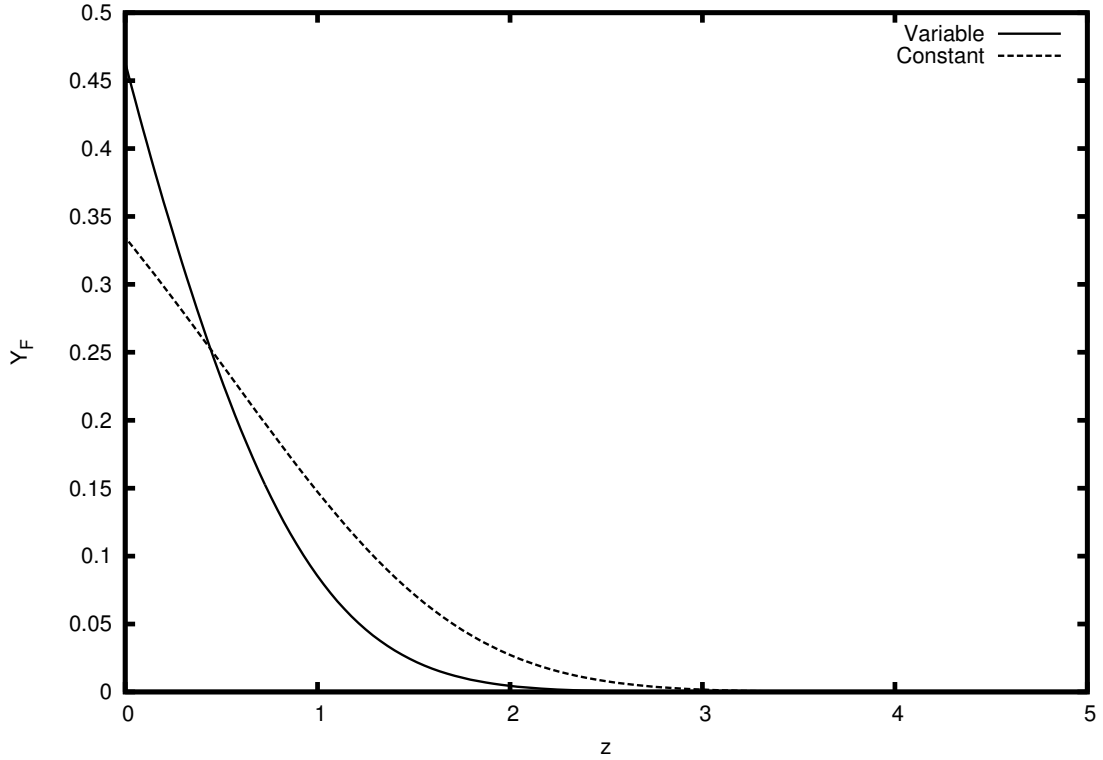


Figure 4.4 - Vapor mass fraction profiles with and without thermal expansion for $\beta^* = 1.08$, $N_g = N_l = L_F = 1.0$, $Pr = \varphi = 0.7$, $\Gamma = 50.0$ and $T_B = 0.333$.

As expected, an increase on the injection temperature (measured by $1 - T_B$) leads to an increase on the vaporization rate \dot{m} and vapor mass fraction at the surface Y_{F0} , as shown in Fig. 4.9. The increase on the solid temperature at the surface is measured as T_{s0}/T_B , instead of only T_{s0} , because the dimensionalization is made with respect to the injection temperature. Then, T_{s0} measures an increase in terms

of \bar{T}_∞ , but T_{s0}/T_B is an absolute measure of the increase of the solid temperature at the surface.

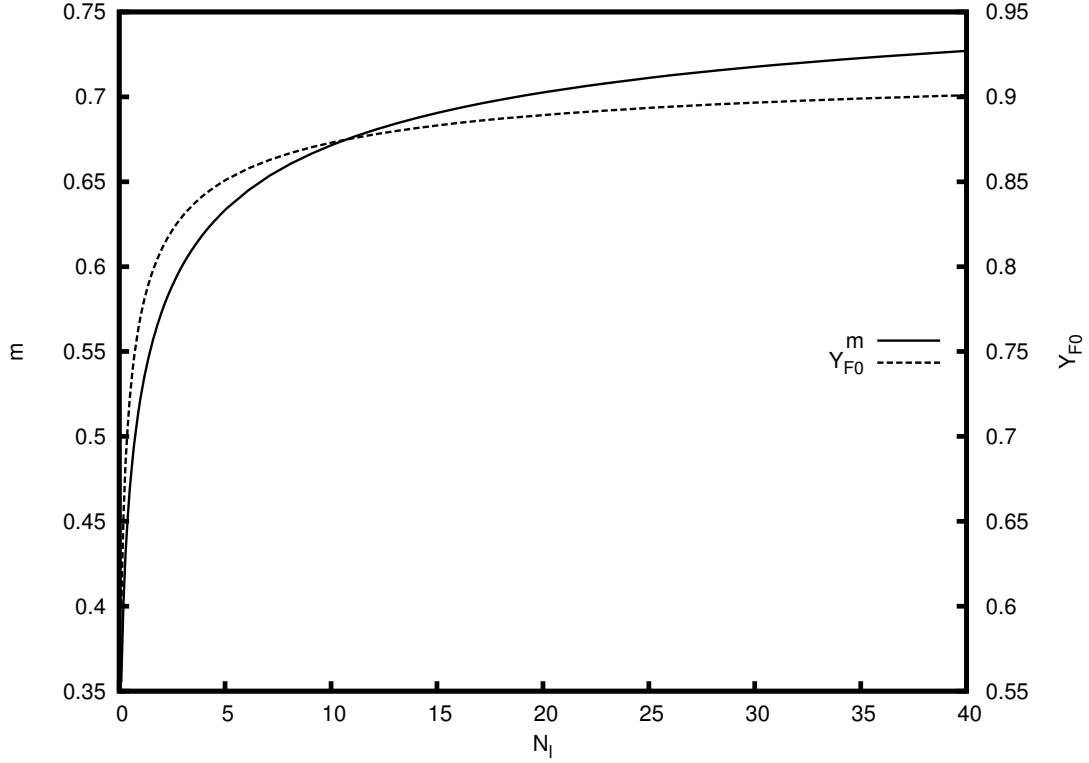


Figure 4.5 - $\{\dot{m}, Y_{F0}\} \times N_l$ with $\beta^* = 1.08$, $N_g = L_F = 1.0$, $Pr = \varphi = 0.7$, $\Gamma = 50.0$ and $T_B = 0.333$.

Higher values of the solid-to-gas thermal conductivities ratio Γ leads to higher values of the vaporization rate \dot{m} , solid temperature at the surface T_{s0} and vapor mass fraction at the surface Y_{F0} , as seen in Fig. 4.10. This occurs because when Γ is large, the heat conduction through the solid phase is large, leading to a higher value of its temperature at the gas-liquid surface, which consequently increase the vaporization rate and the vapor mass fraction at the surface. The contributions to the vaporization rate come from the gas and solid heat fluxes at the surface, as seen in Eqs. 4.17 and 4.20. For increasing values of Γ , the gas contribution decreases, while the solid increases, as one can see in Fig. 4.11.

Increasing values of N_g leads to increasing values of the vaporization rate \dot{m} , as one can see in Fig. 4.12. For $N_g = 0$ the vaporization occur only because of the gas-liquid heat exchange at the surface. As N_g starts to increase, the solid phase heat flux at

the interface increases, which decreases the gas phase heat flux at the interface. Since the solid thermal conductivity is much higher than the gas thermal conductivity, the vaporization rate increases as the solid phase contribution to the vaporization rate increases. As N_g increase further, the intensification of the interphase heat exchange increases gas temperature and decreases solid temperature, leading to an increase on the gas phase heat flux at the surface and to a decrease on the solid phase heat flux at the surface. This behavior makes the solid temperature at the surface to present a maximum, as one can see in Fig. 4.12. In Fig. 4.13 we show the phases heat flux with respect to N_g .

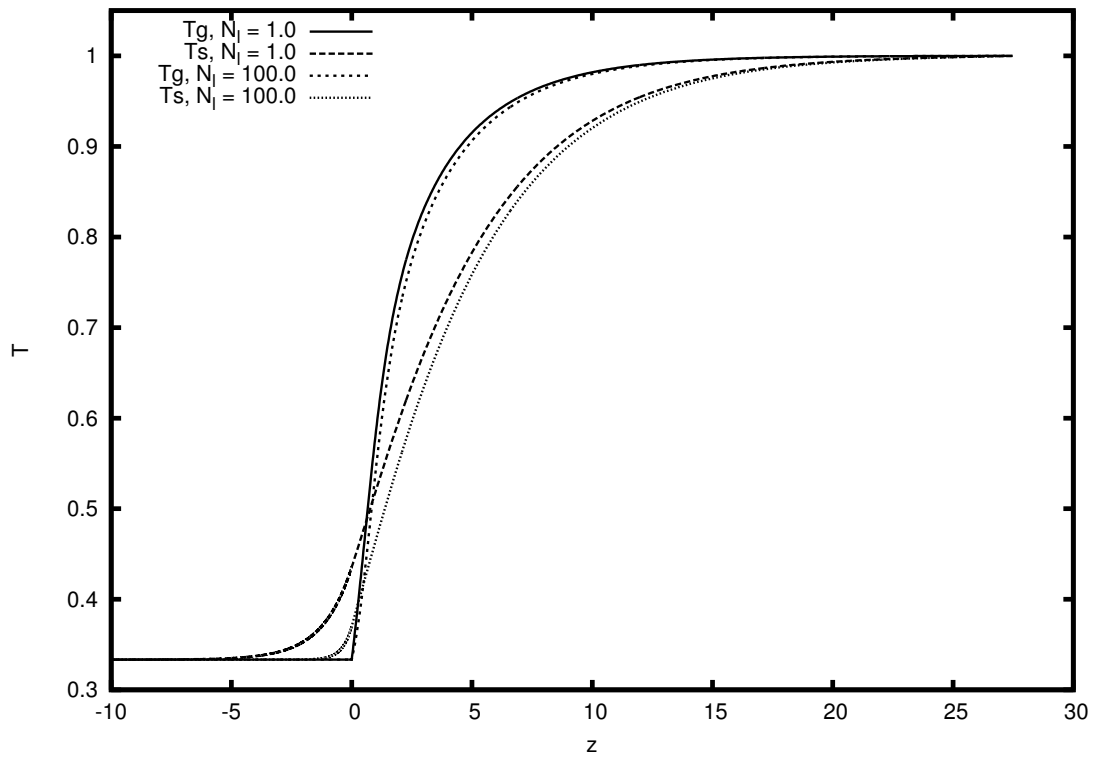


Figure 4.6 - Temperature profiles for $N_l = \{1.0, 100.0\}$, with $\beta^* = 1.08$, $N_g = L_F = 1.0$, $Pr = \varphi = 0.7$, $\Gamma = 50.0$ and $T_B = 0.333$.

The vapor Lewis number L_F influence only the vapor mass fraction at the surface Y_{F0} because it changes the concentration of Y_F near $\eta = 0$. If the vapor Lewis number increases, heat diffusion becomes more relevant than mass diffusion, which enhances the vapor mass fraction at the surface Y_{F0} , as shown in Fig. 4.14.

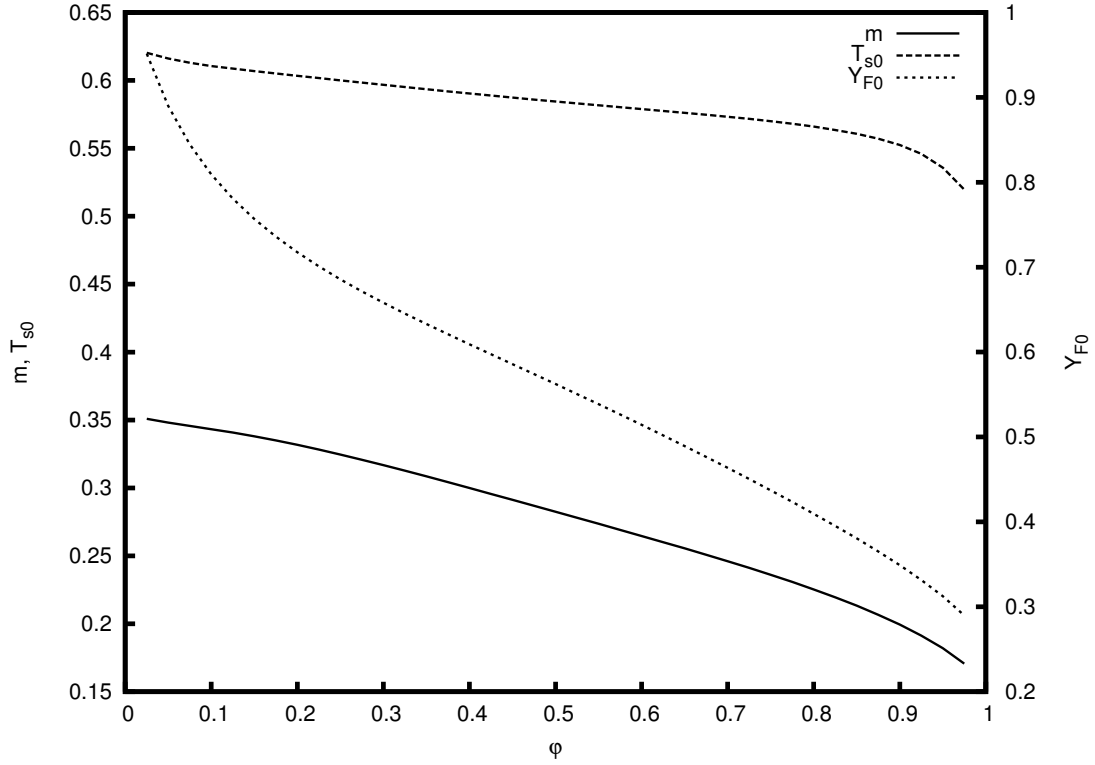


Figure 4.7 - $\{\dot{m}, T_{s0}, Y_{F0}\} \times \varphi$, with $\beta^* = 1.08$, $N_g = N_l = L_F = 1.0$, $Pr = 0.7$, $\Gamma = 50.0$ and $T_B = 0.333$.

4.4 Conclusions

In this Chapter we analyzed a hot impinging flow against a liquid surface, which vaporizes due to the high temperature of the incoming gas flow. The gas-liquid system is immersed in an inert porous matrix. Since the solid phase has a higher thermal conductivity, when compared to the gas phase, the addition of the porous matrix enhances heat transport to large regions, including into the liquid, providing an extra heat source to the phase change process. Then, the vaporization rate is enhanced by the porous matrix. The increase on the vaporization rate is proportional to the solid volume $(1 - \varphi)$, as seen in Eq. 4.17 and Fig. 4.7.

From $\rho = 1/T_g$, thermal expansion compresses the flow from injection (high temperature) to the liquid surface (which is at the liquid boiling temperature), pushing the stagnation-point closer to the surface. The enhancement of the temperatures due to thermal expansion increase the vaporization rate and the higher flow velocity difficult the transport of vapor from the liquid surface against the incoming jet (mass diffusion above the stagnation-point).

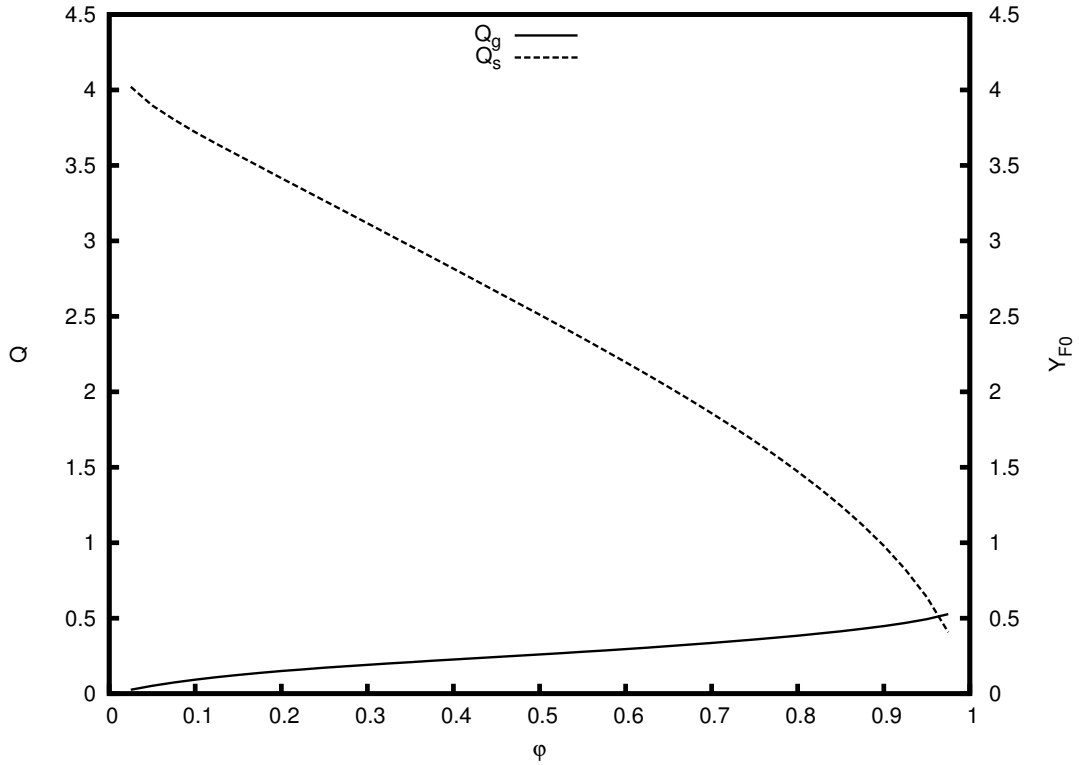


Figure 4.8 - $\{Q_g, Q_s\} \times \varphi$, with $\beta^* = 1.08$, $N_g = N_l = L_F = 1.0$, $Pr = 0.7$, $\Gamma = 50.0$ and $T_B = 0.333$.

The thickness of the thermal non-equilibrium region between liquid and solid diminishes for increasing values of the liquid-solid interphase heat exchange coefficient N_l , as one can see in Fig. 4.6. The thickness of this thermal non-equilibrium region is proportional to $\sqrt{N_l^{-1}}$. Increasing values of N_l increases the vaporization rate, as seen in Eq. 4.12 and Fig. 4.5. In the asymptotic limit of $N_l \gg 1$, the solid temperature T_s in the liquid-solid region approaches the liquid boiling temperature T_B and the vaporization rate is proportional to $\sqrt{N_l}$.

Higher values of Γ leads to higher values of the vaporization rate, as the solid phase heat flux at the surface depends linearly on Γ . Since Γ measures the difference between heat transport in solid and gas phases, high values of Γ means that heat is transported through the solid phase to larger regions. Then, heat exchange between gas and solid heats the gas at larger distances when Γ is large.

For increasing values of N_g , the coupling between phases increase the vaporization rate due to the high value of the solid phase thermal conductivity when compared to the gas phase thermal conductivity. When N_g increase enough, the high interphase

heat exchange between phases increase the gas temperature profile, while decrease the solid temperature profile.

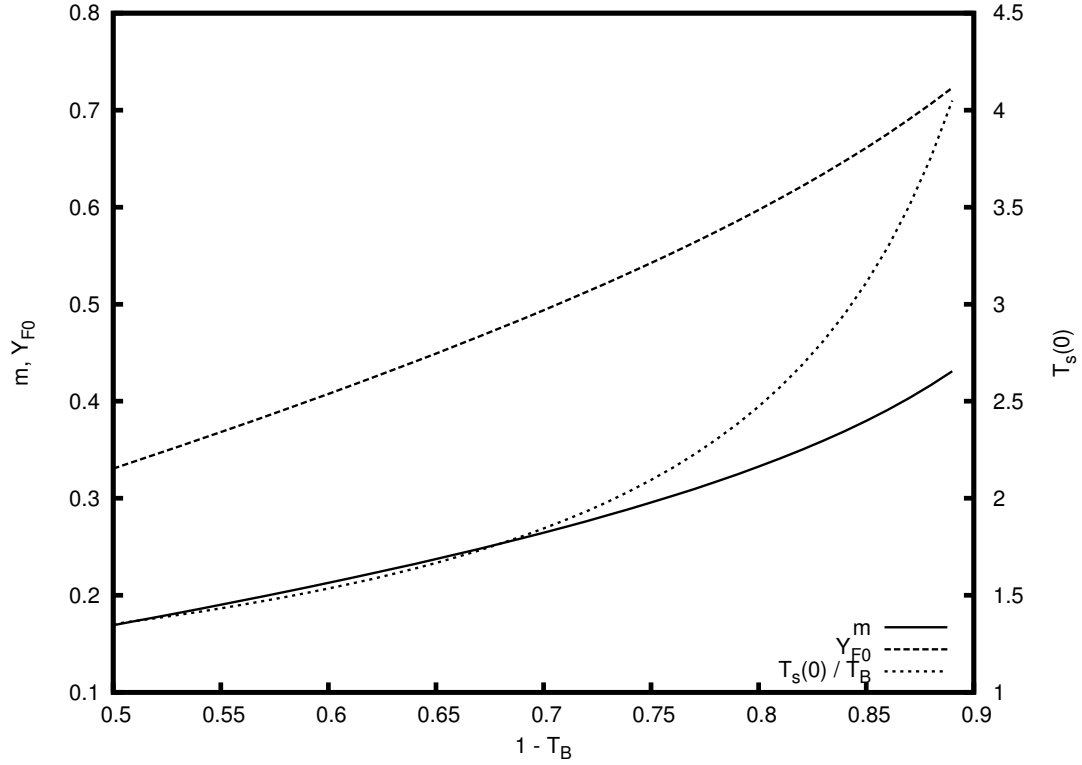


Figure 4.9 - $\{\dot{m}, T_{s0}, Y_{F0}\} \times (1 - T_B)$, with $\beta^* = 1.08$, $N_g = N_l = L_F = 1.0$, $Pr = \varphi = 0.7$ and $\Gamma = 50.0$.

The vapor Lewis number L_F modifies the concentration of vapor at the surface. Increasing values of L_F lead to increasing values of Y_{F0} , because we are increasing heat diffusion with respect to mass diffusion.

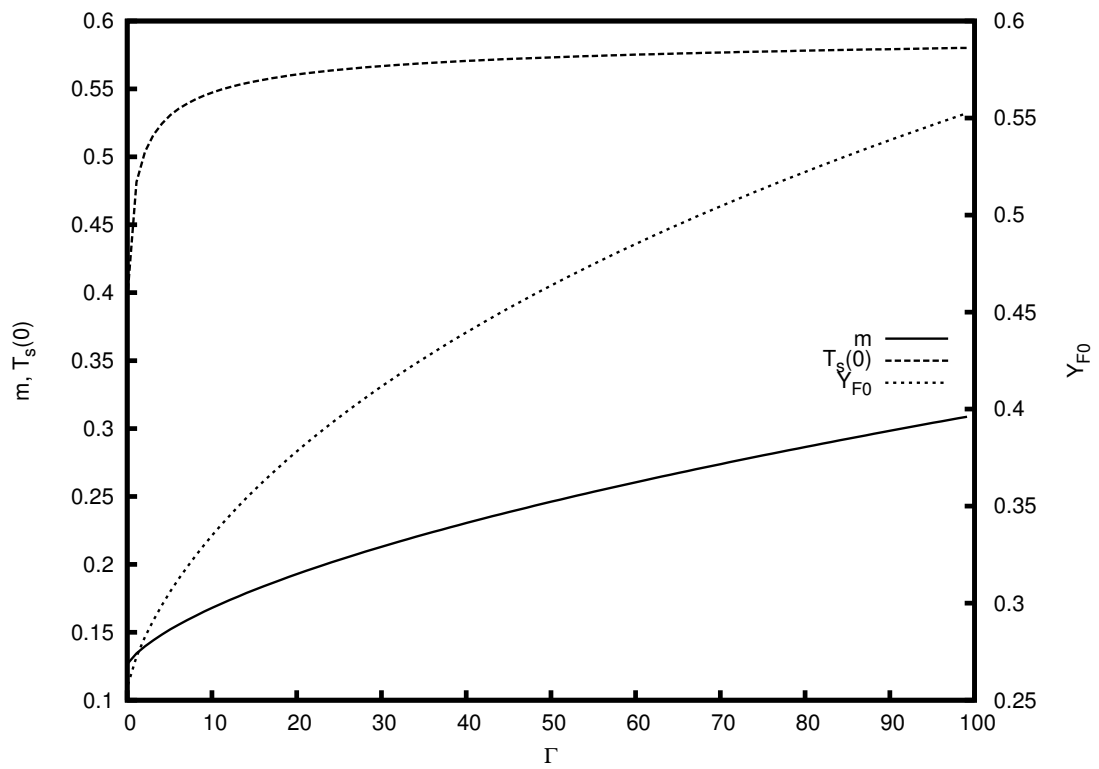


Figure 4.10 - $\{\dot{m}, T_{s0}, Y_{F0}\} \times \Gamma$, with $\beta^* = 1.08$, $N_g = N_l = L_F = 1.0$, $Pr = \varphi = 0.7$ and $T_B = 0.333$.

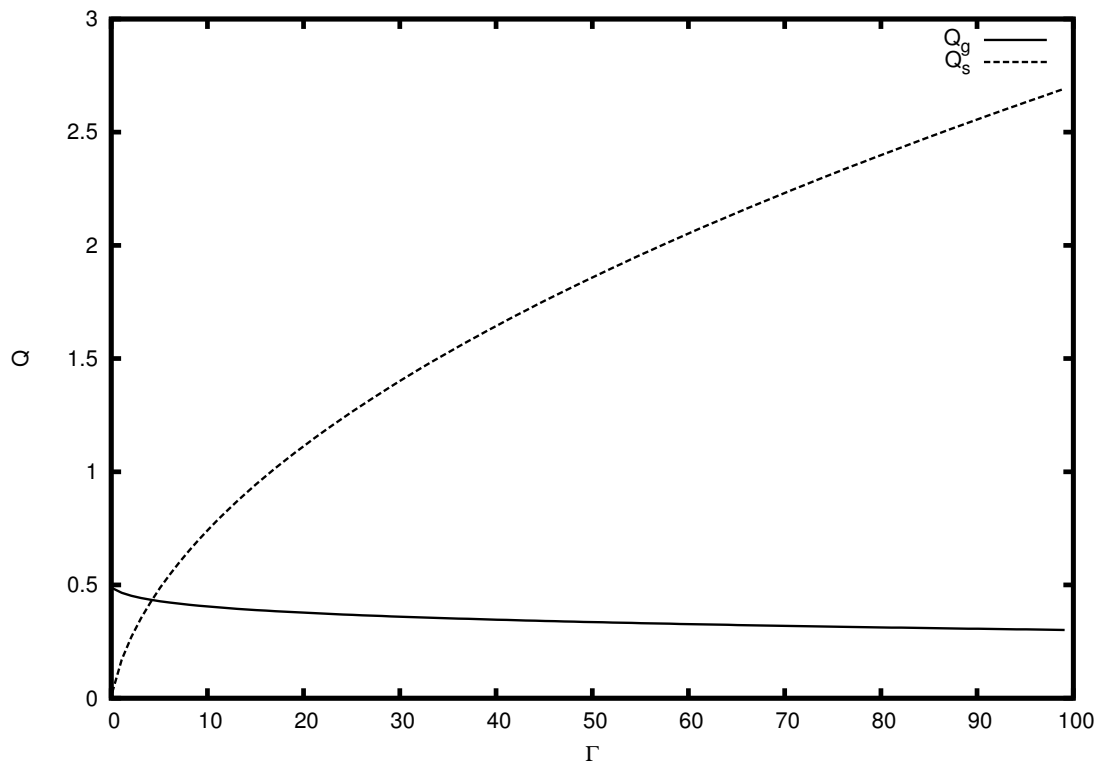


Figure 4.11 - $\{Q_g, Q_s\} \times \Gamma$, with $\beta^* = 1.08$, $N_g = N_l = L_F = 1.0$, $Pr = \varphi = 0.7$ and $T_B = 0.333$.

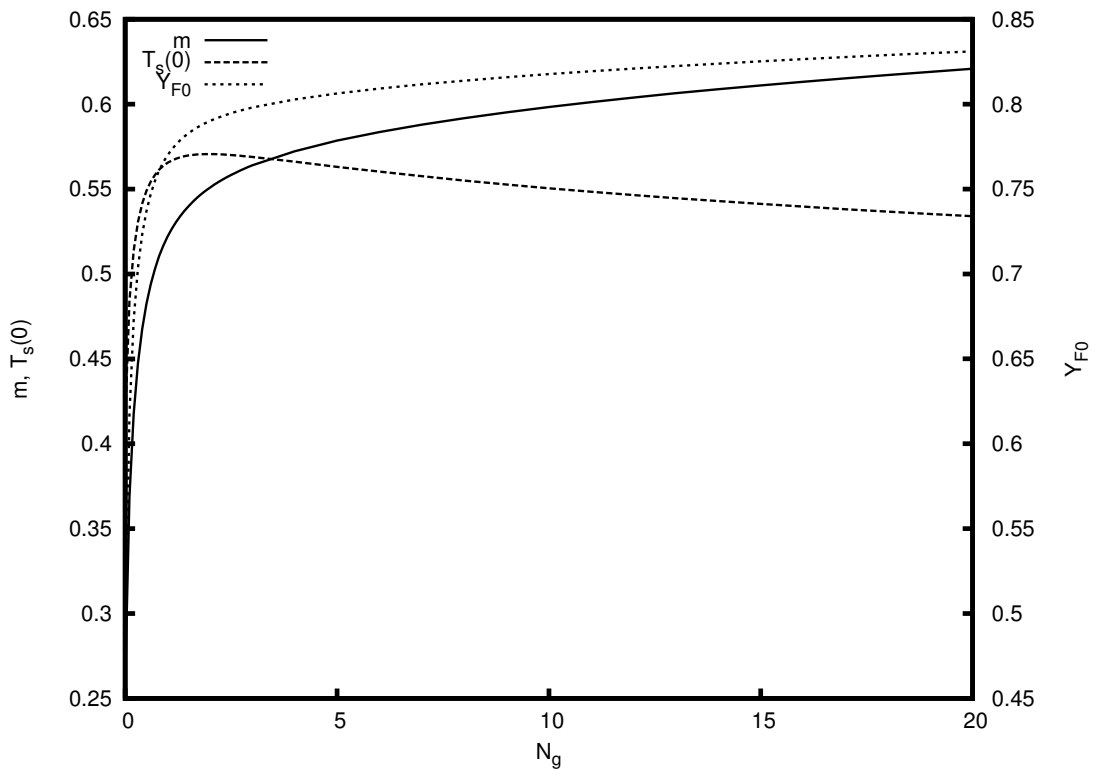


Figure 4.12 - $\{\dot{m}, T_{s0}, Y_{F0}\} \times N_g$, with $\beta^* = 1.08$, $N_l = L_F = 1.0$, $Pr = \varphi = 0.7$, $T_B = 0.333$ and $\Gamma = 50.0$.

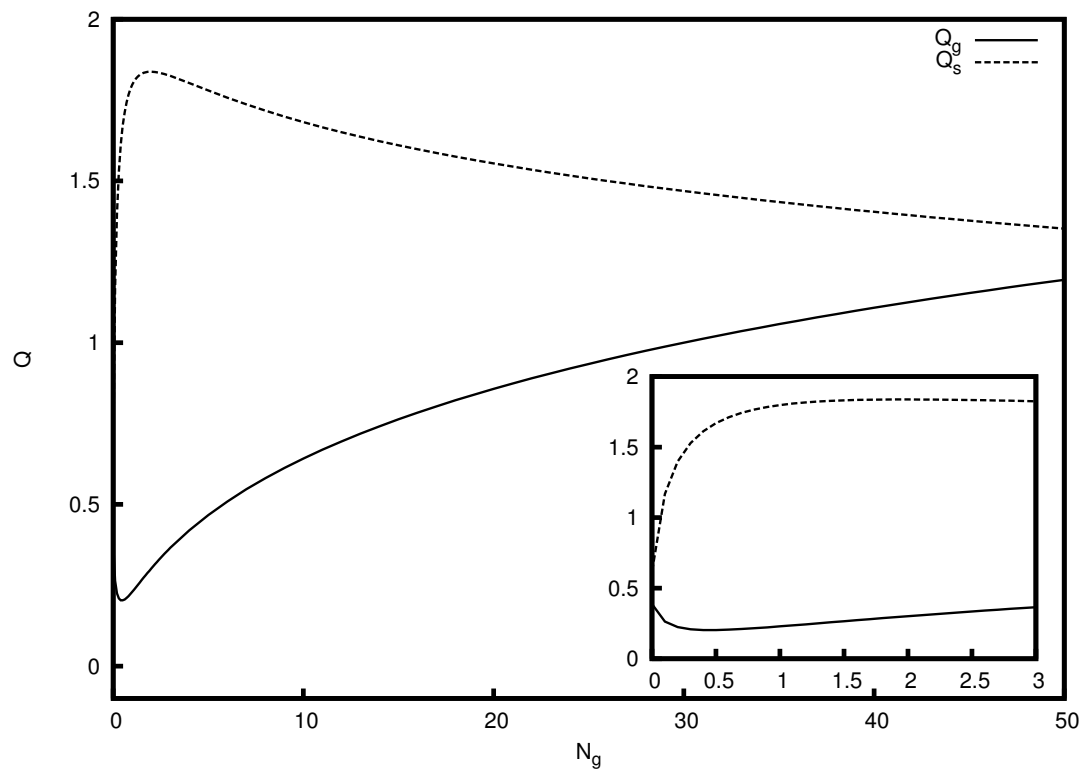


Figure 4.13 - $\{Q_g, Q_s\} \times N_g$ with $\beta^* = 1.08$, $N_l = L_F = 1.0$, $Pr = \varphi = 0.7$, $T_B = 0.333$ and $\Gamma = 50.0$.

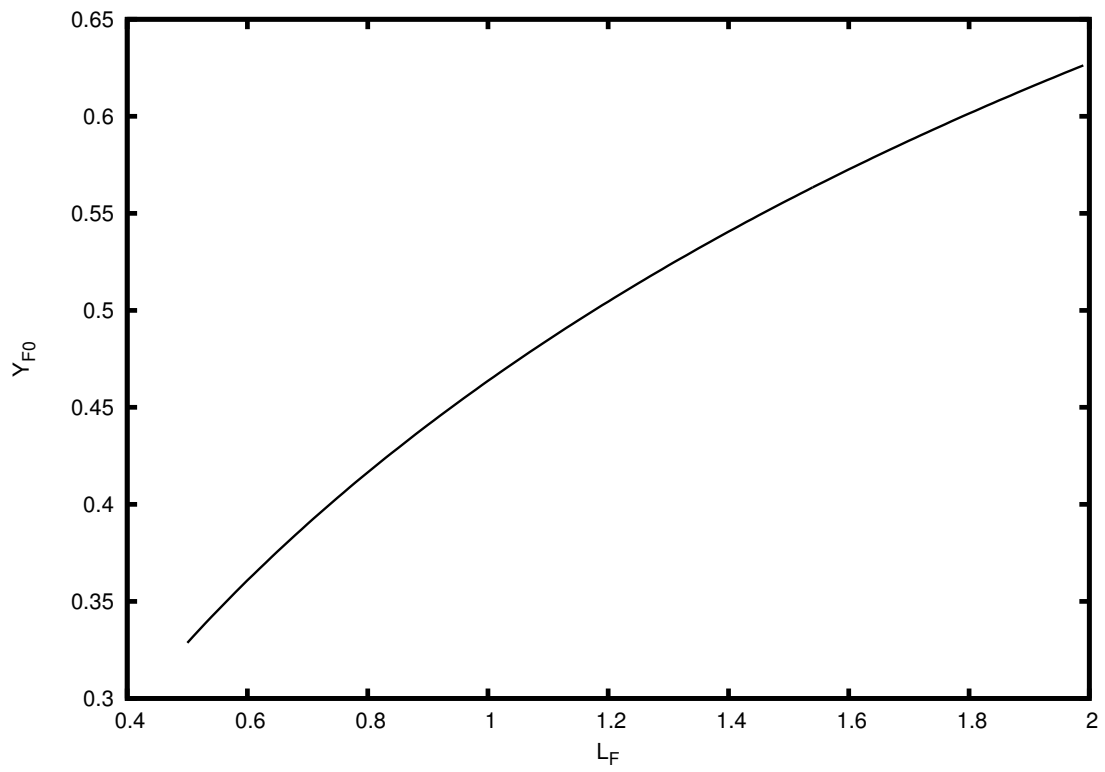


Figure 4.14 - $Y_{F0} \times L_F$, with $\beta^* = 1.08$, $N_g = N_l = 1.0$, $Pr = \varphi = 0.7$, $T_B = 0.333$ and $\Gamma = 50.0$.

5 REACTIVE PROBLEM: DIFFUSION FLAME ESTABLISHED IN A STAGNATION-POINT FLOW CONFIGURATION

In this Chapter we extend the previous Chapters by considering that the liquid is a fuel and the impinging jet is an oxidant. A flame sheet is established in the region where the mass fluxes are at stoichiometric proportion, inside the viscous region around the plane that contains the stagnation-point. The exothermic reaction releases heat, which is conducted to both sides of the flame sheet. In the fuel side, this heat is used to vaporize the liquid fuel, a process that supplies the necessary vapor to sustain the diffusion flame.

For liquid fuels, it has been shown that porous medium burner have some advantages over the conventional spray systems (MUJEEBU *et al.*, 2009). The intense radiation field generated by the heated solid enhances the evaporation of fuel droplets in the confined medium. For situations such that the droplets vaporize and mix with oxidant prior to the combustion zone (MARTYNENKO *et al.*, 1998; KAYAL; CHAKRAVARTY, 2005), essentially a premixed flame is established.

The burning of fuels in non-premixed configurations has not received large attention, which can be measured by the small number of studies found in the literature. However, potentially low emissions of NO_x and CO for the burning of liquid fuels have been addressed (HOWELL *et al.*, 1996). Hence, the study of non-premixed flames in porous media deserves some attention. The evaporation and combustion of ethanol from a porous surface when subjected to a boundary-layer-type flow of air were studied experimentally (BOYARSHINOV *et al.*, 1994). It has been found that the flow velocity has a considerable effect on the flame temperature and the distribution of mass flows over the wall. Also, heat and mass transfer coefficients decreased in combustion. In addition, a similar boundary-layer-type reactive flow was considered in analytical and numerical studies (LIU *et al.*, 2008). The developed analytical model investigates the dynamics of non-premixed flames in a shear layer established between a mainstream flow of fuel-rich combustion products and a porous surface with an angled injection of air. The results were compared with numerical simulations and a qualitative agreement in the surface temperature was observed. Furthermore, comparison of the stability limits predicted by the model with the experimental data was performed and a good qualitative agreement was obtained.

The problem of a free-convective diffusive flame in a porous media was also analyzed by Chao *et al.* (1994). A similarity solution was considered in the infinitely thin flame sheet limit of the reaction of a condensed fuel with an oxidizer flow driven by

the buoyancy force. The results showed that the temperature and species profiles are qualitatively similar to those of the conventional, non-confined, free convection flow. However, the flame temperature is lower as a result of a high value for the effective Lewis number. This elevation on the effective Lewis number causes the flame to move towards the wall. It was also shown that the velocity field may have a maximum at the reaction sheet or two maxima depending upon the temperature dependence of the flow viscosity.

The specific case of stagnation-point diffusion flames stabilized next to a porous wick was analyzed numerically by [Raju and T'ien \(2007\)](#). The porous wick was dipped inside the liquid fuel reservoir and through capillary action the liquid is transported to the surface of the wick and then evaporates and diffuses to the flame. Two regimes beneath the flame, in the porous wick, were characterized: funicular and evaporative regime. In the funicular regime a vapor-liquid (two-phase) region exists close to the surface, with a single-phase liquid region below. In the evaporative regime there is a single vapor phase above the two-phase region. It was shown that the funicular regime was the only stable solution in the porous wick.

In the context of the *in-situ* combustion, [Akkutlu and Yortsos \(2003\)](#) studied the conditions in which the flame propagation in a porous reservoir is stable. They have considered weak heat losses to the ambient and derived expressions for temperature and concentration profiles and the velocity of the combustion front, under both adiabatic and non-adiabatic conditions. A coefficient that expresses the effective heat transfer was obtained in terms of the reservoir thickness and front propagation speed. [Mailybaev et al. \(2011\)](#) analyzed the *in-situ* combustion of oil with pyrolysis and vaporization. By considering injection of air into a porous medium filled with inert gas, medium or high viscosity oil and water, they analyzed the one-dimensional flow generated by a combustion wave. Three pseudo-components were distinguished in the oil: asphaltenes, medium and light oil. At high temperatures, the heavy components were converted to coke, which undergoes combustion. The medium components of the oil crack and release gaseous oil, while the light components and water are vaporized. They considered that the condensed phase was fixed in the reservoir and analyzed the global problem of the propagating combustion front, then they obtained solutions as a series of traveling waves.

The analysis of the *in-situ* combustion phenomenon through the propagating combustion wave neglects diffusion as the analysis is focused on the global aspects of the front. In those cases, the condensed fuel is considered to be at a fixed position inside

the porous matrix. If the local problem is to be considered (close to the condensed phase), then mass diffusion of reactants must be considered in the analysis, as well as the heat conduction.

In the present problem we consider a flame stabilized by a stagnation-point flow against a condensed (liquid) phase, all the system immersed in an inert porous matrix. Then, we analyze how the addition of a porous matrix modifies the overall properties of this problem. Differently from previous Chapters, we do not compare the obtained results with the incompressible model, because the modifications caused by the addition of the porous matrix renders enough physical discussions. Also, we consider a very high Damkohler number, such that we are analyzing a picture close to the infinitely thin flame limit. This is different than the case analyzed in Appendix A, where the finite-rate chemistry is exploited in order to obtain the extinction limits for the confined diffusion flame.

5.1 Physical problem

A schematic of the present problem is given in Fig. 5.1. The exothermic chemical reaction releases heat, which is conducted to both sides of the flame sheet. Gas and solid are thermally coupled such that the heat conducted from the sheet heats the solid, which in turns exchange this heat with the gas and with the liquid. Since mass diffusion towards the flame is the rate-controlling process, the heat removal from the flame through the solid phase lowers the flame temperature. In the context of an one-equation model this result was explained as due to the high value of the effective Lewis number (which takes into account the sum of gas and solid thermal conductivities) (CHAO *et al.*, 1994). In the present case we show that the addition of a resistive force (Darcy term) decreases the local flow velocity, which allows fuel to diffuse to larger distances from the stagnation-point, such that the flame establishes farther from the surface. Then, the vaporization rate decreases, which also decreases the flame temperature. It must be noted that the heat removed from the flame and conducted to the fuel side is recovered, as it is used to vaporize the liquid fuel.

If the interphase heat exchange is high enough, the flame may extinguish (see Appendix A). This result was shown previously (ROY *et al.*, 2014) for premixed flames in the context of smoldering combustion (reactive solid phase). In the present Chapter we do not analyze the extinction limits. The reader is referred to Appendix A, where a comprehensive analysis of the extinction limits of diffusion flames established in inert porous media is performed. In this Chapter we analyze the influence of the porous medium in the overall combustion characteristics of the diffusion flame that

is generated by the stagnation-point flow against the condensed (liquid) phase.

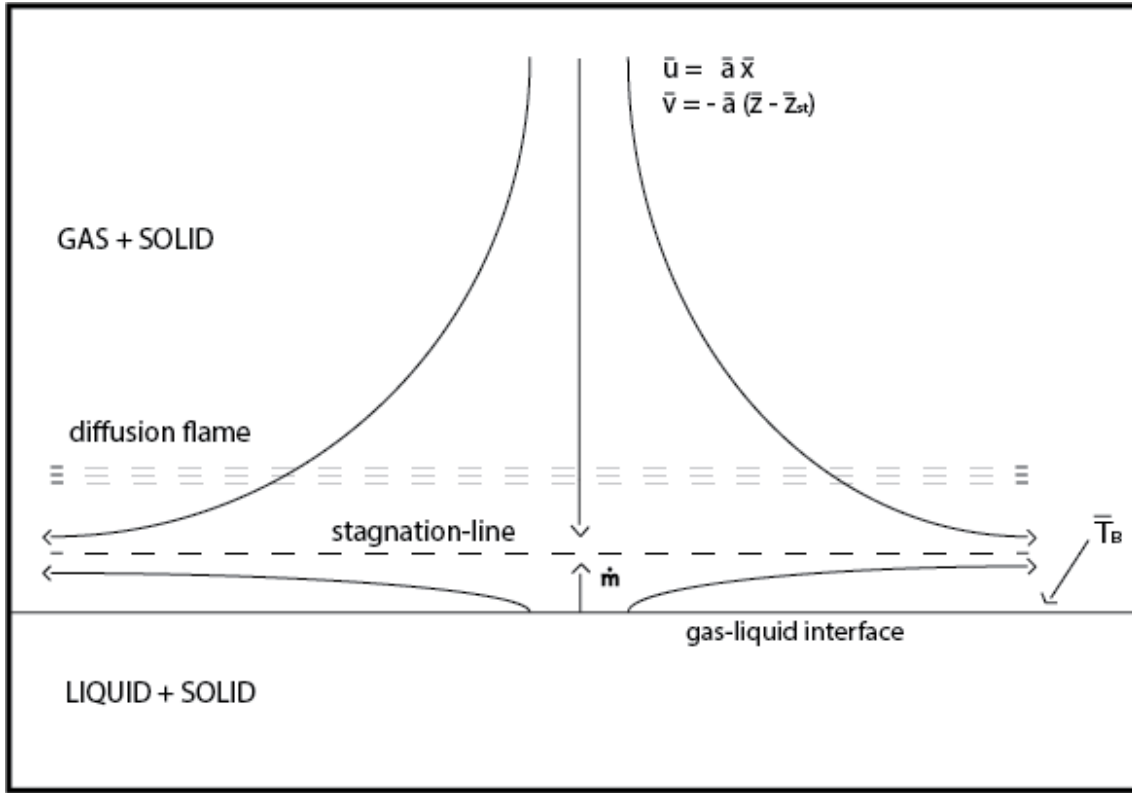


Figure 5.1 - Schematic of the present problem.

The expressions for the solid temperature at the surface T_{s0} , vaporization rate \dot{m} and fuel mass fraction at the surface Y_{F0} are the same as the ones obtained for the pure vaporization case, given by Eqs. 4.16, 4.17 and 4.19. However, in the present case we have the existence of an additional heat source and reactants sink, namely the flame. This new heat source enhances the gas temperature, which by consequence enhances the solid temperature because they are thermally coupled. The increase of the temperature in the gas and solid phases enhances the vaporization rate because of the higher value of the heat fluxes (gas and solid) towards the liquid-solid region (recall that the vaporization rate is given by Eq. 4.17).

Thermal expansion enhances the local flow velocity, which increases the magnitude of the Darcy resistance term (which is proportional to the local flow velocity, as one can see from Eq. 2.42). Hence, at the flame this resistance is high (because of the high local temperature, which by thermal expansion increases the local flow velocity. Note that the Darcy resistance is effectively accounted by βT_g^2). If the

Darcy resistance is high enough, the flow decrease its local velocity at the flame, rather than to increase it as in a non-confined problem. This makes the horizontal flow velocity present a two-peak behavior, similar to the one reported by [Chao et al. \(1994\)](#) in the context of a free-convective flame sheet established in an inert porous media. If the Darcy resistance term is low enough, the flow resembles that of the non-confined problem, with a local maximum horizontal velocity near the flame and caused by gas acceleration due to the heat release at the flame sheet. The Darcy term is proportional to the square of the local gas temperature T_g^2 and to $\beta \sim [(1 - \varphi)/\varphi]^2/(\bar{a}\bar{d}_p^2)$, such that its magnitude can be changed by considering different values of the heat of combustion q (which modifies the flame temperature), strain-rate \bar{a} , medium porosity φ and particle sizes \bar{d}_p (which modify β).

5.2 Mathematical formulation

The full mathematical formulation derived in Chapter 2 is considered now. Then, for the gas-solid region $\eta > 0$ the governing equations are given by

$$Pr \frac{d^3 f}{d\eta^3} + f \frac{d^2 f}{d\eta^2} - \left(\frac{df}{d\eta} \right)^2 - \beta T_g^2 \frac{df}{d\eta} = -T_g (1 + \beta), \quad (5.1)$$

$$Pr \frac{d^2(fT_g)}{d\eta^2} + f \frac{d(fT_g)}{d\eta} - \beta T_g^3 f = (1 - \beta) \frac{dF}{d\eta}, \quad (5.2)$$

$$-f \frac{dY_F}{d\eta} - \frac{\varphi}{L_F} \frac{d^2 Y_F}{d\eta^2} = -\varphi Da Y_F Y_O e^{-T_a/T_g}, \quad (5.3)$$

$$-f \frac{dY_O}{d\eta} - \frac{\varphi}{L_O} \frac{d^2 Y_O}{d\eta^2} = -\varphi \phi Da Y_F Y_O e^{-T_a/T_g}, \quad (5.4)$$

$$-f \frac{dT_g}{d\eta} - \varphi \frac{d^2 T_g}{d\eta^2} = \varphi q Da Y_F Y_O e^{-T_a/T_g} + T_g N_g (T_s - T_g), \quad (5.5)$$

$$-\Gamma(1 - \varphi) \frac{d}{d\eta} \left(\frac{1}{T_g} \frac{dT_s}{d\eta} \right) = -T_g N_g (T_s - T_g). \quad (5.6)$$

For the liquid-solid region $z < 0$, we have

$$-\Gamma(1 - \varphi) \frac{d^2 T_s}{dz^2} = -N_l (T_s - T_B). \quad (5.7)$$

The boundary conditions are the same as the ones used in Chapter 4, but now we must consider the additional boundary conditions for the oxidant mass fraction Y_O .

The boundary conditions for $\eta \rightarrow \infty$ are then given by

$$\frac{df}{d\eta} = 1, \quad T_s = T_g = 1, \quad Y_F = 0, \quad Y_O = 1. \quad (5.8)$$

At the surface $\eta = 0$, we have

$$\frac{df}{d\eta} = 0, \quad T_g = T_B, \quad Y_O = 0. \quad (5.9)$$

The relation between velocities at the interface and the liquid mass conservation gives

$$-f(0) = \dot{m}. \quad (5.10)$$

The solid temperature at the surface $T_s(0) > T_B$ is an unknown to be obtained from the continuity of the solid phase heat flux at the gas-liquid interface, given by

$$\frac{1}{T_B} \frac{dT_s}{d\eta} \Big|_{0+} = \frac{dT_s}{dz} \Big|_{0-}. \quad (5.11)$$

Reservoir condition, $z \rightarrow -\infty$, is given by

$$T_s = T_B. \quad (5.12)$$

At the interface $\eta = z = 0$, fuel mass fraction and energy conservation gives

$$\frac{\varphi}{L_F} \frac{dY_F}{d\eta} \Big|_0 = (1 - Y_{F0})f(0), \quad (5.13)$$

$$\varphi \frac{dT_g}{d\eta} \Big|_{0+} + N_l \int_{-\infty}^{0-} (T_s - T_B) dz = \dot{m} l T_B. \quad (5.14)$$

The solid phase temperature profile in the liquid-solid region is the same as the one given by Eq. 4.15

$$T_s(z) = T_B + \left(\frac{1}{T_B} \frac{dT_s}{d\eta} \Big|_{0+} \sqrt{\frac{\Gamma(1-\varphi)}{N_l}} \right) e^{\sqrt{N_l/(\Gamma(1-\varphi))}z}. \quad (5.15)$$

The vaporization rate and the fuel mass fraction at the surface are also given by Eqs. 4.17 and 4.19

$$\dot{m} = \frac{T_B^{-1}}{l} \left\{ \varphi \frac{dT_g}{d\eta} \Big|_{0+} + \frac{\Gamma(1-\varphi)}{T_B} \frac{dT_s}{d\eta} \Big|_{0+} \right\}, \quad (5.16)$$

$$Y_F(0) = 1 + \frac{\varphi}{L_F \dot{m}} \left. \frac{dY_F}{d\eta} \right|_0. \quad (5.17)$$

As in previous Chapters, we add a fictitious unsteady term into Eqs. 5.1 to 5.7, guess initial profiles that satisfies the boundary conditions and integrate in the pseudo-time until the steady-state is achieved. Then, compare the guessed conditions (namely vaporization rate, solid temperature at the surface and fuel mass fraction at the surface) with the ones calculated through the discretized Eqs. 5.15, 5.16 and 5.17, update if necessary and integrate in the pseudo-time again until the difference between guessed and calculated interface values is less than 10^{-5} . We consider a high Damkohler number and the solutions converge quickly as long as the initial guessed profile for the gas temperature is energetic enough. The constant mesh spacing used was $\Delta\eta = 2.5 \times 10^{-2}$ and this value was enough to capture the overall flame properties (some variations are expected around the values of flame temperature and position because of the high value of the Damkohler number, but the overall trend is correctly predicted). When considering $l = 4.32$, $L_F = L_O = 1.0$, $Pr = \varphi = 0.7$, $q = 100.0$, $\phi = 8.0$, $T_B = 2.5$, $T_a = 10.0$, $Da = 10^7$, $\beta^* = 1.08$, $N_g = N_l = 1.0$ and $\Gamma = 50.0$, we obtained $-f(0) = 0.45855$ with $\Delta\eta = 2.5 \times 10^{-2}$. Dividing the mesh spacing by a factor of two showed no influence up to the fifth decimal, such that $\Delta\eta = 2.5 \times 10^{-2}$ was considered a small enough mesh space. In the reactive term, the reactants mass fractions are calculated implicitly, but the gas temperature explicitly. This avoids the need of linearizing the non-linear Arrhenius term.

5.3 Results

As before, we consider the impinging jet to be air with its properties evaluated at $\bar{T} = 293 \text{ K}$. A mean pore diameter $\bar{d}_p = 5 \text{ mm}$ is considered. Combustion properties are only representative and do not represent any particular fuel. Then, typical profiles for temperatures, mass fractions and velocities are given in Figs. 5.2 and 5.3 with the consideration of $l = 4.32$, $L_F = L_O = 1.0$, $Pr = \varphi = 0.7$, $q = 100.0$, $\phi = 8.0$, $T_B = 2.5$, $T_a = 10.0$, $Da = 10^7$, $\beta^* = 1.08$, $N_g = N_l = 1.0$ and $\Gamma = 50.0$.

Figure 5.2 shows the temperatures and mass fraction profiles (the temperatures profiles for $\eta < 0$ are not shown, but they are similar to the ones obtained in the previous Chapter: constant for the liquid, exponential-like for the solid, as seen from Eq. 5.15 and Fig. 4.2). The consideration of $Da = 10^7$, very high Damkohler number, means that the reactants are almost completely consumed at the flame, which is very thin in this case (a situation very close to the infinitely thin flame limit). At the flame, which for the conditions considered is located approximately at $\eta = 1.9$, as one

can see in Fig. 5.2, the gas has its peak temperature, namely the flame temperature. Since the phases are thermally coupled, the solid has its maximum temperature at the flame as well, but at a lower value T_{sf} . The solid then conducts heat away from the flame. As we move away from the flame, the solid has a higher temperature than the gas because it has a higher thermal conductivity. Since the phases are thermally coupled, the solid heats the incoming reactants, elevating the gas temperature far from the flame sheet.

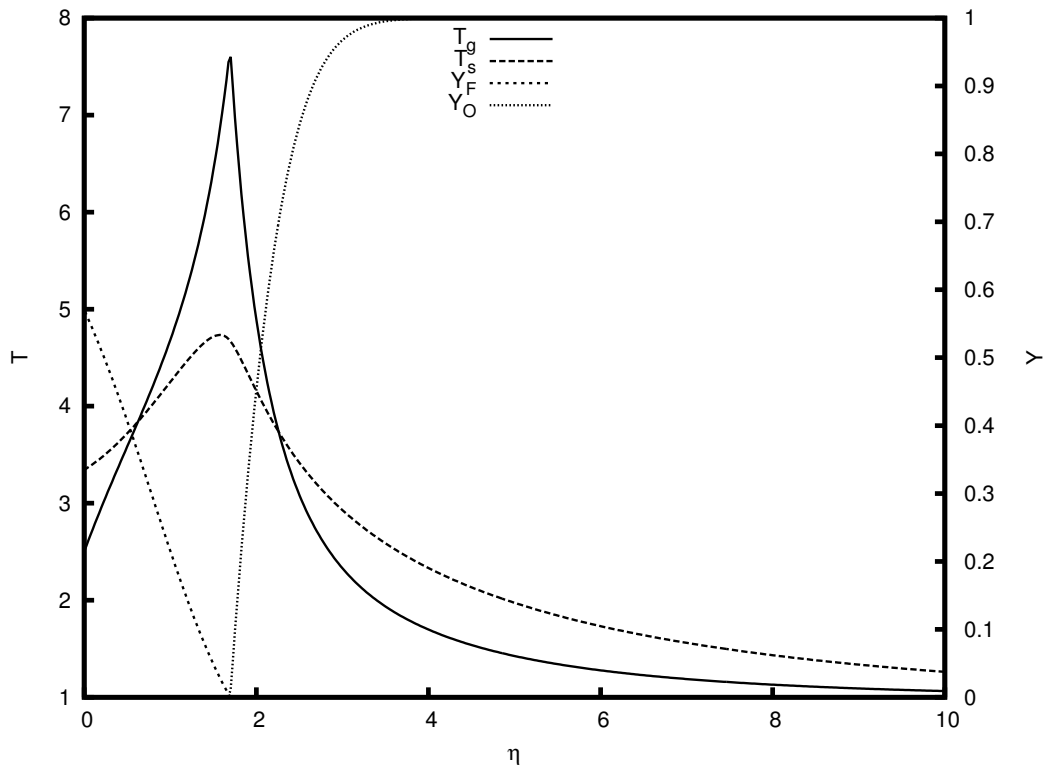


Figure 5.2 - Temperature and mass fraction profiles for $\beta^* = 1.08$, $N_g = N_l = L_F = L_O = 1.0$, $l = 4.32$, $\phi = 8.0$, $Pr = \varphi = 0.7$, $q = 100.0$, $Da = 10^7$, $\Gamma = 50.0$ and $T_B = 2.5$.

The Darcy term represents a resistance force to the flow. For $\varphi = 1.0$ this force is zero, and as we decrease the porosity, the magnitude of this force increases. The Darcy resistance is effectively accounted through the term βT_g^2 that appears in Eq. 5.1. When this resistance is high enough, it decreases the local flow velocity. In this case, fuel vapor can diffuse to larger distances from the stagnation-point to the oxidant side, because the incoming flow has a lower velocity. Then, for lower porosities the flame is established farther from the surface. This decreases the heat

flux to the liquid fuel, such that the vaporization rate decreases.

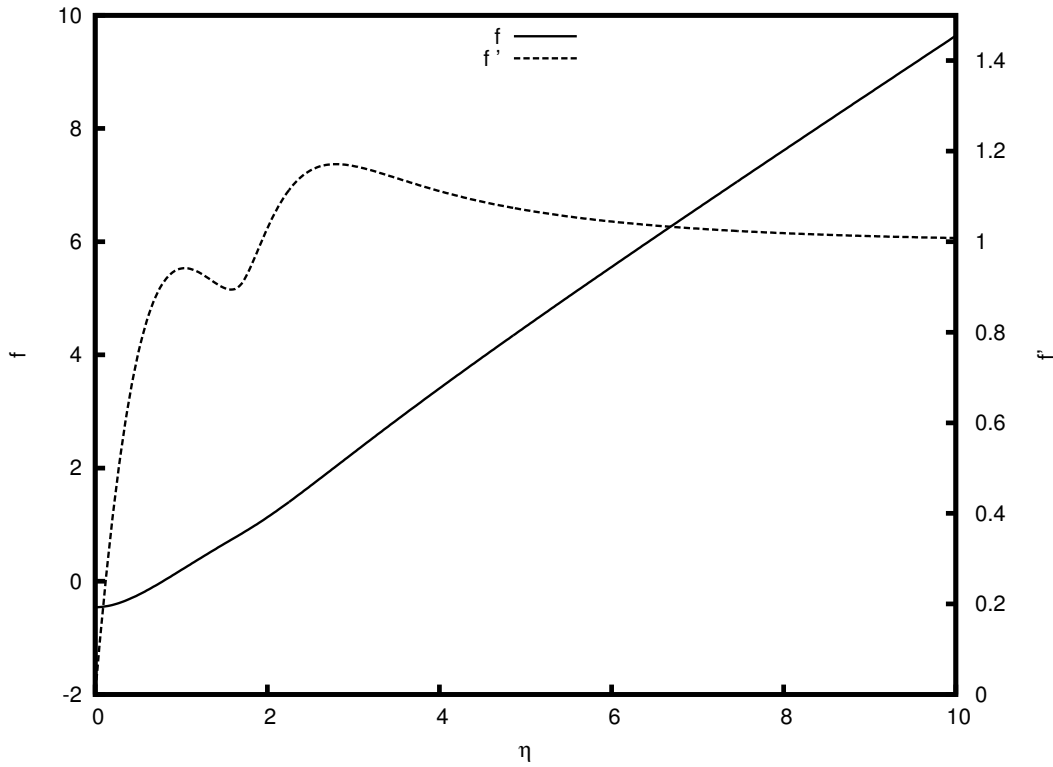


Figure 5.3 - Velocities profiles for $\beta^* = 1.08$, $N_g = N_l = L_F = L_O = 1.0$, $l = 4.32$, $\phi = 8.0$, $Pr = \varphi = 0.7$, $q = 100.0$, $Da = 10^7$, $\Gamma = 50.0$ and $T_B = 2.5$.

Figure 5.4 shows the velocities profiles for $\varphi = \{0.5, 0.7, 1.0\}$, where one can see that a two-peak behavior for the horizontal velocity f' exist when $\varphi = 0.7$ (see also Fig. 5.3). This two-peak is a result of the competition between Darcy resistance, viscosity and convection terms. Thermal expansion enhances velocity, but this also increases the Darcy resistance to the flow (which is proportional to the flow velocity). If the Darcy term is sufficiently high (measured by βT_g^2), the flow resistance imposed by the porous matrix is high and the flow suffer a decrease in its velocity at the flame, rather than an increase, as in non-confined problems ($\varphi = 1.0$ case). The velocity overshoot in the boundary-layer is smoothed by the Darcy resistance as one can see from Fig. 5.4. If the Darcy resistance is high enough, the second-peak is suppressed, as one can see when $\varphi = 0.5$. One can also see from Fig. 5.4 that the vaporization rate (which is measured by $\dot{m} = -f(0)$) is higher for $\varphi = 1.0$. This is because of the higher flame temperature when $\varphi = 1.0$ (for $\varphi = 0.7$ we obtain $T_f \sim 7.6$, while for $\varphi = 1.0$, $T_f \sim 11.02$).

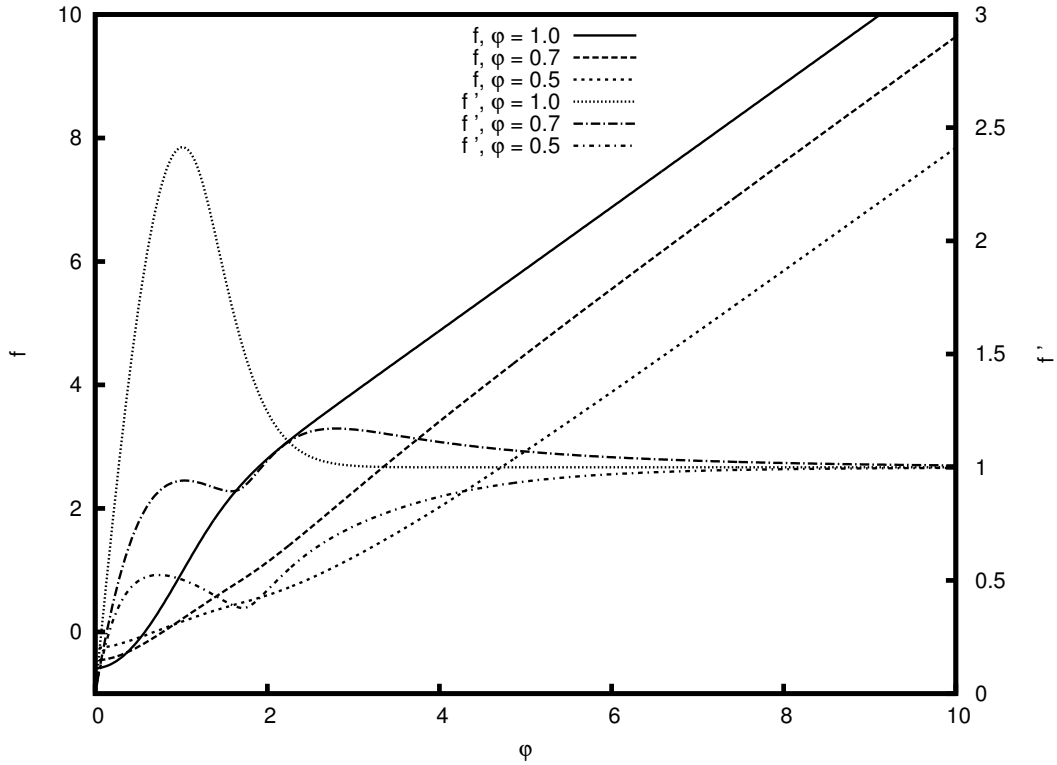


Figure 5.4 - Velocities profiles for $\varphi = \{0.5, 0.7, 1.0\}$ and $\beta^* = 1.08$, $N_g = N_l = L_F = L_O = 1.0$, $l = 4.32$, $\phi = 8.0$, $Pr = 0.7$, $q = 100.0$, $Da = 10^7$, $\Gamma = 50.0$ and $T_B = 2.5$.

The tangential velocity f' has a local minimum at the flame because it is at the flame that βT_g^2 has its maximum value (maximum value of the Darcy resistance), as one can see from Fig. 5.5, where we show f' and βT_g^2 for $\varphi = 0.7$. Then, when β is sufficiently high, the flame acts almost as an wall to the flow, imposing a high resistive force.

The magnitude of the Darcy resistance force is given by βT_g^2 , with a maximum at the flame because T_g is maximum at the flame. Recalling that $\beta = \beta^*[(1 - \varphi)/\varphi]^2$, it is easy to see that for lower porosities this resistance is higher. In Fig. 5.6 we show the maximum value of the Darcy resistance βT_f^2 with respect to the porosity φ , and in Fig. 5.7 we show the positions of the flame and of the stagnation-point with respect to the porosity φ . One can see that for decreasing porosities the maximum Darcy resistance βT_f^2 increases, which favors mass diffusion of the fuel vapor farther from the stagnation-point, which makes the flame to be established farther from the surface.

As argued previously, the presence of the porous medium decreases the flame temper-

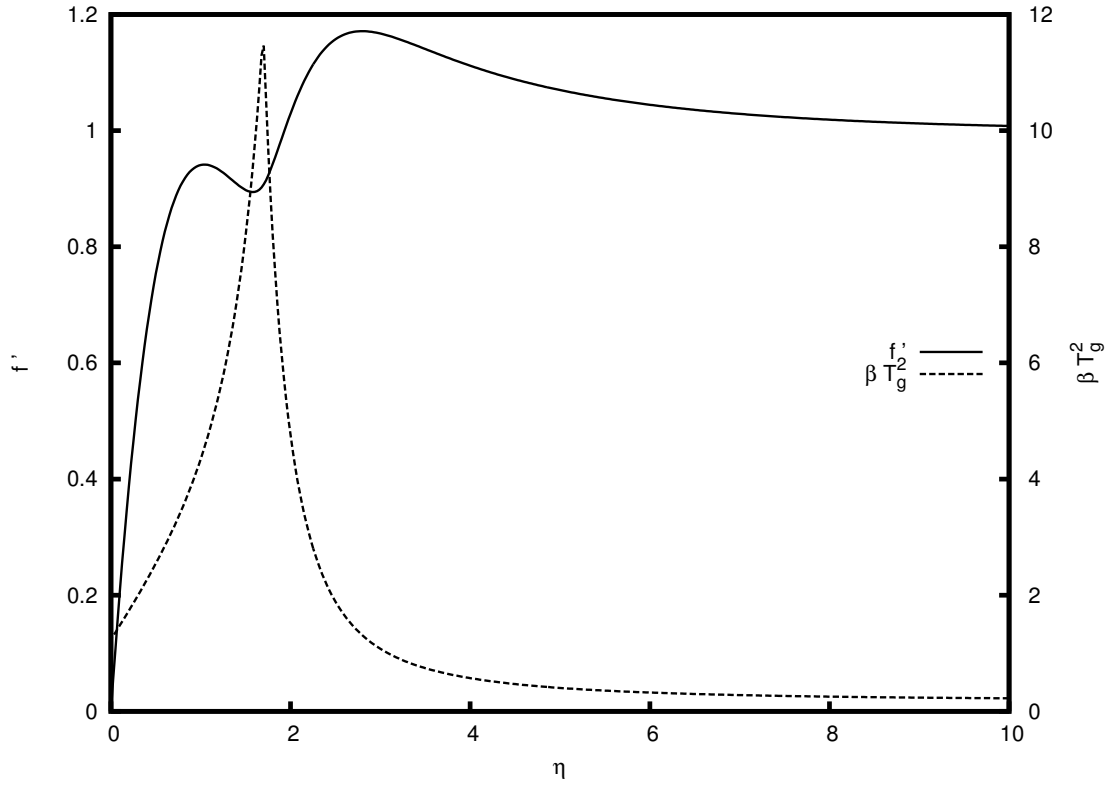


Figure 5.5 - Velocity profile and Darcy resistance for $\varphi = 0.7$, $\beta^* = 1.08$, $N_g = N_l = L_F = L_O = 1.0$, $l = 4.32$, $\phi = 8.0$, $Pr = 0.7$, $q = 100.0$, $Da = 10^7$, $\Gamma = 50.0$ and $T_B = 2.5$.

ature because the solid phase removes heat from the flame and distributes it to both sides of the sheet. Since for lower porosities the heat flux through the solid phase is enhanced, it is expected that if the porosity is low enough the flame will extinguish (see Appendix A). In the present case, however, since we consider $Da = 10^7$, very high Damkohler number, this does not occur. In Fig. 5.8 we compare temperature and mass fraction profiles for $\varphi = 0.5$ and $\varphi = 1.0$. The flame temperature decreases from $T_f = 11.02$ to $T_f = 5.97$, approximately, for the cases $\varphi = 1.0$ and $\varphi = 0.5$, respectively, and its position changes from $\eta_f \sim 1.6$ to $\eta_f \sim 1.9$.

The influence of the medium porosity φ on flame temperature T_f and vaporization rate \dot{m} is shown in Fig. 5.9. For low porosities the heat removed from the flame by the solid phase is high, which lowers the flame temperature and the vaporization rate (which also lowers because the flame is located farther from the surface). As the porosity increases, heat loss diminishes and the flame approaches the surface, such that flame temperature and vaporization rate increases. Starting from $\varphi = 1.0$ (non-confined problem) and decreasing φ , the heat loss to the oxidant side is small, and

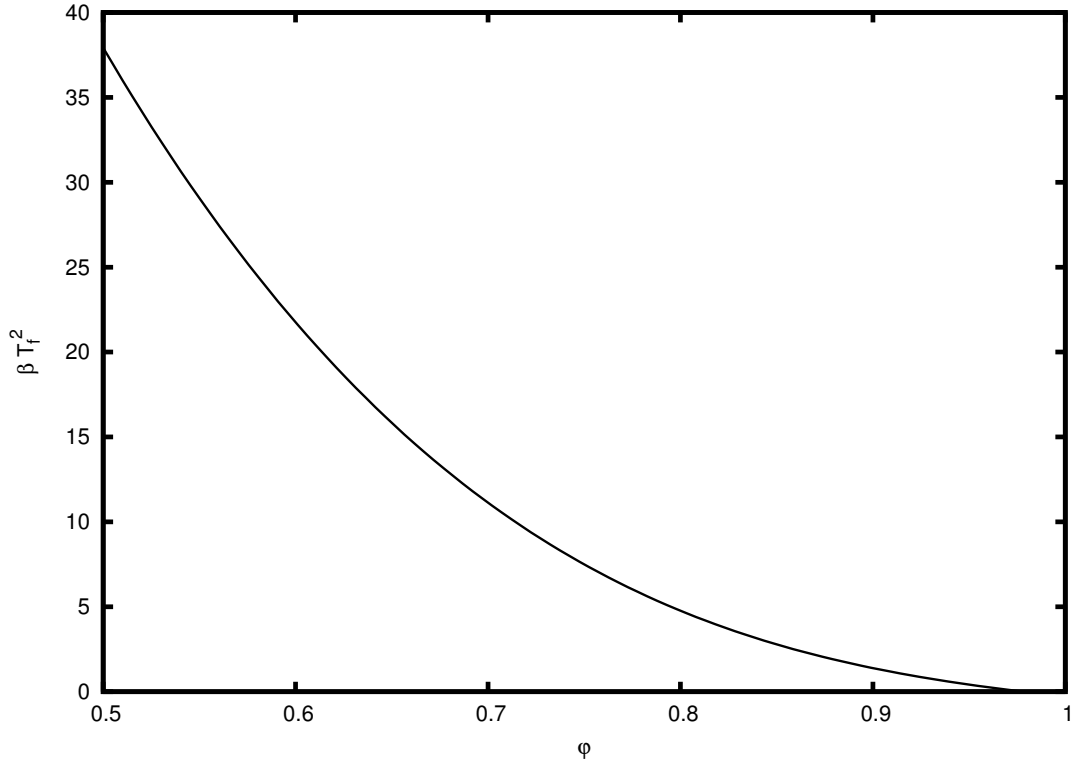


Figure 5.6 - Darcy resistance \times porosity, for $\beta^* = 1.08$, $N_g = N_l = L_F = L_O = 1.0$, $l = 4.32$, $\phi = 8.0$, $Pr = 0.7$, $q = 100.0$, $Da = 10^7$, $\Gamma = 50.0$ and $T_B = 2.5$.

in this case, the heat conduction through the solid phase to the fuel side enhances the vaporization rate. These properties makes the dependence of the vaporization rate with the porosity ϕ to present a maximum at approximately $\phi = 0.925$ for the considered conditions. Note that for the considered conditions, when $\phi < 0.8$, the vaporization rate is smaller than the vaporization rate obtained for the non-confined problem ($\phi = 1.0$). Hence, the porous medium enhances the vaporization rate for $\phi > 0.8$.

In a previous work we analyzed this problem with the assumption of very low permeability medium and under the scope of a constant-density model (KOKUBUN; FACHINI, 2013). In that work, it was shown that the flame temperature and vaporization rate decreased with increasing porosities, an opposite result to what it is obtained in the present work (see Fig. 5.9). However, this happens because in that previous work we considered a very low permeability (low porosity) and then extrapolated the results for higher porosities. In the present notation, the consideration of a very low permeability in that work was accounted through $K = \Gamma^{-1} \ll 1$, or $\beta = \Gamma \gg 1$. Recalling that the model utilized for the permeability 2.31 determines

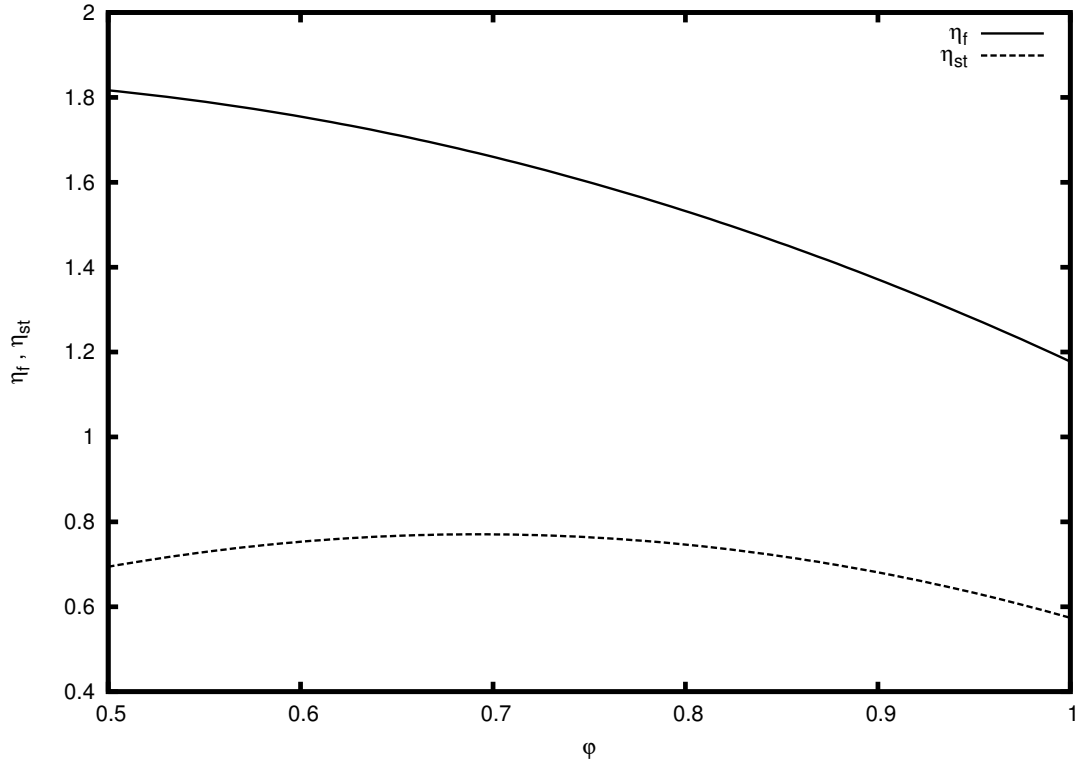


Figure 5.7 - Flame position and stagnation-point position $\times \phi$ for $\beta^* = 1.08$, $N_g = N_l = L_F = L_O = 1.0$, $l = 4.32$, $\phi = 8.0$, $Pr = 0.7$, $q = 100.0$, $Da = 10^7$, $\Gamma = 50.0$ and $T_B = 2.5$.

β through $\beta = \beta^*[(1 - \phi)/\phi]^2$, and that $\beta^* = O(1)$, then, it can be shown that the previous model is valid up to $\phi \sim 1/(\sqrt{\Gamma} + 1)$. By considering $\Gamma = 50.0$, we see that the previous model was valid for porosities lower than $\phi \sim 0.12$, i.e., very low porosities. If we analyze the gas and solid heat fluxes at the surface, Q_g and Q_s in Eq. 4.20 and shown in Fig. 5.10, we can see that when the porosity is high the gas contribution to the vaporization rate is higher than the solid contribution. As we decrease the porosity, the solid contribution becomes higher than the gas contribution, even though both are decaying due to the lowering on the flame temperature. If the flame was not allowed to extinguish, in the limit of very low porosity the solid would be the responsible for the leading-order contribution to the vaporization rate. Then, in this scenario, a decrease on the porosity enhance the vaporization rate and consequently the flame temperature. Since the trend observed in the previous work (KOKUBUN; FACHINI, 2013) and the one observed now are opposed, a theoretical turning point is expected to occur at some intermediary porosity. This trend is given schematically in Fig. 5.11.

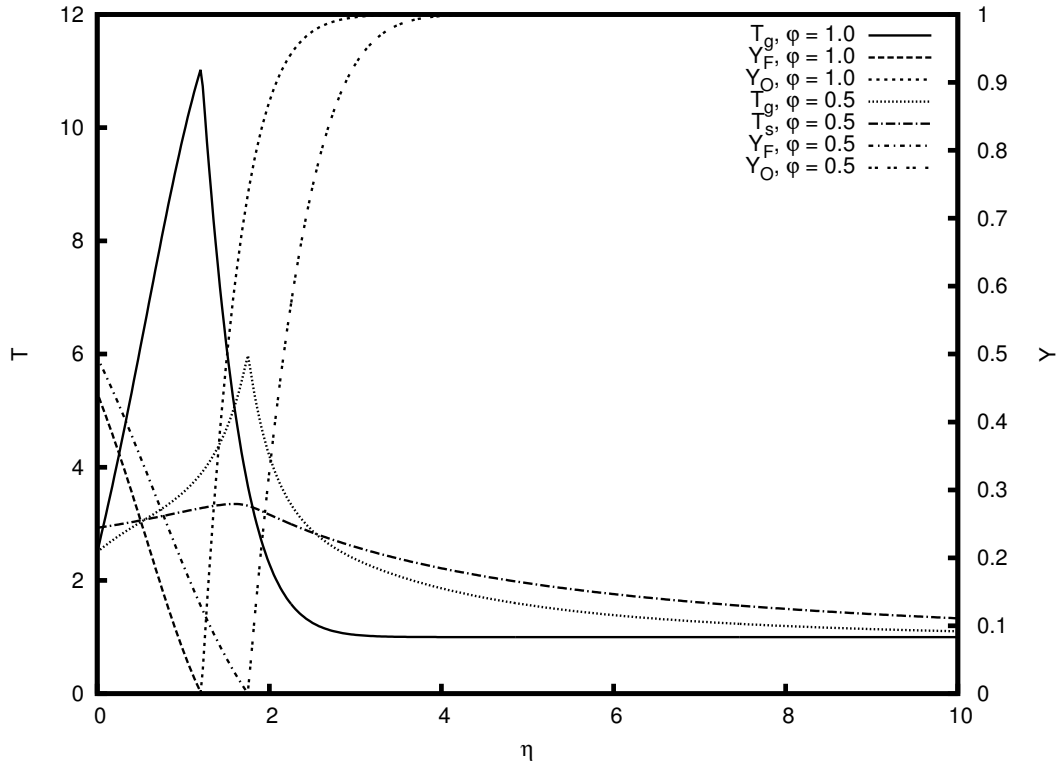


Figure 5.8 - Temperature and mass fraction profiles for $\varphi = \{0.5, 1.0\}$ and $\beta^* = 1.08$, $N_g = N_l = L_F = L_O = 1.0$, $l = 4.32$, $\phi = 8.0$, $Pr = 0.7$, $q = 100.0$, $Da = 10^7$, $\Gamma = 50.0$ and $T_B = 2.5$.

Efficient porous burners have a high porosity whilst having small pores. This is mainly because: (1) if the porosity is low, the hydraulic loss are high and (2) if the pores are large, heat loss by radiation through the solid phase is high. In the present work we do not consider radiation (and also do not calculate the hydraulic losses associated with the lowering in the porosity, i.e., increasing in β), but our results show that we have an optimum porosity to which the vaporization rate is maximum. In this case, the maximum vaporization rate is associated with a balance between the heat loss to the oxidant side and the enhancement of the heat flux towards the liquid fuel, that is caused by the presence of the solid matrix (see Eq. 5.16). It is worth to note that even though the vaporization rate has a maximum, the flame temperature does not have such maximum (the highest flame temperature is achieved in the non-confined case, $\varphi = 1.0$). This is because the gas and solid are coupled, even when the porosity is high, such that the conditions for the establishment of the diffusion flame are achieved farther from the surface, which makes the flame temperature to be lower.

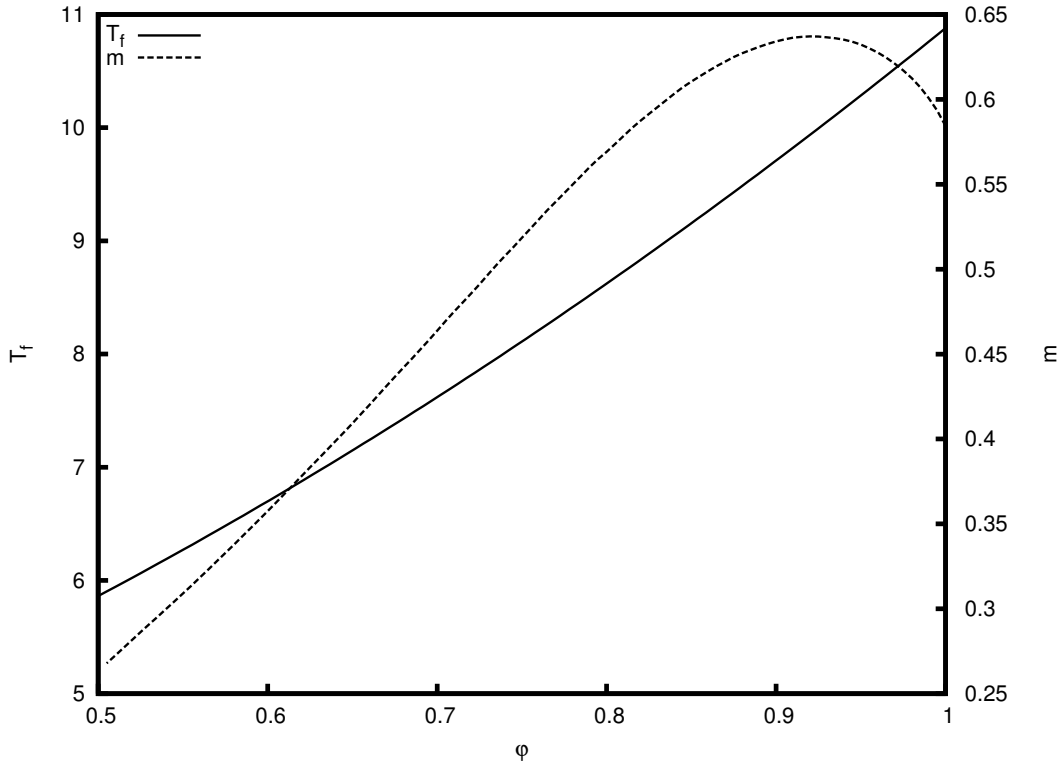


Figure 5.9 - $\{T_f, \dot{m}\} \times \phi$ for $\beta^* = 1.08$, $N_g = N_l = L_F = L_O = 1.0$, $l = 4.32$, $\phi = 8.0$, $Pr = 0.7$, $q = 100.0$, $Da = 10^7$, $\Gamma = 50.0$ and $T_B = 2.5$.

5.4 Conclusions

In this Chapter we extended the previous results by considering an impinging jet of oxidant against a pool of liquid fuel, with all the system immersed in an inert porous matrix. A diffusion flame is established approximately where the reactants mass fluxes are at stoichiometric proportion. The solid matrix removes heat from the flame and transports it to both sides of the flame. At the fuel side, the heat is recovered because it is completely used to the liquid fuel phase change (the liquid fuel is considered to be at its boiling temperature), while at the oxidant side, part of the heat is lost (in the sense that it is not recovered by the flame sheet), such that the flame has a lower temperature when compared to the non-confined case.

Thermal expansion induces an increase on the local flow velocity, but since the Darcy resistance term is proportional to the flow velocity, thermal expansion also induces an increase on the magnitude of the Darcy resistance term. This dynamics leads to a complex flow behavior if compared to a non-confined case. If the porosity is low enough (for the considered conditions, $\phi = 0.7$ was considered low enough), the flow

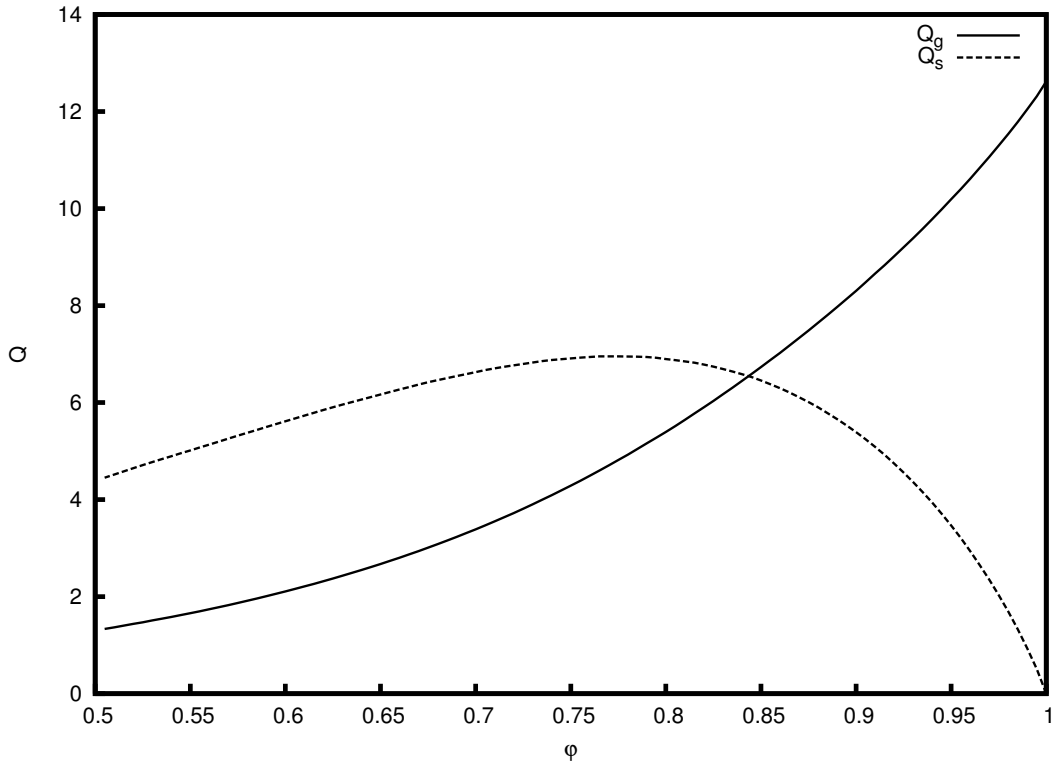


Figure 5.10 - $\{Q_g, Q_s\} \times \varphi$ for $\beta^* = 1.08$, $N_g = N_l = L_F = L_O = 1.0$, $l = 4.32$, $\phi = 8.0$, $Pr = 0.7$, $q = 100.0$, $Da = 10^7$, $\Gamma = 50.0$ and $T_B = 2.5$.

lower its velocity at the flame sheet (instead of increasing it as in a non-confined problem), and a two-peak behavior is observed for the horizontal (tangential) flow velocity. However, if the Darcy resistance is increased further, the velocity overshoot is smoothed, and may even be eliminated, as one can see in Fig. 5.4. Also, since the Darcy resistance is higher for lower porosities, such that the velocity is lower, the fuel is able to diffuse to larger regions when the porosity is low. This makes the flame to be established farther from the surface. This lowers the heat flux towards the liquid phase, such that the vaporization rate and the flame temperature are lower.

The vaporization rate \dot{m} variation with the porosity φ presents a maximum close to $\varphi = 0.925$ (for the set of parameters considered). This is explained because when the porosity is very high, the heat flux to the oxidant side is practically restrict to that by the gas phase and in this situation the heat flux to the fuel side (and to the liquid fuel) is large, consequently the vaporization rate is enhanced. However, if the porosity is lower than $\varphi \sim 0.925$, then the heat flux to the oxidant side surpass the heat conduction to the fuel side by the solid phase, such that the vaporization rate starts to decrease.

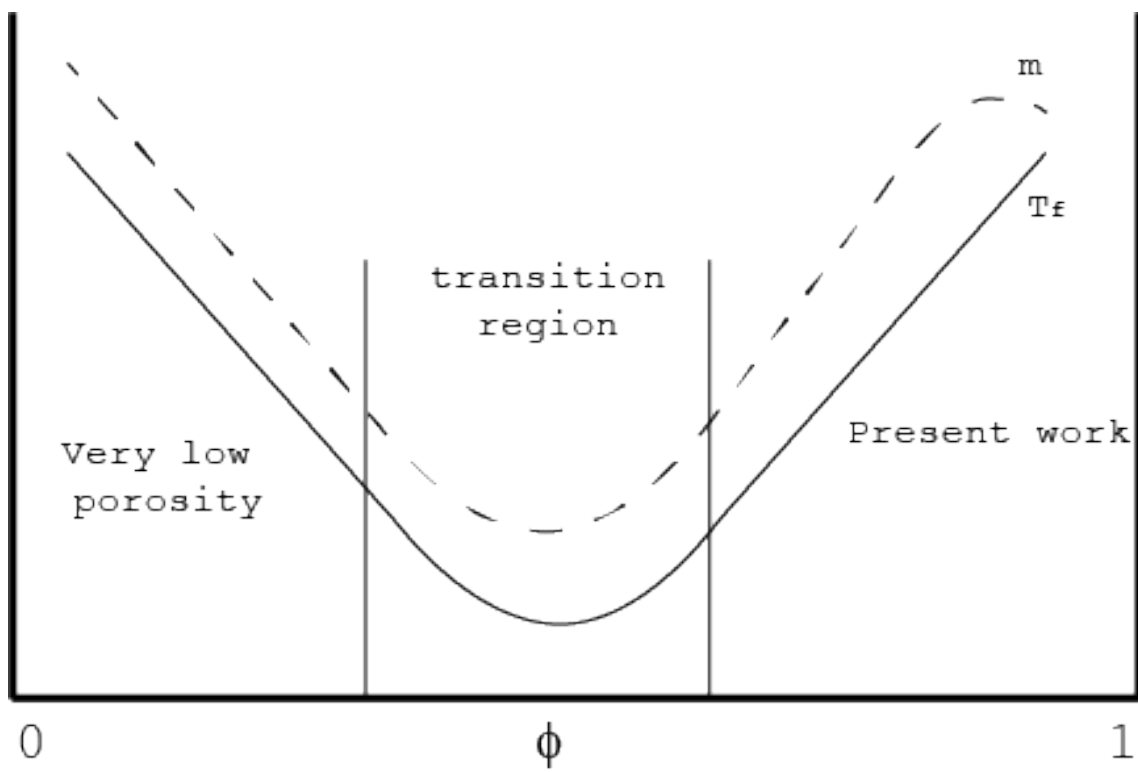


Figure 5.11 - Expected variations of flame temperature and vaporization rate with respect to the porosity ϕ .

6 CONCLUSIONS

In this work we analyzed a diffusion flame established inside an inert porous medium. An impinging jet of oxidant against a liquid fuel pool, with all the system (gas and liquid phases) immersed inside the porous matrix, was the considered geometry. A semi-heuristic formulation was utilized, in which the Darcy term was added to the usual compressible Navier-Stokes equations for the momentum components. The thermal interaction between phases was accounted through an interphase heat exchange term, that couples gas and solid; and liquid and solid energy equations. In order to obtain a better understanding of the physical features that occur in such system, we divided the problem in three parts.

In the first, we analyze a frozen impinging flow of gas against a hot impermeable wall (the gas is confined in the porous matrix): heat transfer problem. The results obtained, which are relevant for the study of porous heat exchangers, shows the existence of velocity overshoot in the viscous boundary-layer, like in a non-confined problem. However, if the porosity is low enough, the Darcy resistance to the flow smooth this overshoot. The presence of the solid phase enhances heat transport to large regions because the solid has a higher thermal conductivity compared to gas. This increases the length of the thermal boundary-layer (a growth that is proportional to $\sqrt{\Gamma(1-\varphi)}$, i.e., the square root of the product between the solid-to-gas thermal conductivities ratio Γ and the solid volume $(1-\varphi)$). Comparing the obtained results with results obtained for an incompressible model (constant density), it is shown that thermal expansion usually enhances the wall shear. However, if the wall temperature is high enough, the Darcy resistance term may be high (as it is measured by βT_g^2), which may lowers the local flow velocity, leading to a decrease on the wall shear for high values of the wall temperature, a behavior not captured by incompressible models (which measures the Darcy resistance only through β). Depending on the value of β (inverse of the Darcy number, which is based on the viscous length-scale), the pressure field may present a maximum above the stagnation-point due to the high pore-level dissipation. The existence of a singular point for $\beta = 1$ might point to the need of using a different model for the pressure when the permeability is low ($\beta > 1$).

In the second part we replace the impermeable wall by a liquid pool and consider that the incoming jet is hot, such that a vaporization problem was analyzed. In this case, the heat and mass transfer properties in the confined problem were analyzed by considering a frozen flow (chemical term set to zero). Velocity overshoot was

not observed because this demands the existence of a temperature in the viscous boundary-layer higher than the free-stream temperature. The addition of a porous matrix enhances heat transport towards the liquid, which increases the vaporization rate. The consideration of thermal expansion leads to higher values of the vaporization rate, solid temperature at the surface and vapor mass fraction at the surface. Also, since the flow velocity is enhanced, vapor transport from the surface to above the stagnation-point is more difficult. The liquid vaporization rate increases with increasing values of the liquid-solid heat exchange coefficient N_l . In the asymptotic limit of $N_l \gg 1$ the vaporization rate growth is proportional to $\sqrt{N_l}$. An increase on the solid-to-gas thermal conductivities ration Γ also increases the vaporization rate because it increases heat transport through the solid phase. For increasing values of the gas-solid heat exchange coefficient N_g the vaporization rate increases. From Fig. 4.13 one can see that for small N_g the solid has a greater influence on the vaporization rate than the gas. As N_g increases, the lowering on the temperatures difference leads to the phases contributing more equally to the vaporization rate. Since the solid has a much larger thermal conductivity than the solid, when N_g is small the growth of the vaporization rate is much more prominent than the growth when N_g is greater, as one can see from Fig. 4.12.

Finally, in the third part we consider the incoming jet to be oxidant and the liquid to be fuel. The chemical reaction was then taken into account and a confined diffusion flame was analyzed. The solid matrix removes heat from the flame and conducts it to oxidant and fuel sides. For the fuel side, this heat is recovered because it is used to vaporize the liquid fuel, which is at its boiling temperature. For the oxidant side, part of this heat is lost (in the sense that it is not recovered at the flame sheet). Then, the porous matrix lowers the temperature of the confined diffusion flame. The increase of the Darcy resistance term when the porosity is low makes the flow velocity decrease at the flame, which leads the flow to present a two-peak behavior, with a local minimum at the flame. The lower local flow velocity due to the high Darcy resistance also allows the fuel to diffuse to larger regions beyond the stagnation-point, which makes the flame to establish farther from the surface. Even though the flame temperature only decreases with decreasing porosities, the vaporization rate presents a maximum with the porosity. This occur because when the porosity is high, the heat transport to the fuel side is enhanced by the solid matrix, such that the vaporization rate increases accordingly. However, if the porosity is lowered enough, the heat loss to the oxidant side becomes more relevant, such that the heat flux towards the liquid fuel diminishes, lowering the vaporization rate. The low temperatures achieved for the confined diffusion flames makes this system to have

potentially lower emissions of pollutants.

In Appendix A we perform an asymptotic analysis of the extinction limits of a diffusion flame established in a porous chamber, in order to clarify the influence of the gas-solid heat exchange on the extinction behavior of such confined flame. It was shown that low porosities may extinguish this flame because of the increase of the heat exchange coefficient N . The reactant that is more consumed at extinction depends on the injection velocity \bar{V} (which modifies the interphase heat exchange coefficient). When the extinction diagram is shown with respect to the dimensionless injection velocity, we can see that two extinction points exist: one for low injection velocities and the other for high injection velocities. The extinction point associated with the high injection velocity is the usual kinetic extinction point, which is associated with a low residence time of the reactants in the reaction region. The extinction point associated with the low injection velocity is associated with a high value of the heat loss (heat exchange between gas and solid phases). This low-velocity extinction point was already observed previously in the literature (MATALON et al., 1979; MATALON; LUDFORD, 1979; TIEN, 1986; SIBULKIN, 1988; CHAO et al., 1990; CHAO; LAW, 1993; WANG et al., 2007), but differently from those cases, the Damkohler number for the low-velocity extinction point is low, instead of high. This occurs because the injection velocity modifies the Burke-Schumann solutions in this confined problem, as it changes the interphase heat exchange coefficient N , which modifies the stoichiometric flame temperature T_f^s (temperature associated with complete combustion). If the heat exchange is high enough, namely $N = O(\epsilon^{-1})$ (where $\epsilon \ll 1$ is the inverse of the dimensionless activation energy), then the interphase heat exchange becomes important in the reaction region. In this case, the leakage of reactants through the flame sheet becomes of order of unity and the flame will fall into Liñan's premixed flame regime (LIÑAN, 1974), such that a different asymptotic treatment is required.

6.1 Future works

Even though we attempted to cover a wide range of physical situations when we divided the problem into three distinct, but closely related, parts, some simplifications that were considered when constructing the mathematical model deserve some attention.

The consideration of constant interphase heat exchange coefficients N_g and N_l is not realistic. These coefficients have no closed-form expression, but instead their expressions rely on empirical correlations (in Appendix A we utilize one of such correlations). For increasing flow velocities, these coefficients decrease, because the

higher contact time between fluid and solid decreases the heat exchange between phases. This is expected to have a significant influence in the gas-solid region, which have a complex flow profile. Also, if the pores are large, the Rosseland approximation fails and one must take into consideration heat transfer by radiation through the solid phase. This will have a significant effect on the vaporization rate and on the flame temperature. In the realistic case where a three-phase region below the interface exists, the formation of bubbles at the pore walls decrease the local heat transfer between solid and liquid, which will decrease the vaporization rate. Then, the consideration of a constant-temperature, two-phase zone in which the liquid fuel undergoes phase change overpredicts the vaporization rate. If the heat transfer is intense, there is a dramatic reduction in the vaporization rate (ZHAO; LIAO, 2000).

For diffusion flames, the rate-controlling process is the mass diffusion of reactants towards the flame sheet. Then, the pre-heating of the reactants caused by the solid phase should be significant only if the mass diffusion of reactants towards the flame increases. Since we consider $\rho^2 D_i = 1$, this effect is minimum (if not completely negligible). If we consider the more realistic case of $\rho^2 D_i \sim T_g^a$ (where $a > 0$), it is expected that the pre-heating of the reactants becomes relevant, as it will influence directly the mass diffusion of reactants towards the flame sheet. In this case, results for the flame temperature will be higher than the ones obtained in the present work.

Nevertheless, the proposed model can shed some light into the heat and mass transfer processes that occur in confined media. The work presented here form the basis for future researches that can be performed. We anticipate some of the possible extensions:

- Consideration of proper models for N_g and N_l , i.e., the interphase heat exchange coefficients;
- Consideration of radiation through the solid-phase;
- More realistic temperature-dependences for the gas viscosity and for the mass-diffusion coefficients;
- Proper modelling of the three-phase region right below the gas-liquid surface (using the model developed by Raju and T'ien (2007) as basis, for instance);
- Ignition conditions for the problem analyzed in Chapter 4;
- Extinction limits for the problem analyzed in Chapter 5.

REFERENCES

- AKKUTLU, I. Y.; YORTSOS, Y. C. The dynamics of in-situ combustion fronts in porous media. **Combust. Flame**, v. 134, p. 229–247, 2003. 1, 68
- ALI, S. M. F. Heavy oil - evermore mobile. **J. Petroleum Sci. Engng**, v. 37, p. 5–9, 2003. 1
- ATTIA, H. On the effectiveness of porosity on stagnation point flow with heat transfer over a permeable surface. **J. Porous Media**, v. 10, p. 625–631, 2007. 29
- BARRA, A.; ELLZEY, J. Heat recirculation and heat transfer in porous burners. **Combust. Flame**, v. 137, p. 230–241, 2004. 1
- BOYARSHINOV, B. F.; VOLCHKOV, E. P.; TEREKHOV, V. I. Heat and mass transfer in a boundary layer with the evaporation and combustion of ethanol. **Combust. Expl. Shock Waves**, v. 30, p. 1–8, 1994. 67
- BRANCH, M. C. In-situ combustion retorting of oil shale. **Prog. En. Combust. Sci.**, v. 5, p. 193–206, 1979. 1
- CASTANIER, L. M.; BRIGHAM, W. E. Upgrading of crude oil via in situ combustion. **J. Petroleum Sci. Engng**, v. 39, p. 125–136, 2003. 1
- CHAO, B. H.; CHENG, P.; LE, T. Free-convective diffusion flame sheet in porous media. **Combust. Sci. Tech**, v. 99, p. 37–41, 1994. 3, 5, 6, 16, 67, 69, 71
- CHAO, B. H.; LAW, C. K. Asymptotic theory of flame extinction with surface radiation. **Combust. Flame**, v. 92, p. 1–24, 1993. 9, 87, 119
- CHAO, B. H.; LAW, C. K.; TIEN, J. S. Structure and extinction of diffusion flames with flame radiation. **Symposium (International) on Combustion**, v. 23, p. 523–531, 1990. 87, 119
- CHEATHAM, S.; MATALON, M. A general asymptotic theory of diffusion flames with application to cellular instability. **J. Fluid Mech.**, v. 414, p. 105–144, 2000. 8, 100, 102, 112, 113, 120
- COHEN, C. B.; RESHOTKO, E. Similar solutions for the compressible laminar boundary layer with heat transfer and pressure gradient. **Naca Technical Report**, n. 3325, 1955. 34

DAURELLE, J. V.; TOPIN, F.; OCCELLI, R. Modeling of coupled heat and mass transfers with phase change in a porous medium: application to superheated steam drying. **Numer. Heat Transf. Part A**, v. 33, p. 39–63, 1998. 47

DUVAL, F.; FICHOT, F.; QUINTARD, M. A local thermal non-equilibrium model for two-phase flows with phase-change in porous media. **Int. J. Heat Mass Transf.**, v. 47, p. 613–639, 2004. 15

FU, X.; VISKANTA, R.; GORE, J. P. Measurement and correlation of volumetric heat transfer coefficients of cellular ceramics. **Exp. Thermal Fluid Sci.**, v. 17, p. 285–293, 1998. 104

HOWARTH, L. On the solution of the laminar Boundary-layer equations. **Proc. Roy. London A**, v. 164, p. 547–579, 1938. 26, 32

HOWELL, J. R.; HALL, M. J.; ELLZEY, J. L. Combustion of hydrocarbon fuels within porous inert media. **Prog. En. Combust. Sci.**, v. 22, p. 121–145, 1996. 1, 67

IL'ICHEV, A. T.; TSYPKIN, G. G.; PRITCHARD, D.; RICHARDSON, C. N. Instability of the salinity profile during the evaporation of saline groundwater. **J. Fluid Mech.**, v. 614, p. 87–104, 2008. 48

JABBOUR, C.; M, Q.; BERTIN, H.; ROBIN, M. Oil recovery by steam injection: three-phase flow effects. **J. Petroleum Sci. Engng**, v. 16, p. 109–130, 1996. 48

JENG, T. M.; TZENG, S. C. Experimental study of forced convection in metallic porous block subject to a confined slot jet. **Int. J. Heat Mass Transf.**, v. 46, p. 1242–1250, 2007. 29

JUGJAI, S.; PHOTHIYA, C. Liquid fuels-fired porous combustor-heater. **Fuel**, v. 86, p. 1062–1068, 2007. 16

JUGJAI, S.; PONGSAI, C. Liquid fuels-fired porous burner. **Combust. Sci. Tech**, v. 179, p. 1823–1840, 2007. 3, 4, 16

JUGJAI, S.; POLMART, N. Enhancement of evaporation and combustion of liquid fuels through porous media. **Exp. Thermal Fluid Sci.**, v. 27, p. 901–909, 2003. 3, 4

JUGJAI, S.; WONGPANIT, N.; LAOKETKAN, T.; NOKKAEW, S. The combustion of liquid fuels using a porous medium. **Exp. Thermal Fluid Sci.**, v. 26, p. 15–23, 2002. 3, 4

- KAKUTKINA, N. A. Some stability aspects of gas combustion in porous media. **Combust. Expl. Shock Waves**, v. 41, p. 395–404, 2006. 2
- KAMAL, M. M.; MOHAMAD, A. A. Development of a cylindrical porous-medium burner. **J. Porous Media**, v. 9, p. 469–481, 2006. 4
- KAVIANY, M. **Principles of heat transfer in porous media**. 2. ed. [S.l.]: Springer, 1995. 13, 14, 15, 19
- KAYAL, T. K.; CHAKRAVARTY, M. Combustion of liquid fuel inside inert porous media: an analytical approach. **Int. J. Heat Mass Transf.**, v. 48, p. 331–339, 2005. 3, 67
- KOKUBUN, M. A. E.; FACHINI, F. F. An analytical approach for a Hiemenz flow in a porous medium with heat exchange. **Int. J. Heat Mass Transf.**, v. 54, p. 3613–3621, 2011. 8, 30, 36, 44
- _____. Asymptotic analysis of a Hiemenz flow in a low-porosity medium with phase change. **J. Fluid Mech.**, v. 698, p. 185–210, 2012. 8, 49
- _____. Flame sheet model for the burning of a low-volatility liquid fuel in a low-permeability medium under low rates of strain. **Combust. Flame**, v. 160, p. 2783–2799, 2013. 8, 78, 79
- KOKUBUN, M. A. E.; PEREIRA, F. M.; FACHINI, F. F. Analytical study of stretched ultra-lean premixed flames within porous inert media. **Proc. Combust. Institute**, v. 34, p. 839–845, 2013. 1, 16
- KUKUCK, S.; MATALON, M. The onset of oscillations in diffusion flames. **Combust. Theory Modelling**, v. 5, p. 217–240, 2001. 113
- LAEVSKII, Y. M.; BABKIN, V. S. Stabilized gas combustion wave in an inert porous medium. **Combust. Expl. Shock Waves**, v. 44, p. 502–508, 2008. 2
- LEE, D.; VAFAI, K. Analytical characterization and conceptual assessment of solid and fluid temperature differentials in porous media. **Int. J. Heat Mass Transf.**, v. 42, p. 423–435, 1999. 30
- LEHMANN, P.; ASSOULINE, S.; OR, D. Characteristic length scales affecting evaporative drying of porous media. **Phys. Rev. E**, v. 77, 2008. 48
- LIÑAN, A. The asymptotic structure of counterflow diffusion flames for large activation energies. **Acta Astronautica**, v. 1, p. 1007–1039, 1974. 87, 103, 120

- LIU, S.; FOTACHE, C. G.; CHAO, B. H.; HAUTMAN, D. J.; OCHS, S. S. Boundary layer modeling of reactive flow over a porous surface with angled injection. **Combust. Flame**, v. 154, p. 378–386, 2008. 67
- MAILYBAEV, A. A.; BRUINING, J.; MARCHESIN, D. Analysis of in situ combustion of oil with pyrolysis and vaporization. **Combust. Flame**, v. 158, p. 1097–1108, 2011. 1, 68
- MARTYNENKO, V. V.; ECHIGO, R.; YOSHIDA, H. Mathematical model of self-sustaining combustion in inert porous medium with phase change under complex heat transfer. **Int. J. Heat Mass Transf.**, v. 41, p. 117–126, 1998. 3, 67
- MATALON, M.; LUDFORD, G. S. S. Chambered diffusion flames for different supply temperatures. **Acta Astronautica**, v. 6, p. 1377–1386, 1979. 9, 87, 118
- MATALON, M.; LUDFORD, G. S. S.; BUCKMASTER, J. Diffusion flames in a chamber. **Acta Astronautica**, v. 6, p. 943–959, 1979. 9, 87, 118
- METZENER, P.; MATALON, M. Diffusive-thermal instabilities of diffusion flames: onset of cells and oscillations. **Combust. Theory Modelling**, v. 10, p. 701–725, 2006. 113
- MIN, D. K.; SHIN, H. D. Laminar premixed flame stabilized inside a honeycomb ceramic. **Int. J. Heat Mass Transf.**, v. 34, p. 341–356, 1991. 16
- MITAL, R.; GORE, J. P.; VISKANTA, R. A Study of the Structure of Submerged Reaction Zone in Porous Ceramic Radiant Burners. **Combust. Flame**, v. 111, p. 175–184, 1997. 4
- MUJEEBU, M. A.; ABDULLAH, M. Z.; BAKAR, M. Z. A.; MOHAMAD, A. A.; ABDULLAH, M. K. A review of investigations on liquid fuel combustion in porous inert media. **Prog. En. Combust. Sci.**, v. 35, p. 216–230, 2009. 67
- MUJEEBU, M. A.; ABDULLAH, M. Z.; MOHAMAD, A.; BAKAR, M. A. Trends in modelling of porous media combustion. **Prog. En. Combust. Sci.**, v. 36, p. 627–650, 2010. 1
- NARAYAN, K. A.; WALSH, B. W. An experimental investigation of hydrocarbon recovery from a porous medium by continuous steam injection. **Fuel**, v. 67, p. 215–220, 1988. 48

- PEREIRA, F.; OLIVEIRA, A.; FACHINI, F. Asymptotic analysis of stationary adiabatic premixed flames in porous inert media. **Combust. Flame**, v. 156, p. 152–165, 2009. 2, 3, 16
- _____. Theoretical analysis of ultra-lean premixed flames in porous inert media. **J. Fluid Mech.**, v. 657, p. 285–307, 2010. 1, 3, 16
- PEREIRA, F. M. **Estudo analítico da estrutura de chamas adiabáticas pré-misturadas em meios porosos inertes e desenvolvimento de um modelo de curvas de nível para simulações numéricas**. PhD Thesis (PhD) — Universidade Federal de Santa Catarina, 2009. 12, 14
- PEREIRA, F. M.; OLIVEIRA, A. A. M.; FACHINI, F. F. Maximum superadiabatic temperature for stabilized flames within porous inert media. **Combust. Flame**, v. 158, p. 2283–2288, 2011. 3, 16
- RADULESCU, M. I.; MAXWELL, B. M. The mechanism of detonation attenuation by a porous medium and its subsequent re-initiation. **J. Fluid Mech.**, v. 667, p. 96–134, 2011. 1
- RAJU, M. P.; T' IEN, J. S. Heat and Mass Transports in a One-Dimensional Porous Wick Driven by a Gas-Phase Diffusion Flame. **J. Porous Media**, v. 10, p. 327–342, 2007. 4, 5, 20, 68, 88
- RAMESH, P. S.; TORRANCE, K. E. Boiling in a porous layer heated from below: effects of natural convection and a moving liquid/two-phase interface. **J. Fluid Mech.**, v. 257, p. 289–309, 1993. 47
- REES, D. A. S.; BASSOM, A. P.; SIDDHESHWAR, P. G. Local thermal non-equilibrium effects arising from the injection of a hot fluid into a porous medium. **J. Fluid Mech.**, v. 594, p. 379–398, 2008. 47
- ROY, N. C.; HOSSAIN, A.; NAKAMURA, Y. A universal model of opposed flow combustion of solid fuel over an inert porous medium. **Combust. Flame**, v. 161, p. 1645–1658, 2014. 2, 69
- SCHLICHTING, H. **Boundary-layer theory**. New York: McGraw-Hill, 1968. 81–86 p. 22
- SESHADRI, K.; HUMER, S.; SEISER, R. Activation-energy asymptotic theory of autoignition of condensed hydrocarbon fuels in non-premixed flows with comparison to experiment. **Combust. Theory Modelling**, v. 12, p. 831–855, 2008. 20

- SIBULKIN, M. Free convection diffusion flames from burning solid fuels. **Prog. En. Combust. Sci.**, v. 14, p. 195–212, 1988. 87, 119
- STELZNER, B.; KERAMIOTIS, C.; VOSS, S.; FOUNTI, M. A.; TRIMIS, D. Analysis of the flame structure for lean methane-air combustion in porous inert media by resolving the hydroxyl radical. **Proc. Combust. Institute**, In Press, 2014. 4
- TAKENO, T.; SATO, K. An excess enthalpy flame theory. **Combust. Sci. Tech.**, v. 20, p. 73–84, 1979. 1
- TELENGATOR, A. M.; MARGOLIS, S. B.; WILLIAMS, F. A. Stability of quasi-steady deflagrations in confined porous energetic materials. **Combust. Sci. Tech.**, v. 160, p. 259–315, 2000. 1
- TIEN, J. S. Diffusion flame extinction at small stretch rates: the mechanism of radiative loss. **Combust. Flame**, v. 65, p. 31–34, 1986. 87, 119
- TIEN, J. S.; SINGHAL, S. N.; HARROLD, D. P.; PRAHL, J. M. Combustion and Extinction in the Stagnation-Point Boundary Layer of a Condensed Fuel. **Combust. Flame**, v. 33, p. 55–68, 1978. 26
- TSENG, C.; HOWELL, J. Combustion of liquid fuels in a porous radiant burner. **Combust. Sci. Tech.**, v. 112, p. 141–161, 1996. 3
- VAFAI, K. **Handbook of porous media**. Boca Raton, FL: CRC Press, 2005. 607–645 p. 1, 15
- VAFAI, K.; KIM, S. K. Analysis of surface enhancement by a porous substrate. **J. Heat Transfer**, v. 112, p. 700–706, 1990. 29
- VOGEL, B. J.; ELLZEY, J. L. Subadiabatic and superadiabatic performance of a two-section porous burner. **Combust. Sci. Tech.**, v. 177, p. 1323–1338, 2005. 16
- WANG, H. Y.; CHEN, W. H.; LAW, C. K. Extinction of counterflow diffusion flames with radiative heat loss and nonunity Lewis numbers. **Combust. Flame**, v. 148, p. 100–116, 2007. 9, 87, 119
- WEINBERG, F. Combustion temperatures: the future? **Nature**, v. 233, p. 239–241, 1971. 1
- WHITAKER, S. The Forchheimer equation: a theoretical development. **Transport in Porous Media**, v. 25, p. 27–61, 1996. 15

- WILLIAMS, F. A. **Combustion theory**. 2. ed. [S.l.]: The Benjamin/Cummings Publishing Company, 1985. 11
- WOOD, S.; HARRIS, A. T. Porous burners for lean-burn applications. **Prog. En. Combust. Sci.**, v. 34, p. 667–684, 2008. 1, 16
- WOODS, A. W. Liquid and vapour flow in superheated rock. **Annu. Rev. Fluid Mech.**, v. 31, p. 171–199, 1999. 47
- WU, Q.; WEINBAUM, S.; ANDREOPOULOS, Y. Stagnation-point flows in a porous medium. **Chem. Engng Sci.**, v. 60, p. 123–134, 2005. 25, 37, 42, 43
- YARIN, L. P.; SUKHOV, G. S. On filtration combustion reactor theory. **Combust. Sci. Tech.**, v. 84, p. 15–32, 1992. 2
- YORTSOS, Y. C.; STUBOS, A. K. Phase change in porous media. **Curr. Opin. Colloid Interface Sci.**, v. 6, p. 208–216, 2001. 47
- ZHAO, T. S. Coupled heat and mass transfer of a stagnation point flow in a heated porous bed with liquid film evaporation. **Int. J. Heat Mass Transf.**, v. 42, p. 861–872, 1999. 47
- ZHAO, T. S.; LIAO, Q. On capillary-driven flow and phase-change heat transfer in a porous structure heated by a finned surface: measurements and modeling. **Int. J. Heat Mass Transf.**, v. 43, p. 1141–1155, 2000. 5, 20, 21, 88
- ZHDANOK, S.; KENNEDY, L. A.; KOESTER, G. Superadiabatic combustion of methane air mixtures under filtration in a packed bed. **Combust. Flame**, v. 100, p. 221–231, 1995. 2

APPENDIX A: ASYMPTOTIC ANALYSIS OF EXTINCTION OF A DIFFUSION FLAME IN A POROUS CHAMBER

In this Appendix we analyze a steady, planar diffusion flame established inside an inert porous chamber. Gaseous fuel is injected from the bottom at a constant velocity and mixes with the oxidant that is entering the porous chamber through diffusion. The reactants mix at the molecular level and reacts in a diffusion flame. A schematic of the problem considered here is presented in Fig. A.1.

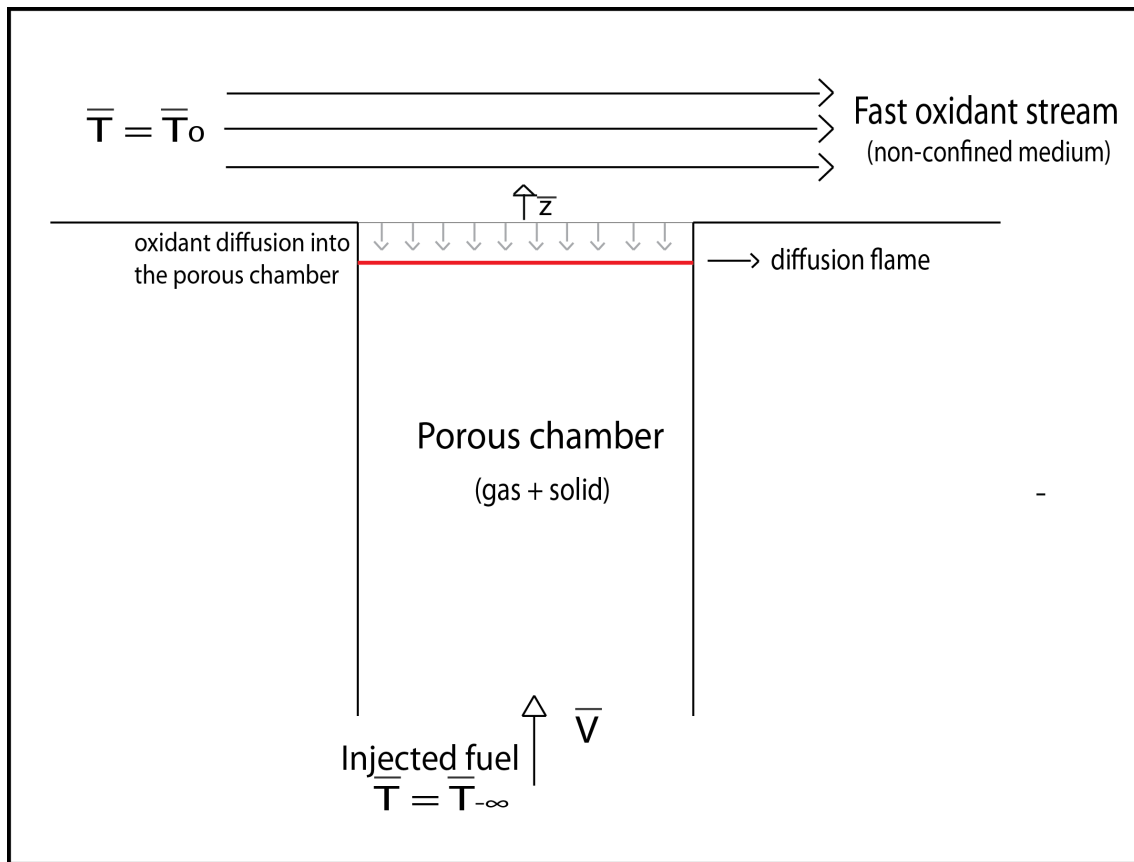


Figure A.1 - Schematic of the present problem.

The solid is heated due to the heat release at the flame sheet. It then transports this heat to both sides of the flame, pre-heating the incoming reactants. At the top of the chamber, due to the difference on the conductivities, the phases have different temperature values. The gas is at thermal equilibrium with the outer stream at a temperature \bar{T}_0 , while the solid is at a higher temperature \bar{T}_{s0} (that must be determined). Due to this difference, the solid loses heat to the outer flow.

We consider a single-step chemical reaction of the Arrhenius type. Due to the energy generation in the gas phase we must consider a two-equation model for the gas-solid system. The porous medium is considered isotropic and dispersion effects are neglected, such that the effective thermal conductivities are order zero tensors. Hence, the gas and solid conservation equations are coupled only through the interfacial convective heat transfer coefficient h .

The major findings are related with the low flame temperatures achieved, when compared to non-confined problems, and with the extinction limits. The extinction diagram, when presented as a function of the injection velocity, shows the existence of two distinct extinction points, one associated with a high velocity, and the other associated with a low velocity. The high-injection-velocity extinction point is associated with kinetic extinction (low residence time for the reactants in the flame sheet). The low-injection-velocity extinction point is associated with high values of the interphase heat exchange.

It is interesting to point that the existence of two extinction points was already recognized in the literature, and the low extinction point was associated with heat losses with a high Damkohler number. In the present case, on the other hand, the low extinction point (low injection velocity) is associated with a low value of the Damkohler number. This occurs because the stoichiometric temperature is reduced when the injection velocity is large (due to the enhancement of the interphase heat exchange), which leads to a decrease on the reactive Damkohler number.

The results to be presented in the following were obtained in partnership with Professor Moshe Matalon, from the University of Illinois at Urbana-Champaign.

A.1 Mathematical formulation

We consider a characteristic length¹ given by $l_s = \lambda_s / (\bar{\rho} c_p \bar{V})$, with λ_s the thermal conductivity of the solid, $\bar{\rho}$ the gas density, c_p the gas specific heat capacity at constant pressure and \bar{V} the injection velocity of the gaseous fuel. Mass fractions are non-dimensionalized with respect to their initial values $\bar{Y}_{F-\infty}$ and \bar{Y}_{O0} , for fuel and oxidant, respectively. The temperatures are non-dimensionalized with respect to q/c_p , with $q \equiv Q\bar{Y}_{F-\infty}$ being the heat released per unit mass of fuel.

The non-dimensional governing equations are then given by

¹Note that the characteristic length scale given here is different than the one used in previous Chapters.

$$\frac{dY_F}{dz} - \frac{1}{\Gamma L_F} \frac{d^2 Y_F}{dz^2} = -\Gamma Da Y_F Y_O e^{-T_a/T_g}, \quad (\text{A.1})$$

$$\frac{dY_O}{dz} - \frac{1}{\Gamma L_O} \frac{d^2 Y_O}{dz^2} = -\Gamma \phi Da Y_F Y_O e^{-T_a/T_g}, \quad (\text{A.2})$$

$$\frac{dT_g}{dz} - \frac{1}{\Gamma} \frac{d^2 T_g}{dz^2} = \Gamma Da Y_F Y_O e^{-T_a/T_g} + \Gamma N (T_s - T_g), \quad (\text{A.3})$$

$$-p \frac{d^2 T_s}{dz^2} = -\Gamma N (T_s - T_g), \quad (\text{A.4})$$

where L_F and L_O are the fuel and oxidant Lewis numbers, respectively, $\phi \equiv \bar{\phi} \bar{Y}_{F-\infty} / \bar{Y}_{O0}$ is the initial mixture strength, $Da \equiv B \lambda_g \bar{Y}_{O0} / (c_p \bar{V}^2)$ is the Damkohler number with B the frequency factor and we define $N \equiv \lambda_g h / (\varphi (\bar{\rho} c_p \bar{V})^2)$ as the heat exchange parameter and $p \equiv (1 - \varphi) / \varphi$ as the porosity parameter, with φ being the porosity and h the volumetric surface-convection coefficient.

The non-dimensionalization process introduces the parameter $\Gamma \equiv \lambda_s / \lambda_g$, the solid-to-gas thermal conductivities ratio. In this problem we consider the asymptotic limit $\Gamma \gg 1$. Hence, one can see that we introduce a far-field length-scale, in which convection is dominant and a region of the order of Γ^{-1} from the top of the chamber in which convection and diffusion transport balance. Since in the convective, far-field region, the solution for the oxidant mass fraction is given by $Y_O = 0$ (due to the boundary condition for $z \rightarrow -\infty$), the chemical reaction is negligible in this region. Chemical reaction occurs in the convective-diffusive region, which is analyzed through the re-scaled spatial coordinate $\tilde{z} = \Gamma z$. In the limit of very high porosity, such that $p = O(\Gamma^{-1}) \ll 1$, it's easy to show that up to all orders $T_s = T_g = T_{-\infty}$ in the far-field. In this case, the consideration of the far-field length scale is not necessary and we can simply analyze the problem in the usual viscous length scale for non-confined problems (in this case, $\Gamma^{-1} l_s$). In Fig. A.2 we show a representative picture of the profiles in each length-scale.

Boundary conditions for $z \rightarrow -\infty$ are given by

$$Y_F = 1, \quad Y_O = 0, \quad T_s = T_g = T_{-\infty}. \quad (\text{A.5})$$

For the top of the chamber $z = 0$,

$$Y_F = 0, \quad Y_O = 1, \quad T_g = T_0, \quad (\text{A.6})$$

and considering a conductive heat loss model for the solid temperature, we have

$$\left. \frac{dT_s}{dz} \right|_0 = -K (T_{s0} - T_0), \quad (\text{A.7})$$

where $K \equiv \bar{K}/((1 - \varphi)\bar{\rho}c_p\bar{V})$ is the dimensionless heat loss parameter and T_{s0} is the solid temperature at the top of the chamber.

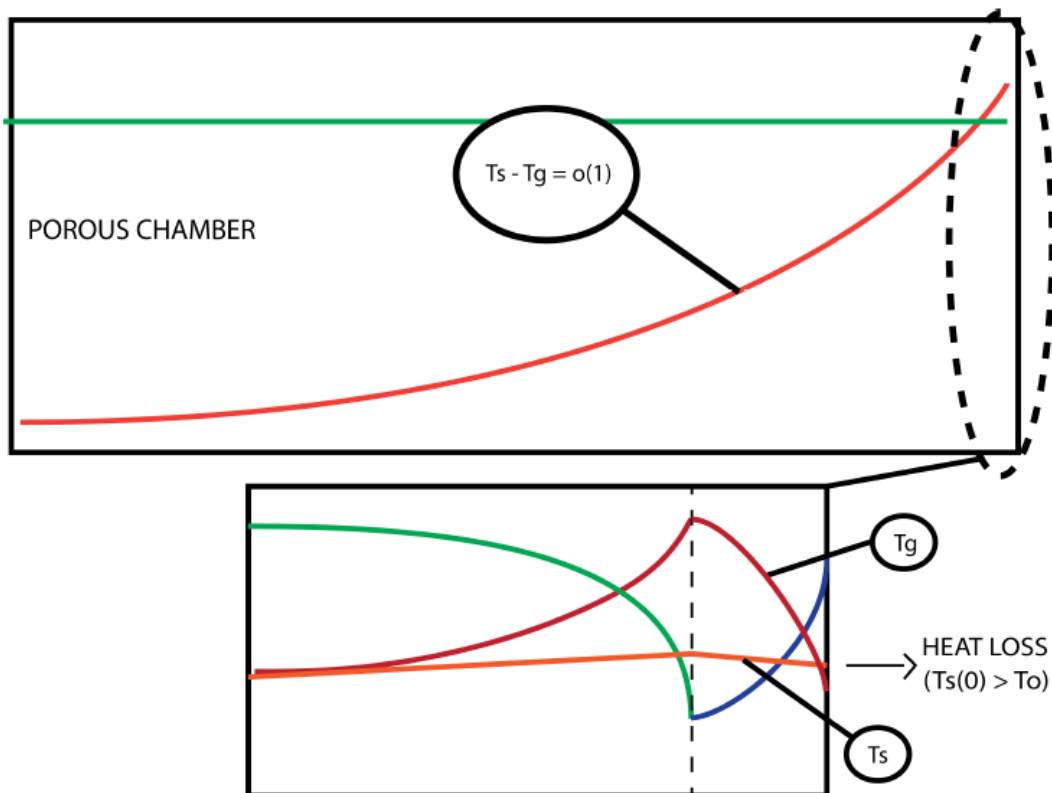


Figure A.2 - Representative profiles in the two length-scales.

The flame is located in a thin sheet and the variables experience jumps across it. To leading-order the reactants are completely consumed at this sheet and the gas temperature is the stoichiometric flame temperature (associated with the complete consumption of reactants). We follow the formulation derived by [Cheatham and Matalon \(2000\)](#) for the jumps across the flame sheet.

To leading-order the following jump relations must be satisfied across the flame sheet

$$[Y_{F(0)}] = [Y_{O(0)}] = [T_{g(0)}] = 0, \quad \left[\frac{dT_{g(0)}}{dz} \right] = -\frac{1}{L_F} \left[\frac{dY_{F(0)}}{dz} \right] = -\frac{1}{\phi L_O} \left[\frac{dY_{O(0)}}{dz} \right], \quad (\text{A.8})$$

in which $[F] = F(z_f^+) - F(z_f^-)$ denotes the jump across the flame sheet which is located at z_f (z_f^+ and z_f^- denotes the oxidant and fuel sides of the flame, respectively) and $F_{(0)}$ is the leading-order term of the expansion $F = F_{(0)} + \epsilon F_{(1)} + o(\epsilon)$.

Also, complete combustion is required for the leading-order reactants, such that

$$Y_{F(0)}|_{z_f} = Y_{O(0)}|_{z_f} = 0. \quad (\text{A.9})$$

To $O(\epsilon)$ the the following jump relations must be satisfied across the flame

$$[T_{g(1)}] = -L_F^{-1} [Y_{F(1)}] = -(\phi L_O)^{-1} [Y_{O(1)}], \quad (\text{A.10})$$

$$\left[T_{g(1)} - \frac{dT_{g(1)}}{dz} \right] = - \left[Y_{F(1)} - L_F^{-1} \frac{dY_{F(1)}}{dz} \right] = - \left[Y_{O(1)} - (\phi L_O)^{-1} \frac{dY_{O(1)}}{dz} \right], \quad (\text{A.11})$$

in which $\epsilon \equiv c_p R (\bar{T}_f^s)^2 / (q E_a)$ is the inverse of the activation energy parameter, with R the gas constant, E_a the activation energy and \bar{T}_f^s the dimensional flame temperature associated with complete combustion (or stoichiometric temperature).

For the solid phase, we must consider continuity of the temperature and its flux up to all orders

$$[T_s] = \left[\frac{dT_s}{dz} \right] = 0. \quad (\text{A.12})$$

Leakage of reactants through the flame sheet is given by the higher-order terms, such that

$$Y_{F(1)}(z_f^+) = L_F S_F(\gamma, \delta), \quad Y_{O(1)}(z_f^-) = \phi L_O S_O(\gamma, \delta), \quad (\text{A.13})$$

where S_F and S_O are the fuel and oxidant leakage functions, respectively. This leakage of reactants modifies the flame position. It is not so straight-forward to define the correction for the flame position η_f . The first choice would be the point where the temperature reach its peak, but in this case η_f must be determined numerically. Then, if we define η_f as the point where the correction for the flame temperature is continuous, we have

$$[T_{g(1)}] + \eta_f \left[\frac{dT_{g(0)}}{d\tilde{z}} \right] = 0, \quad (\text{A.14})$$

as the relation that defines the flame position correction η_f .

The auxiliary parameters that characterizes the internal flame structure are

$$\gamma \equiv \frac{dT_{g(0)}/dz|_{z_f^+} + dT_{g(0)}/dz|_{z_f^-}}{[dT_{g(0)}/dz]}, \quad \delta \equiv \frac{4\phi L_F L_O}{[dT_{g(0)}/dz]^2} D \exp \left\{ \frac{1+\gamma}{2} h_O^* + \frac{1-\gamma}{2} h_F^* \right\}, \quad (\text{A.15})$$

where γ is a parameter that depends on the temperature profiles for complete combustion and h_O^* and h_F^* are the excess/deficient enthalpy at the flame, given by

$$h_O^* = T_{f1}^- + \frac{1}{\phi L_O} Y_O^-, \quad h_F^* = T_{f1}^+ + \frac{1}{L_F} Y_F^+, \quad (\text{A.16})$$

where T_{f1} is the dimensionless correction of the flame temperature, which is expanded as $T_f = T_f^s + \epsilon T_{f1} + o(\epsilon)$.

The modified (reactive) Damkohler number D is given by

$$D = \epsilon^3 Da e^{-T_a/T_f^s}, \quad (\text{A.17})$$

where the usual distinguish limit of $D = O(1)$ is considered for the asymptotic analysis of the flame structure.

One can see that the excess enthalpy at the flame makes the relation between δ and D non-trivial. For zero excess enthalpy at the flame they are directly proportional to each other (a case that occurs for $L_i = 1$ in an adiabatic, non-confined problem), such that they represent the same physical state. In the present case, the excess enthalpy at the flame is induced by non-unitary Lewis numbers and by the heat exchange between gas and solid phases.

Cheatham and Matalon (2000) provided approximations for the leakage curves S_F and S_O . For the lower branch (solutions that tend to the Burke-Schumann limit of complete combustion when $\delta \rightarrow +\infty$) we have

$$S_O = a_0 \delta^{-4/3} \exp \{ -a_1 (\delta - \delta_c)^{a_2} \}, \quad (\text{A.18})$$

$$S_F = b_0 \delta^{-4/3} \exp \left\{ -b_1 (\delta - \delta_c)^{b_2} \right\}, \quad (\text{A.19})$$

with

$$a_0 = 0.61923 + 3.2523|\gamma| + 0.52069|\gamma|^2,$$

$$a_1 = 1.9077 - 1.901|\gamma| + 1.055|\gamma|^2,$$

$$a_2 = 0.46137 - 0.15374|\gamma| - 0.06769|\gamma|^4 - 0.23288|\gamma|^6,$$

$$\begin{aligned}
b_0 &= 0.61923(1 - |\gamma|)^{15} \exp \{10.469|\gamma|\}, \\
b_1 &= 1.9077 + 11.588|\gamma|^2 - 17.014|\gamma|^4 + 55.865|\gamma|^6, \\
b_2 &= 0.46137 + 0.27706|\gamma| - 0.2029|\gamma|^2.
\end{aligned}$$

For the upper branch (solutions that corresponds to states with increasingly large leakage of reactants and which become invalid when δ is sufficiently large)

$$S_O = \delta^{-1/3} \{q_0 + q_1 (\delta - \delta_c)^{q_2}\}, \quad (\text{A.20})$$

$$S_F = \delta^{-1/3} \{r_0 + r_1 (\delta - \delta_c)^{r_2}\}, \quad (\text{A.21})$$

$$q_0 = 0.72704 (1 - |\gamma|)^{-0.63858} \exp \{1.4311|\gamma|^{0.5696}\},$$

$$q_1 = 2.7108 + \frac{10.788 \tan(\pi|\gamma|/2)}{1 + 2.5459|\gamma| - 2.8114|\gamma|^2},$$

$$q_2 = 0.625,$$

$$r_0 = 0.72704 (1 - |\gamma|)^{15} \exp \{10.451|\gamma|\},$$

$$r_1 = 2.7108 (1 - |\gamma|)^{5.8507},$$

$$r_2 = 0.625 - 0.49221|\gamma| + 2.0203|\gamma|^2 - 4.2464|\gamma|^3 + 4.2286|\gamma|^4.$$

It is worth to note that the above approximations were obtained for $-1 < \gamma \leq 0$, which is the case when more heat is transported to the fuel side. When $0 \leq \gamma < 1$, the roles of S_F and S_O must be interchanged.

In the above expressions, the critical δ_c was obtained by Liñan (1974) and it is given by

$$\delta_c = e \{ (1 - |\gamma|) - (1 - |\gamma|)^2 + 0.26(1 - |\gamma|)^3 + 0.055(1 - |\gamma|)^4 \}. \quad (\text{A.22})$$

When $N \gg 1$, gas and solid temperature approach each other. In this case, $[dT_g/d\tilde{z}] \sim [dT_s/d\tilde{z}]$ and it can be shown from the addition of Eqs. A.3 and A.4 that

$$\gamma = - \left[\frac{dT_{(0)}}{d\tilde{z}} \right] (1 + \Gamma p). \quad (\text{A.23})$$

Then, unless $p = O(\Gamma^{-1})$ (high-porosity) or $[dT_{(0)}/d\tilde{z}] = O(\Gamma^{-1})$ (small heat release), γ will be large because $\Gamma \gg 1$. For $|\gamma| > 1$, there is $O(1)$ reactant leakage from the flame. Hence, when $N \gg 1$ the flame will fall into Liñan's premixed flame regime (LIÑAN, 1974) and a different asymptotic treatment is required.

The dimensional heat exchange coefficient h is modeled following Fu et al. (1998) and gives a dimensionless parameter N as

$$N = \varphi^{(m'-4)/2} \left(\frac{\lambda_g}{c_p} \right)^2 \frac{C'}{\mu^{m'}} \left(\bar{\rho} \bar{V} \sqrt{\frac{4}{\pi}} \frac{1}{39.37 \bar{\varphi}} \right)^{m'-2}, \quad (\text{A.24})$$

in which C' and m' are experimentally-determined constants, μ is the gas-phase kinematic viscosity and $\bar{\varphi}$ is the linear-pore density. Note that in this Appendix we consider the correlations between the interphase heat exchange coefficient h , the porosity φ and the flow velocity \bar{V} , differently than in the previous Chapters. We do so here because the flow field is trivial and given by the constant value \bar{V} of the injection velocity, and in the previous Chapters the flow field is more complex.

It is important to note that the formulation introduces two different perturbation parameters, ϵ and Γ^{-1} , the first being associated with incomplete combustion and leakage of reactants through the flame-sheet, and the second being associated with the difference between gas and solid heat transport. For the sake of simplicity, we analyze the distinguished limit of $\Gamma^{-1} \sim \epsilon$, such that we consider $\epsilon = c\Gamma^{-1}$, with $c = O(1)$ being a proportionality constant.

A.2 Far-field, convective region

It is easy to show that mass fraction solutions in the far-field, convective region, are simply given by $Y_F(z) = 1$ and $Y_O(z) = 0$ when the asymptotic limit of $\Gamma \gg 1$ is considered. Hence, chemical reaction is negligible in the convective region. Then, one can manipulate energy equations and obtain

$$\frac{dT_g}{dz} - \frac{1}{\Gamma} \frac{d^2T_g}{dz^2} - p \frac{d^2T_s}{dz^2} = 0, \quad (\text{A.25})$$

$$-p \frac{d^2T_s}{dz^2} = -\Gamma N (T_s - T_g). \quad (\text{A.26})$$

One can see that the leading-order term for both phases is equal, as the heat exchange term is dominant in the second equation. Hence, we expand gas and solid solutions in series as

$$T_s(z) = T_{(0)} + \Gamma^{-1} T_{s(1)} + o(\Gamma^{-1}), \quad (\text{A.27})$$

$$T_g(z) = T_{(0)} + \Gamma^{-1} T_{g(1)} + o(\Gamma^{-1}), \quad (\text{A.28})$$

where we emphasize that the temperature difference arises only in the higher-order terms.

Substituting the proposed solutions into the set of governing equations, we obtain leading and higher-order equations as

$$\frac{dT_{(0)}}{dz} - p \frac{d^2 T_{(0)}}{dz^2} = 0, \quad (\text{A.29})$$

$$\frac{dT_{g(1)}}{dz} - \frac{d^2 T_{(0)}}{dz^2} - p \frac{d^2 T_{s(1)}}{dz^2} = 0, \quad (\text{A.30})$$

$$-p \frac{d^2 T_{(0)}}{dz^2} = -N(T_{s(1)} - T_{g(1)}). \quad (\text{A.31})$$

Leading-order solution is given by

$$T_{(0)}(z) = T_{-\infty} + c_0 e^{z/p}, \quad (\text{A.32})$$

where c_0 is a constant. If we integrate the higher-order equation for the gas-phase and apply the result for $z \rightarrow -\infty$, we have the relation

$$T_{g(1)} = T'_{(0)} + pT'_{s(1)}, \quad (\text{A.33})$$

where the prime denotes differentiation with respect to z . Substituting this in the higher-order equation for the solid-phase we obtain

$$pT'_{s(1)} - T_{s(1)} = -\frac{c_0}{p} \left(1 + \frac{1}{N}\right) e^{z/p}. \quad (\text{A.34})$$

Hence, the higher-order solution for the solid is given by

$$T_{s(1)}(z) = c_1 e^{z/p} - c_0 \left(1 + \frac{1}{N}\right) \frac{z}{p^2} e^{z/p}, \quad (\text{A.35})$$

where c_1 is a constant. Higher-order solution for the gas-phase is straight-forward obtained as

$$T_{g(1)}(z) = c_1 e^{z/p} - \frac{c_0}{N p} e^{z/p} - c_0 \left(1 + \frac{1}{N}\right) \frac{z}{p^2} e^{z/p}. \quad (\text{A.36})$$

Then, temperature solutions in the convective region are given by

$$T_g(z) = T_{-\infty} + c_0 e^{z/p} + \Gamma^{-1} \left\{ c_1 e^{z/p} - \frac{c_0}{N p} e^{z/p} - c_0 \left(1 + \frac{1}{N}\right) \frac{z}{p^2} e^{z/p} \right\} + o(\Gamma^{-1}), \quad (\text{A.37})$$

$$T_s(z) = T_{-\infty} + c_0 e^{z/p} + \Gamma^{-1} \left\{ c_1 e^{z/p} - c_0 \left(1 + \frac{1}{N}\right) \frac{z}{p^2} e^{z/p} \right\} + o(\Gamma^{-1}). \quad (\text{A.38})$$

It is easy to see that when $N \gg 1$ (very intense interphase heat exchange), $T_s \rightarrow T_g$, while for $p \ll 1$ (very high porosity), $\{T_s, T_g\} \rightarrow T_{-\infty}$. The unknown constants c_0

and c_1 are to be determined.

A.3 Convective-diffusive region

In a length scale of the order of Γ^{-1} close to $z = 0$, consumption of reactants is observed, as it is in this region that convection and diffusion reactants transport balance. Hence, in order to analyze this region we stretch the spatial coordinate as $\tilde{z} = \Gamma z$ and obtain the following governing equations

$$\frac{dY_F}{d\tilde{z}} - \frac{1}{L_F} \frac{d^2 Y_F}{d\tilde{z}^2} = -Da Y_F Y_O e^{-T_a/T_g}, \quad (\text{A.39})$$

$$\frac{dY_O}{d\tilde{z}} - \frac{1}{L_O} \frac{d^2 Y_O}{d\tilde{z}^2} = -\phi Da Y_F Y_O e^{-T_a/T_g}, \quad (\text{A.40})$$

$$\frac{dT_g}{d\tilde{z}} - \frac{d^2 T_g}{d\tilde{z}^2} = Da Y_F Y_O e^{-T_a/T_g} + N (T_s - T_g), \quad (\text{A.41})$$

$$-\Gamma p \frac{d^2 T_s}{d\tilde{z}^2} = -N(T_s - T_g). \quad (\text{A.42})$$

Boundary conditions for $\tilde{z} = 0$ are given by

$$T_g = T_g(0), \quad Y_F = 0, \quad Y_O = 1, \quad \Gamma \left. \frac{dT_s}{d\tilde{z}} \right|_0 = -K (T_s(0) - T_g(0)). \quad (\text{A.43})$$

We seek solutions in powers of $\epsilon = c\Gamma^{-1}$, or

$$Y_F(\tilde{z}) = Y_{F(0)} + \epsilon Y_{F(1)} + o(\epsilon), \quad (\text{A.44})$$

$$Y_O(\tilde{z}) = Y_{O(0)} + \epsilon Y_{O(1)} + o(\epsilon), \quad (\text{A.45})$$

$$T_g(\tilde{z}) = T_{g(0)} + \epsilon T_{g(1)} + o(\epsilon), \quad (\text{A.46})$$

$$T_s(\tilde{z}) = T_{s(0)} + \epsilon T_{s(1)} + o(\epsilon). \quad (\text{A.47})$$

For the mass fractions we have the following solutions (utilizing the boundary con-

ditions and jumps at the flame sheet shown previously)

$$Y_F(\tilde{z}) = \left\{ \begin{array}{l} 1 - e^{(\tilde{z}-\tilde{z}_f)L_F} \\ + \\ \epsilon \left\{ 1 + S_O/S_F - \left\{ \frac{L_F/L_O}{\phi+(1-\phi)e^{\tilde{z}_f L_O}} \right\} \left(\frac{1-e^{\tilde{z}_f L_O}}{1-e^{\tilde{z}_f L_F}} \right) \right\} L_F S_F e^{(\tilde{z}-\tilde{z}_f)L_F}, \quad \text{for } \tilde{z} < \tilde{z}_f \\ \epsilon L_F S_F (1 - e^{\tilde{z}L_F}) / (1 - e^{\tilde{z}_f L_F}), \quad \text{for } \tilde{z} > \tilde{z}_f \end{array} \right\}, \quad (\text{A.48})$$

$$Y_O(\tilde{z}) = \left\{ \begin{array}{l} \epsilon \phi L_O S_O e^{(\tilde{z}-\tilde{z}_f)L_O}, \quad \text{for } \tilde{z} < \tilde{z}_f \\ 1 - \left(\frac{1-e^{\tilde{z}L_O}}{1-e^{\tilde{z}_f L_O}} \right) + \epsilon L_F S_F \frac{\phi}{\phi+(1-\phi)e^{\tilde{z}_f L_O}} \left(\frac{1-e^{L_O \tilde{z}}}{1-e^{L_O \tilde{z}_f}} \right) \quad \text{for } \tilde{z} > \tilde{z}_f. \end{array} \right\}. \quad (\text{A.49})$$

Note that $Y_F = O(\epsilon)$ for $\tilde{z} > \tilde{z}_f$ and $Y_O = O(\epsilon)$ for $\tilde{z} < \tilde{z}_f$, which denotes the small leakage of reactants across the flame sheet.

Leading-order solution for the solid is given by

$$T_{s(0)}(\tilde{z}) = (c_0 + T_{-\infty}), \quad (\text{A.50})$$

where matching with the far-field region was imposed.

Leading-order equation for the gas is given by

$$T'_{g(0)} - T''_{g(0)} + N T_{g(0)} = N(c_0 + T_{-\infty}). \quad (\text{A.51})$$

where prime denotes differentiation with respect to \tilde{z} . This equation must be solved for both sides of the flame.

The general solution is given by

$$T_{g(0)}(\tilde{z}) = (c_0 + T_{-\infty}) + e^{\tilde{z}/2} (K_1 e^{A\tilde{z}/2} + K_2 e^{-A\tilde{z}/2}), \quad (\text{A.52})$$

where $A \equiv \sqrt{4N + 1}$ comes from the characteristic equation of the homogeneous solution.

For the fuel side, $\tilde{z} < \tilde{z}_f$, matching with the far-field solution gives $K_2^- = 0$. Then, leading-order solution of the gas in the fuel side is given by

$$T_{g(0)}(\tilde{z} < \tilde{z}_f) = (c_0 + T_{-\infty}) + c_2 e^{(1+A)\tilde{z}/2}, \quad (\text{A.53})$$

where $c_2 = K_1^-$ is to be determined.

For the oxidant side, condition at the top of the chamber gives $K_2^+ = -K_1^+ - c_0 + \Delta T$, where $\Delta T = T_0 - T_{-\infty}$ is the temperature differential across the chamber. Then, we have

$$T_{g(0)}(\tilde{z} > \tilde{z}_f) = (c_0 + T_{-\infty}) + c_3 e^{(1+A)\tilde{z}/2} - (c_0 - \Delta T + c_3) e^{(1-A)\tilde{z}/2}, \quad (\text{A.54})$$

where $K_1^+ = c_3$ is to be determined.

Higher-order equation for the solid is given by

$$c p T_{s(1)}'' + N T_{g(0)} - N(c_0 + T_{-\infty}) = 0. \quad (\text{A.55})$$

For the fuel side the following equation holds

$$c p \frac{d^2 T_{s(1)}}{d\tilde{z}^2} + N c_2 e^{(1+A)\tilde{z}/2} = 0. \quad (\text{A.56})$$

Then, higher-order solution for the solid on the fuel side is given by

$$T_{s(1)}(\tilde{z} < \tilde{z}_f) = \frac{c_0}{c p} \tilde{z} + \frac{c_1}{c} - \frac{4N c_2}{c p(1+A)^2} e^{(1+A)\tilde{z}/2}, \quad (\text{A.57})$$

where matching with the far-field was imposed.

For the oxidant side, $\tilde{z} > \tilde{z}_f$, we have the following governing equation

$$c p T_{s(1)}'' - N(c_0 - \Delta T + c_3) e^{(1-A)\tilde{z}/2} + N c_3 e^{(1+A)\tilde{z}/2} = 0. \quad (\text{A.58})$$

General solution is given by

$$T_{s(1)}(\tilde{z} > \tilde{z}_f) = K_1^+ + K_2^+ \tilde{z} + \frac{e^{(1-A)\tilde{z}/2}}{4Nc p} \left\{ (c_0 - \Delta T + c_3) (1+A)^2 - c_3 e^{A\tilde{z}} (1-A)^2 \right\}. \quad (\text{A.59})$$

Up to leading-order the solid is at a constant temperature $c_0 + T_{-\infty}$. At the top of the chamber, we have $T_s(0) = (c_0 + T_{-\infty}) + \Gamma^{-1} T_{s1} + o(\Gamma^{-1})$. The correction of the order of Γ^{-1} (T_{s1}) would have to be obtained from the heat loss condition at the top of the chamber for the $O(\Gamma^{-1})$ terms. For the present problem and discussion, it is enough to consider $T_{s1} = 0$, such that the condition at the top of the chamber

$T_{s(1)}(0) = 0$ determines

$$K_1^+ = -\frac{1}{4Ncp} \left\{ (c_0 - \Delta T + c_3)(1+A)^2 - c_3(1-A)^2 \right\}, \quad (\text{A.60})$$

such that

$$T_{s(1)}(\tilde{z} > \tilde{z}_f) = K_2^+ \tilde{z} - \frac{1}{4Ncp} \left\{ (c_0 - \Delta T + c_3)(1+A)^2 (1 - e^{(1-A)\tilde{z}/2}) - c_3(1-A)^2 (1 - e^{(1+A)\tilde{z}/2}) \right\}. \quad (\text{A.61})$$

Applying the heat loss condition at the top of the chamber and collecting $O(1)$ terms, we have

$$c \left. \frac{dT_{s(1)}}{d\tilde{z}} \right|_0 = -K(c_0 - \Delta T), \quad (\text{A.62})$$

which determines the constant K_2^+ in terms of c_3 and c_0 as

$$K_2^+ = -\frac{K}{c}(c_0 - \Delta T) - \frac{1}{4Ncp} \left\{ (c_0 - \Delta T + c_3)(1+A)^2 \frac{(1-A)}{2} - c_3(1-A)^2 \frac{(1+A)}{2} \right\}. \quad (\text{A.63})$$

Then we have the following solution

$$T_{s(1)}(\tilde{z} > \tilde{z}_f) = -\frac{K}{c}(c_0 - \Delta T)\tilde{z} - \frac{1}{4Ncp} \left\{ (c_0 - \Delta T + c_3)(1+A)^2 \left(1 - e^{(1-A)\tilde{z}/2} + \frac{(1-A)\tilde{z}}{2} \right) - c_3(1-A)^2 \left(1 - e^{(1+A)\tilde{z}/2} + \frac{(1+A)\tilde{z}}{2} \right) \right\}. \quad (\text{A.64})$$

Higher-order equation for the gas is given by

$$T'_{g(1)} - T''_{g(1)} + NT_{g(1)} = NT_{s(1)}, \quad (\text{A.65})$$

which must be solved for both sides of the flame.

For the fuel side we have the following governing equation

$$T'_{g(1)} - T''_{g(1)} + NT_{g(1)} = N \left\{ \frac{c_1}{c} + \frac{c_0}{c} \tilde{z} - \frac{4N c_2}{c p (1+A)^2} e^{(1+A)\tilde{z}/2} \right\}. \quad (\text{A.66})$$

General solution (discarding the exponentially large term) is given by

$$T_{g(1)}(\tilde{z} < \tilde{z}_f) = c_4 e^{(1+A)\tilde{z}/2} + \left(\frac{c_1}{c} - \frac{c_0}{Ncp} + \frac{c_0}{c} \tilde{z} \right) + \frac{4N^2 c_2}{A^2(1+A)^2 c p} (A\tilde{z} - 1) e^{(1+A)\tilde{z}/2}. \quad (\text{A.67})$$

One can see that this solution matches properly with the far-field solution. The integration constant $c_4 = K_1^-$ is determined from the condition of continuity at the flame (higher-order terms).

For the oxidant side, we have the following governing equation

$$\begin{aligned} T'_{g(1)} - T''_{g(1)} + NT_{g(1)} = \\ N \left\{ -\frac{K}{c}(c_0 - \Delta T)\tilde{z} - \frac{1}{4Ncp} \left\{ (c_0 - \Delta T + c_3)(1+A)^2 \left(1 - e^{(1-A)\tilde{z}/2} + \frac{(1-A)\tilde{z}}{2} \right) - \right. \right. \\ \left. \left. c_3(1-A)^2 \left(1 - e^{(1+A)\tilde{z}/2} + \frac{(1+A)\tilde{z}}{2} \right) \right\} \right\}. \end{aligned} \quad (\text{A.68})$$

For the sake of compactness, we express the above in a general equation of the form

$$T'_{g(1)} - T''_{g(1)} + NT_{g(1)} = N \{ f_1 \tilde{z} + f_2 e^{(1-A)\tilde{z}/2} + f_3 e^{(1+A)\tilde{z}/2} + f_4 \}, \quad (\text{A.69})$$

where

$$f_1 = -\frac{K}{c}(c_0 - \Delta T) - \frac{1}{4Ncp} \left\{ (c_0 - \Delta T + c_3)(1+A)^2 \frac{(1-A)}{2} - c_3(1-A)^2 \frac{(1+A)}{2} \right\}, \quad (\text{A.70})$$

$$f_2 = \frac{1}{4Ncp}(c_0 - \Delta T + c_3)(1+A)^2, \quad f_3 = -\frac{1}{4Ncp}c_3(1-A)^2, \quad (\text{A.71})$$

$$f_4 = -\frac{1}{4Ncp} \{ (c_0 - \Delta T + c_3)(1+A)^2 - c_3(1-A)^2 \}. \quad (\text{A.72})$$

We have a general solution given by

$$\begin{aligned} T_{g(1)}(\tilde{z} > \tilde{z}_f) = \frac{(N f_4 - f_1)}{N} + f_1 \tilde{z} + \\ \frac{N}{A^2} f_2 (1 + A\tilde{z}) e^{(1-A)\tilde{z}/2} + \frac{N}{A^2} f_3 (1 - A\tilde{z}) e^{(1+A)\tilde{z}/2} + e^{\tilde{z}/2} \{ K_1^+ e^{A\tilde{z}/2} + K_2^+ e^{-A\tilde{z}/2} \}. \end{aligned} \quad (\text{A.73})$$

Again, for a matter of simplicity, we consider as a boundary condition at the top of the chamber $T_{g(1)}(0) = 0$. Hence, we obtain K_2^+ in terms of K_1^+ as

$$K_2^+ = -\frac{(N f_4 - f_1)}{N} - (f_2 + f_3) \frac{N}{A^2} - K_1^+. \quad (\text{A.74})$$

Then, higher-order solution for the gas in the oxidant side is given by

$$T_{g(1)}(\tilde{z} > \tilde{z}_f) = \frac{(N f_4 - f_1)}{N} \{1 - e^{(1-A)\tilde{z}/2}\} + f_1 \tilde{z} + \frac{N}{A} f_2 \tilde{z} e^{(1-A)\tilde{z}/2} - \frac{N}{A} f_3 \tilde{z} e^{(1+A)\tilde{z}/2} + c_5 \{e^{(1+A)\tilde{z}/2} - e^{(1-A)\tilde{z}/2}\}, \quad (\text{A.75})$$

where $K_1^+ = c_5$ is to be determined.

We have up to now six undetermined constants c_i , with $i = \{0, 1, 2, 3, 4, 5\}$. Four of them are to be obtained from the jumps at the flame sheet, while the other two are obtained from the continuity of the solid temperature and heat flux at the flame.

These constants that depends on \tilde{z}_f , N , c and p are lengthy and can be expressed as

$$\begin{aligned} c_0 &= c_0^{(1)} \Delta T + c_0^{(2)}, & c_1 &= -c_1^{(1)} \Delta T + c_1^{(2)}, \\ c_2 &= \frac{(e^{-A\tilde{z}_f} - 1)}{A e^{(1-A)\tilde{z}_f/2}} - c_0 + \Delta T, & c_3 &= -c_0 + \Delta T - \frac{e^{(A-1)\tilde{z}_f/2}}{A}, \\ c_4 &= \Delta T c_4^{(1)} + c_4^{(2)} + S_F E_1 - S_O E_2, \\ c_5 &= \Delta T c_5^{(1)} + c_5^{(2)} + S_F F_1 - S_O F_2, \end{aligned} \quad (\text{A.76})$$

with

$$\begin{aligned} E_1 &= \left(\frac{L_F}{L_O}\right) \frac{(1 - e^{\tilde{z}_f L_O})}{\phi + (1 - \phi)e^{\tilde{z}_f L_O}} \left\{ \frac{(A - 1) e^{(A-1)\tilde{z}_f/2} + (1 + A) e^{-(1+A)\tilde{z}_f/2}}{2A(1 - e^{\tilde{z}_f L_F})} \right\} + \\ &\quad \frac{L_F (1 - e^{-A\tilde{z}_f}) e^{(A-1)\tilde{z}_f/2}}{A(1 - e^{\tilde{z}_f L_F})}, \\ E_2 &= \left\{ \frac{(A - 1) e^{(A-1)\tilde{z}_f/2}}{2A} (1 - e^{-A\tilde{z}_f}) + e^{-(1+A)\tilde{z}_f/2} \right\}, \\ F_1 &= \left(\frac{L_F}{L_O}\right) \frac{1}{\phi + (1 - \phi)e^{\tilde{z}_f L_O}} \left(\frac{1 - e^{\tilde{z}_f L_O}}{1 - e^{\tilde{z}_f L_F}}\right) \frac{(A - 1) e^{(A-1)\tilde{z}_f/2}}{2A} + \frac{L_F e^{(A-1)\tilde{z}_f/2}}{A(1 - e^{\tilde{z}_f L_F})}, \\ F_2 &= \frac{(A - 1) e^{(A-1)\tilde{z}_f/2}}{2A}, \end{aligned} \quad (\text{A.77})$$

where the auxiliary constants $\{c_0^{(1)}, c_0^{(2)}, c_1^{(1)}, c_2^{(2)}, c_4^{(1)}, c_4^{(2)}, c_4^{(1)}, c_4^{(2)}\}$ depend on the problem parameters $A, N, c, \varphi, \tilde{z}_f$ and K . In the limit of $\{N, K\} \rightarrow 0$ we have $A \rightarrow 1$ and $\{c_0, c_1, c_4^{(1)}, c_4^{(2)}, c_5^{(1)}, c_5^{(2)}\} \rightarrow 0$, and its easy to show that we recover the profiles for the gaseous (non-confined) case ².

²One must be careful when taking this limit. If we look to the governing equations in the far-

Leading-order flame position \tilde{z}_f is obtained from the leading-order reactants jump at the flame

$$\frac{1}{L_F} \left[\frac{dY_{F(0)}}{d\tilde{z}} \right] = \frac{1}{\phi L_O} \left[\frac{dY_{O(0)}}{d\tilde{z}} \right], \quad (\text{A.78})$$

and it gives

$$\tilde{z}_f = -\frac{1}{L_O} \log(1 + \phi^{-1}), \quad (\text{A.79})$$

which is the same expression for the non-confined case (CHEATHAM; MATALON, 2000) and it only depends on the Lewis number of the reactant that must diffuse against the incoming mass flux (in this case, oxidant, that is diffusing into the chamber against a mass flux of fuel).

The stoichiometric temperature (associated with complete combustion) is given by

$$T_f^s = \frac{1}{A} + T_{-\infty} + \left(\Delta T e^{(1-A)\tilde{z}_f/2} - \frac{1}{A} \right) e^{A\tilde{z}_f} + c_0 (1 - e^{(1+A)\tilde{z}_f/2}), \quad (\text{A.80})$$

and the parameter γ has the form

$$\gamma = -\frac{1}{A} + (1 + A) \left\{ \left(\frac{e^{(A-1)\tilde{z}_f/2} - \Delta T}{A} \right) + c_0 \right\} e^{(1+A)\tilde{z}_f/2}. \quad (\text{A.81})$$

Again, for the limit of $N \rightarrow 0$, we have that $A \rightarrow 1$ and $c_0 \rightarrow 0$, such that in this limit case of $N \rightarrow 0$ we obtain

$$T_f^s \rightarrow 1 + T_{-\infty} + (\Delta T - 1) e^{\tilde{z}_f}, \quad \gamma \rightarrow -1 + 2(1 - \Delta T) \left(\frac{\phi}{1 + \phi} \right)^{1/L_O}, \quad (\text{A.82})$$

or exactly the expressions for the gaseous case (non-confined) (CHEATHAM; MATALON, 2000). Recovering the gaseous, non-confined results for the limit in which gas and solid phases decouple is an indicative of the consistency of the formulation.

The excess enthalpy functions are given by

$$h_O^* = h_O^{(1)} \Delta T + h_O^{(2)} + S_O G_1 - S_F G_2, \quad (\text{A.83})$$

$$h_F^* = h_F^{(1)} \Delta T + h_F^{(2)} + S_O G_1 - S_F G_3, \quad (\text{A.84})$$

field, we note that the limit $N \ll 1$ only decouples the phases if we consider that $N\Gamma \ll 1$. Since Γ does not appear explicitly in the solutions, as it is the perturbation parameter, the proper way to consider $N\Gamma \ll 1$ would be to jointly with $N \ll 1$ consider $c \gg 1$. The obvious limit would be $c \rightarrow N^{-1}$.

where

$$\begin{aligned}
G_1 &= \frac{(A-1)(1-e^{A\tilde{z}_f})}{2A}, \\
G_2 &= \left(\frac{L_F}{L_O}\right) \left\{ L_O \frac{(1-e^{A\tilde{z}_f})}{A(1-e^{\tilde{z}_f L_F})} - \frac{(1-e^{\tilde{z}_f L_O})}{\phi+(1-\phi)e^{\tilde{z}_f L_O}} \left(\frac{(1+A)+(A-1)e^{A\tilde{z}_f}}{2A(1-e^{\tilde{z}_f L_F})} \right) \right\}, \\
G_3 &= \left(\frac{L_F}{L_O}\right) \frac{(1-e^{A\tilde{z}_f})(A-1)}{\phi+(1-\phi)e^{\tilde{z}_f L_O}} \left(\frac{1-e^{\tilde{z}_f L_O}}{2A(1-e^{\tilde{z}_f L_F})} \right) - \left\{ \frac{L_F(1-e^{A\tilde{z}_f})-A(1-e^{\tilde{z}_f L_F})}{A(1-e^{\tilde{z}_f L_F})} \right\}, \tag{A.85}
\end{aligned}$$

and $h_O^{(1)}, h_O^{(2)}, h_F^{(1)}, h_F^{(2)}$ depends on $A, N, c, \varphi, \tilde{z}_f$ and K . In the limit $N \rightarrow 0$ (together with $c \rightarrow 1/N$, as argued previously), we have $A \rightarrow 1$ and $\{h_O^{(1)}, h_O^{(2)}, h_F^{(1)}, h_F^{(2)}\} \rightarrow 0$, and again it's easy to show that we recover the expressions for the excess enthalpy for the gaseous (non-confined) case (CHEATHAM; MATALON, 2000; KUKUCK; MATALON, 2001; METZENER; MATALON, 2006).

Evaluating the expression for the correction of the flame position, Eq. A.14, we obtain

$$\eta_f = \eta_f^{(1)} \Delta T + \eta_f^{(2)} + S_O - \left(\frac{L_F}{L_O}\right) \frac{S_F}{\phi+(1-\phi)e^{\tilde{z}_f L_O}} \left(\frac{1-e^{\tilde{z}_f L_O}}{1-e^{\tilde{z}_f L_F}} \right), \tag{A.86}$$

where $\eta_f^{(1)}$ and $\eta_f^{(2)}$ depends on \tilde{z}_f, N, c and p . The heat exchange between phases modifies the flame position through the leakage functions S_F, S_O and through the parameters $\eta_f^{(1)}, \eta_f^{(2)}$. For the limit $N \rightarrow 0$, we have $\{\eta_f^{(1)}, \eta_f^{(2)}\} \rightarrow 0$, such that we recover the result for the gaseous (non-confined) case.

In the next section we analyze the Burke-Schumann limit (leading-order solutions) in order to show how the porosity and heat exchange affects the leading-order features of the flame.

A.4 Burke-Schumann limit

In the limit of infinitely high δ we have no leakage of reactants through the flame sheet and the flame has its highest temperature, T_f^s (stoichiometric temperature). We considered $\Delta T = 0$, $Y_{F-\infty} = 0.4$, $Y_{O0} = 0.21$ and $\phi = 1.2$ for plotting the profiles. Lewis numbers were considered as $L_F = 0.96$ and $L_O = 1.01$. It is worth to note that in the gaseous (non-confined) case, the injection velocity does not influence the leading-order problem, as its influence appears only on the Damkohler number. However, in the present case it affects N and K , the heat exchange between gas and solid and the heat loss at the top of the chamber, respectively. Hence, it affects the Burke-Schumann solution as shown ahead.

In the far-field region, the temperatures are at thermal equilibrium up to $O(1)$, and no chemical reaction occurs since $Y_O = 0$, $Y_F = 1$. The leading-order temperature profiles in the far-field is shown in Fig. A.3

In a region of the order of $O(\Gamma^{-1})$ from the top of the chamber, consumption of reactants occurs and gas and solid are no longer at thermal equilibrium. The gas temperature peaks at the flame sheet. Temperatures and mass fraction profiles in the convective-diffusive region are shown in Fig. A.4.

The influence of the porosity on the stoichiometric temperature T_f^s , solid temperature at the flame T_{sf} (which is the same as the solid temperature at the top of the chamber) and the parameter γ (ratio of the excess heat conducted to one side of the reaction sheet to the total heat generated in the reaction zone) is shown in Fig. A.5.

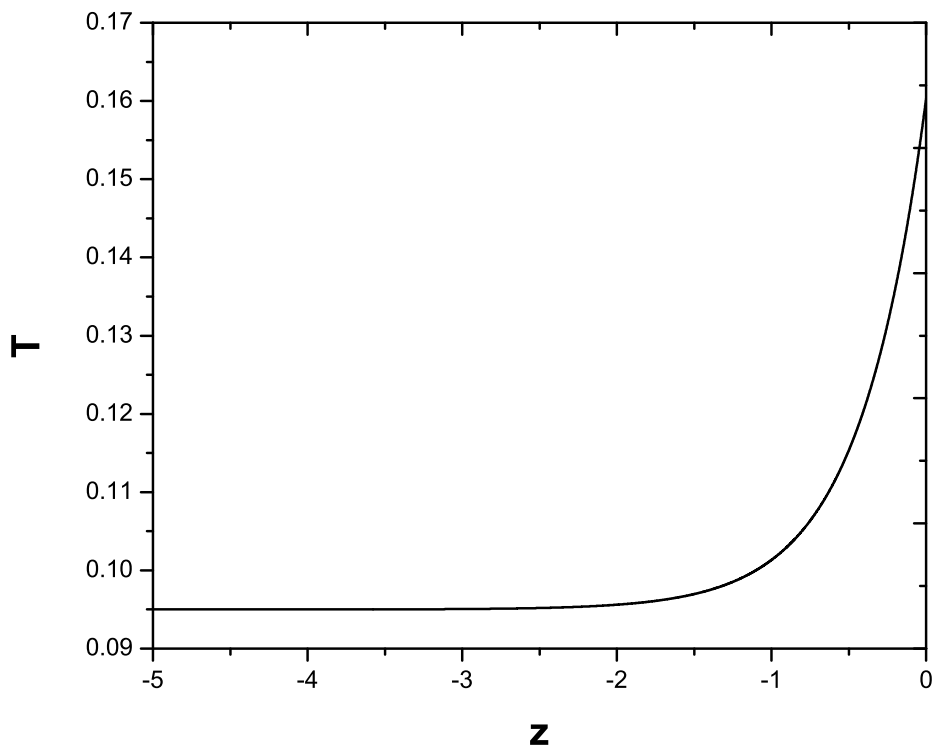


Figure A.3 - Temperature profiles in the far field.

Even though for high porosities the heat loss is high, the small heat exchange between phases does not allow a high decrease of the flame temperature, as it can be seen in Fig. A.6.

For an increase on the injection velocity³, we have a decrease on the heat exchange and heat loss, which results in a higher stoichiometric temperature. In Fig. A.7 we can see that the stoichiometric temperature approaches asymptotically the flame temperature T_{fg} for the gaseous, non-confined case, as shown previously. The parameter γ also tends asymptotically to its value for a non-confined problem. It is interest to note that differently from the gaseous, non-confined case, the injection velocity affects the Burke-Schumann solution through N and K .

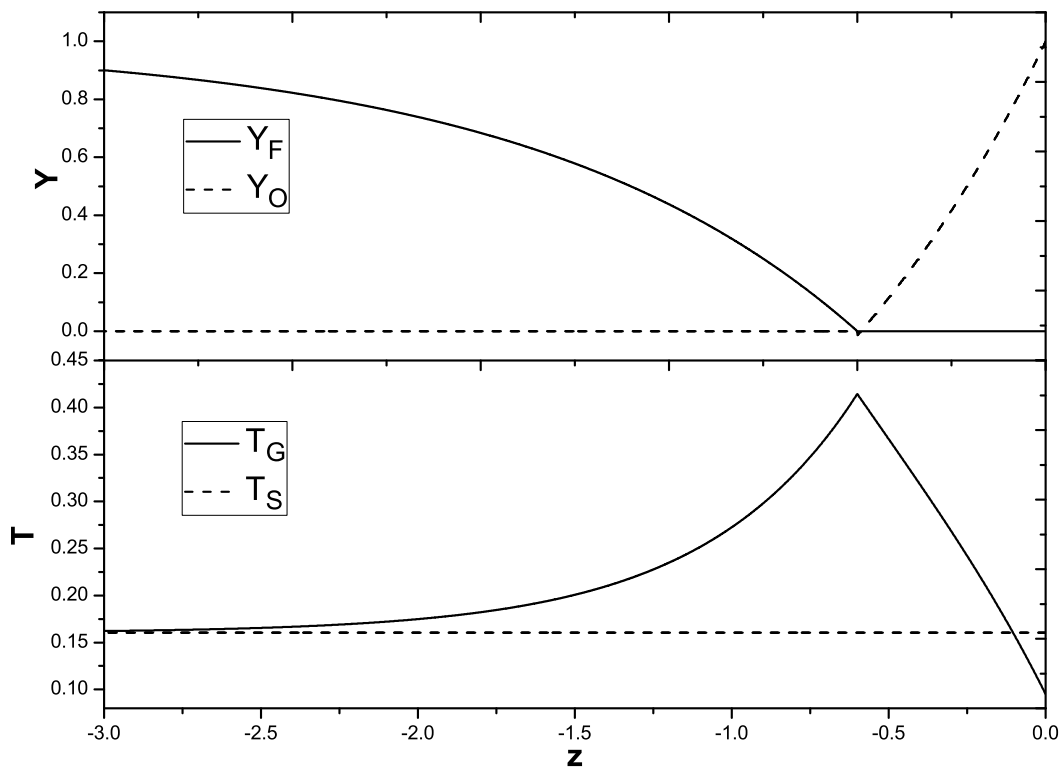


Figure A.4 - Profiles in the consumption zone.

³The dimensionless injection velocity is given by $N^{1/(m'-2)}$, as seen from the model used for N .

A.5 Reactant leakage curves

In this section we present the fuel and oxidant leakage curves S_F and S_O , respectively, based on the formulation presented earlier. Since the injection velocity modifies the Burke-Schumann solution, it also modifies γ . Hence, one must be careful when obtaining the reactants leakage curves that characterizes extinction for this flame, as the expressions of S_F and S_O are different for each γ , as one can see from Eqs. A.18 to A.21.

For each δ we have two different solutions, one associated with a more intense burning state (higher temperature) and the other associated with increasingly high leakage of reactants (lower temperature). Below δ_c we have no solutions, and hence δ_c represents the state of flame extinction. We utilize the expressions for S_F and S_O presented earlier and analyze how the porosity and the injection velocity (heat exchange) affects the flame extinction. We point to the fact that the injection velocity modifies not only the Damkohler number D , but also N and K , affecting the extinction of this flame in a more complex way when compared with the gaseous, non-confined, case.

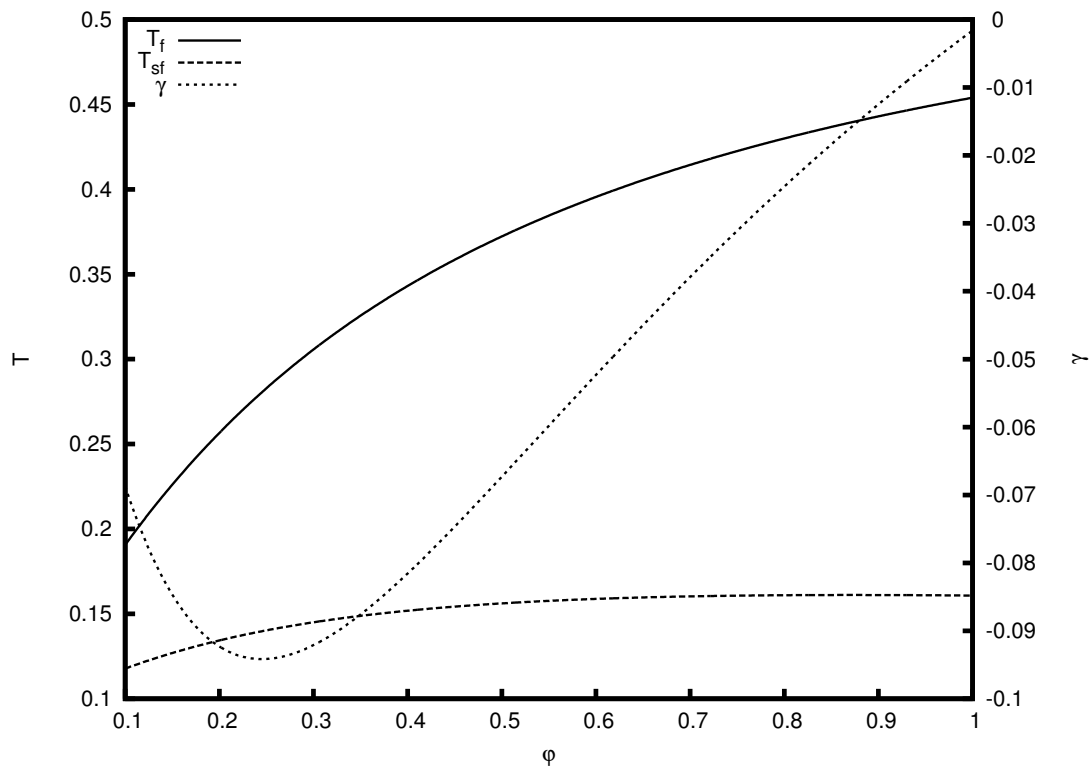


Figure A.5 - Porosity influence.

In Fig. A.8 we show the influence of the porosity φ on the leakage curves S_F and S_O (for $\bar{V} = \{20, 100, 500\} \text{ mm/s}$ ⁴) close to extinction. We also show the variation of γ and η_f with respect to φ in Fig. A.9. If the porosity is low enough, the heat removal from the flame through the solid matrix decreases flame temperature, which increases the leakage of reactants, and eventually leads to extinction. The reactant that is more consumed close to extinction depends on the value of the injection velocity, as one can see from Figs. A.8 and A.9. For instance, when $\bar{V} = 20 \text{ mm/s}$, $\gamma < 0$ everywhere, including at the extinction point $\varphi_{ex} \sim 0.46$. Then, in this case the more consumed reactant close to extinction is the fuel, which makes the flame to shift to the oxidant side. In the case in which $\bar{V} = 500 \text{ mm/s}$, $\gamma > 0$ everywhere, including at the extinction point $\varphi_{ex} \sim 0.33$. Then, in this case the more consumed reactant close to extinction is the oxidant, which shifts the flame to the fuel side.

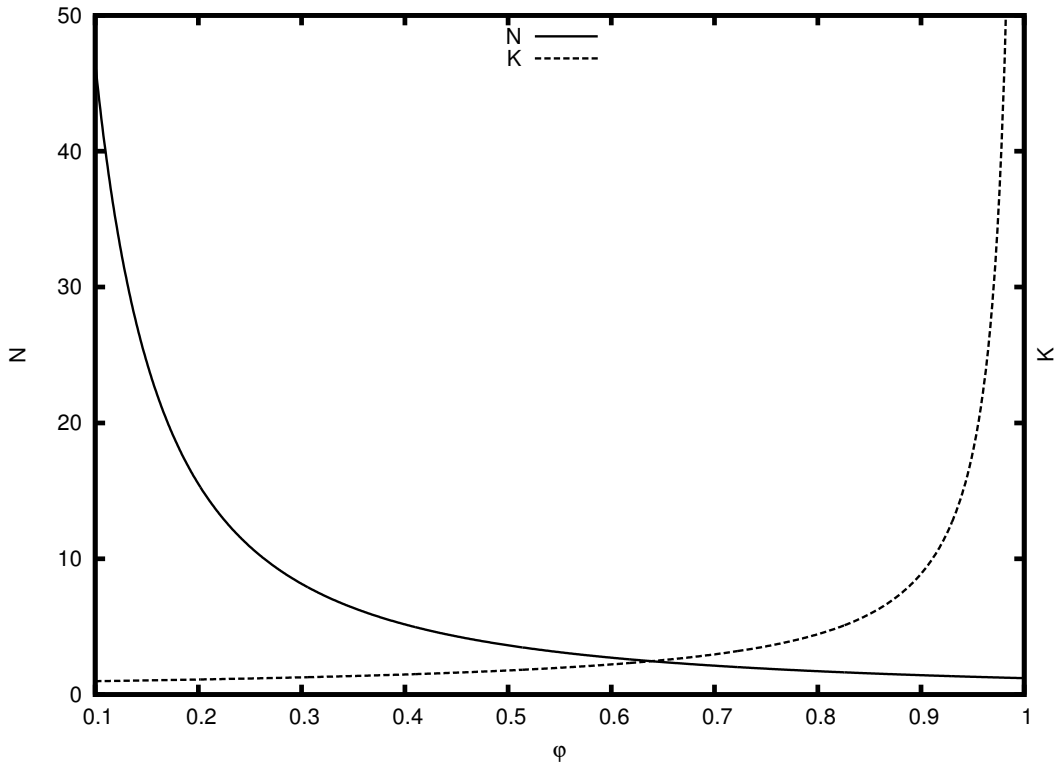


Figure A.6 - $\{N, K\} \times \varphi$.

As we increase the injection velocity \bar{V} from 20 mm/s to 500 mm/s the extinction

⁴Note that since N varies with φ , we can not fix a dimensionless injection velocity to different values of φ , hence, we fix the dimensional injection velocity \bar{V} instead.

porosity decreases and then increases. In a non-confined problem, an increase on the injection velocity only decreases the Damkohler number. One could expect that a similar behavior would occur for the confined case, but that is not the case. In the present case, increasing the injection velocity first increase the Damkohler number up to a maximum (as opposed to what happens in a non-confined problem), and further increasing the injection velocity decrease the Damkohler number. Since for low \bar{V} we have a high value of the interphase heat exchange N , the intense heat transfer between gas and solid decreases the stoichiometric flame temperature T_f^s , which decreases exponentially the reactive Damkohler number D (from A.17, $D \sim e^{-T_a/T_f^s}$). These features may be seen in Fig. A.10, where we show T_f^s and D as a function of \bar{V} for $\varphi = 0.7$.

The influence of the dimensionless injection velocity $N^{1/(m'-2)}$ on the reactants leakage is presented in Fig. A.11 with $\varphi = 0.7$, while in Fig. A.12 we present γ and η_f variations with respect to the dimensionless injection velocity (as no porosity variation is considered here, the dimensionless velocity $V \equiv N^{1/(m'-2)}$ may be used). It can be seen that the flame presents high leakage of reactants for both low and high values of the injection velocity (Fig. A.13 show the low-velocity extinction point, while Fig. A.14 show the high-velocity extinction point).

For the lower extinction point (low injection velocity and high heat exchange), more heat is conducted from the flame sheet towards the fuel side, such that fuel is the more consumed reactant, while for the higher extinction point (high injection velocity and low heat exchange) the opposite holds, as seen in Figs. A.13 and A.14. For $N \rightarrow 0$, γ tends to its value on the gaseous, non-confined case, as shown in a previous section. For high porosities, such that $p = O(\Gamma^{-1})$, it can be shown that the low extinction point (low injection velocity and high heat exchange) may be eliminated. In other words, in this case, the flame supports higher amounts of heat loss. However, when $N = O(\epsilon^{-1}) \gg 1$ the formulation breaks down, as the heat exchange now occurs in the reaction region, and in this case the jumps at the flame sheet must be modified, as the flame structure equations must consider the gas-solid heat exchange.

It is interest to point that the existence of two extinction points was observed earlier in the gaseous, non-confined case, when a finite chamber was considered (MATALON et al., 1979; MATALON; LUDFORD, 1979), with a lower boundary through which gaseous fuel was injected. In those works, when the fuel injection rate was low enough, the flame was established close to the lower boundary, allowing high heat losses, such

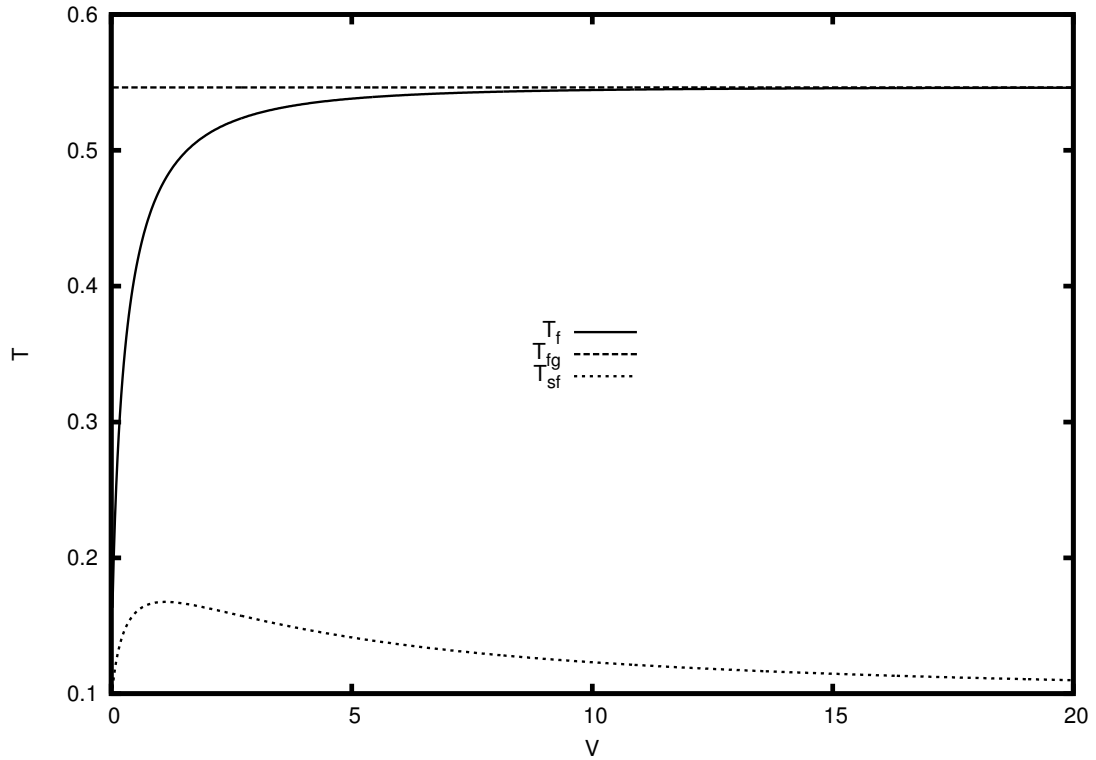


Figure A.7 - $\{T_f, T_f^g, T_{sf}\} \times \bar{V}$.

that a low extinction point was possible. However, for the semi-infinite chamber such second extinction point is not observed.

More generally, the existence of two-extinction points is observed when heat losses are present. The possibility of an upper and lower bound for D for extinction was proposed by Tien (1986) (for a stagnation-point flow) and Sibulkin (1988) (for a free-convection diffusion flame), but their works considered radiation from the condensed-phase surface. It was then shown the existence of the dual extinction points in the analyses of Chao et al. (1990) and Chao and Law (1993). In those theoretical works, it was shown that when the stretch rate is small, the flame thickness increases, promoting radiative losses by the flame. If the stretch rate is low enough, the excessive heat loss leads to flame extinction. This analysis was later extended by Wang et al. (2007) to consider non-unity Lewis number.

In the present case, starting from the high extinction point (associated with kinetic extinction), D increases and after reaching a maximum, decreases, reaching the extinction point associated with heat loss at a low value of D (instead of a high, as seen in previous works). The lowering on D for low injection velocities is an effect

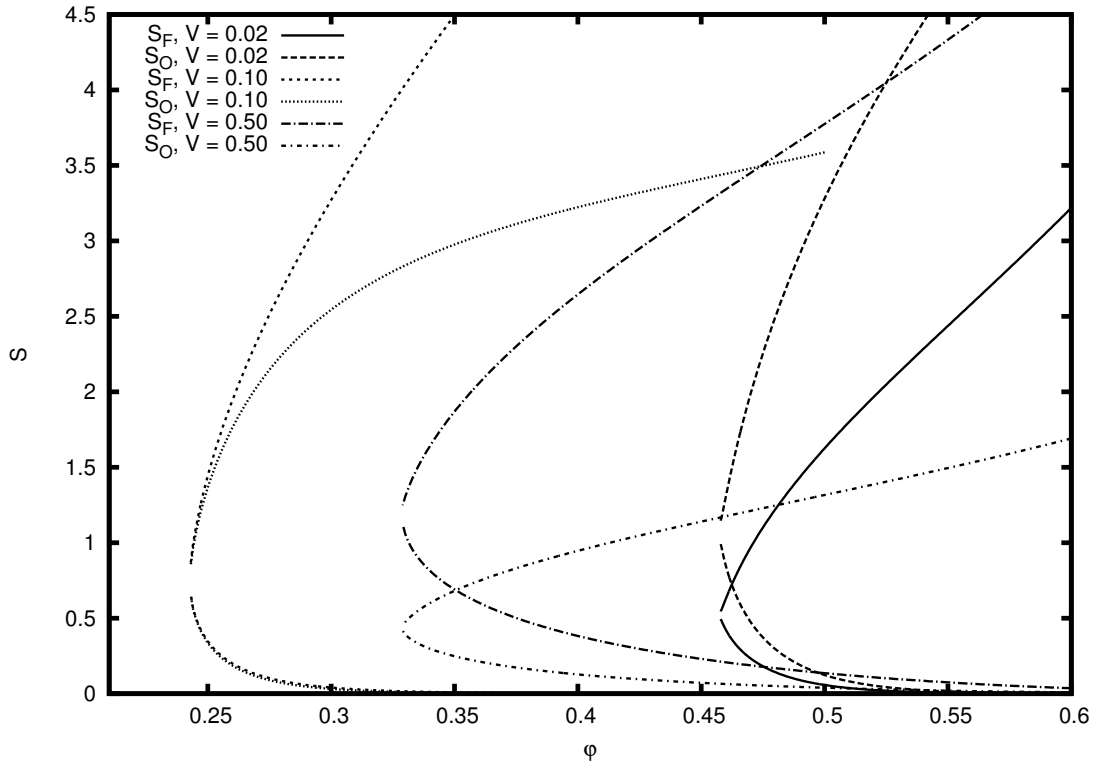


Figure A.8 - Reactants leakage $\times \varphi$ for $\bar{V} = 20, 100, 500 \text{ mm/s}$.

of the decrease of T_f^s .

If conditions are such that the flame can support high amounts of heat exchange, there is $O(1)$ leakage of reactants through the sheet and the flame falls into Liñan's premixed flame regime (LIÑAN, 1974), such that a different asymptotic treatment is required). When $N = O(\epsilon^{-1})$ the formulation breaks down, because in this case we must consider heat exchange in the reaction region.

A.6 Conclusions

In this Appendix we performed an asymptotic analysis of the extinction limits of a diffusion flame established in an inert porous chamber. The asymptotic limit of $\Gamma \gg 1$ was considered, such that in addition of the two usual length-scales of interest (convection-diffusion region, where no chemical reaction takes place, and a diffusive-reactive region, where all the heat is released by the exothermic reaction), an additional region arises: a far-field where heat conduction through the solid phase balance heat convection through the gas-phase. The general formulation derived by Cheatham and Matalon (2000) for the structure of diffusion flames was applied in

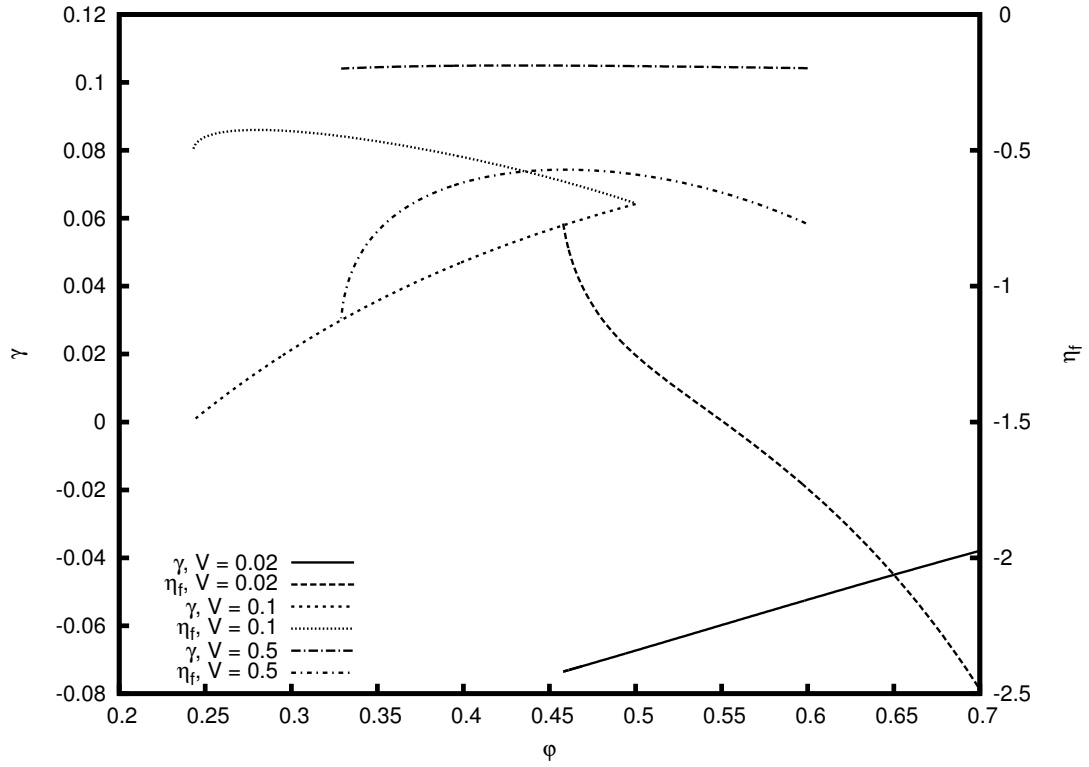


Figure A.9 - $\{\gamma, \eta_f\} \times \varphi$ for $\bar{V} = 20, 100, 500 \text{ mm/s}$.

order to obtain curves for the leakage of reactants. The influence of porosity and injection velocity (interphase heat exchange) on the extinction limits of this flame is analyzed.

It is important to emphasize that in this analysis we considered an empirical model for h , but in the remaining Chapters of this work we fix a N instead (independent of the flow velocity). We use a more precise model in this Appendix because of the simplicity of the flow field (constant injection velocity), in contrast to the more complicated flow field in the other Chapters.

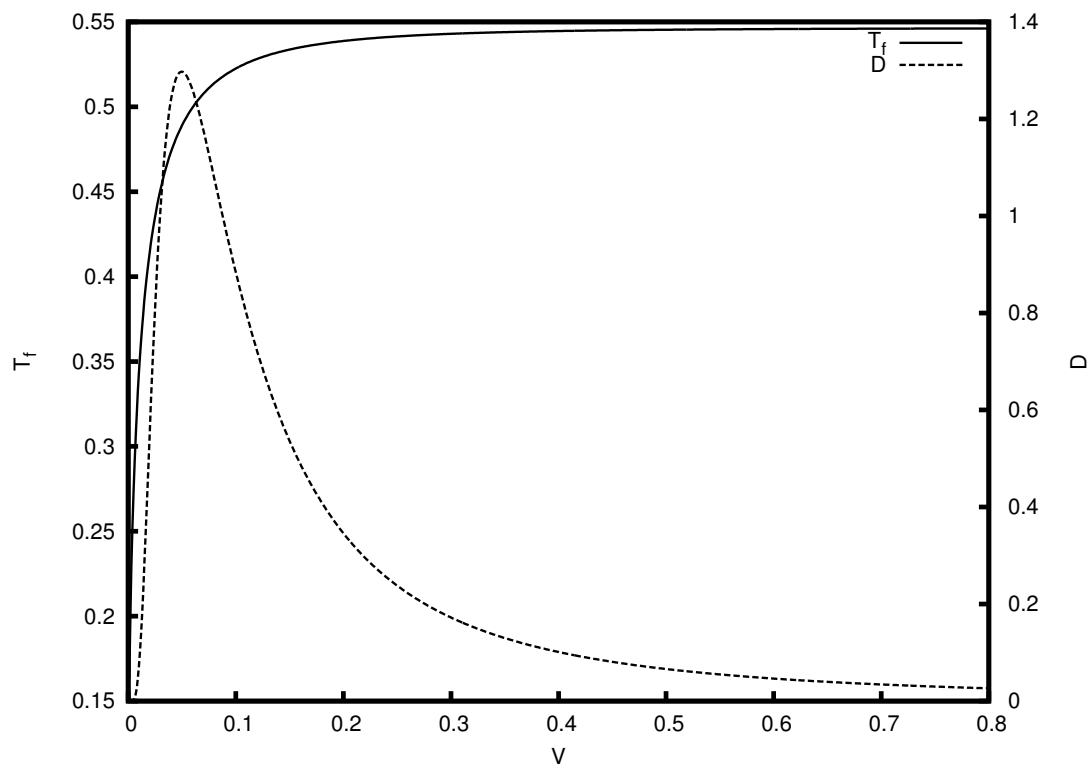


Figure A.10 - $\{T_f, D\} \times \bar{V}$ for $\varphi = 0.7$.

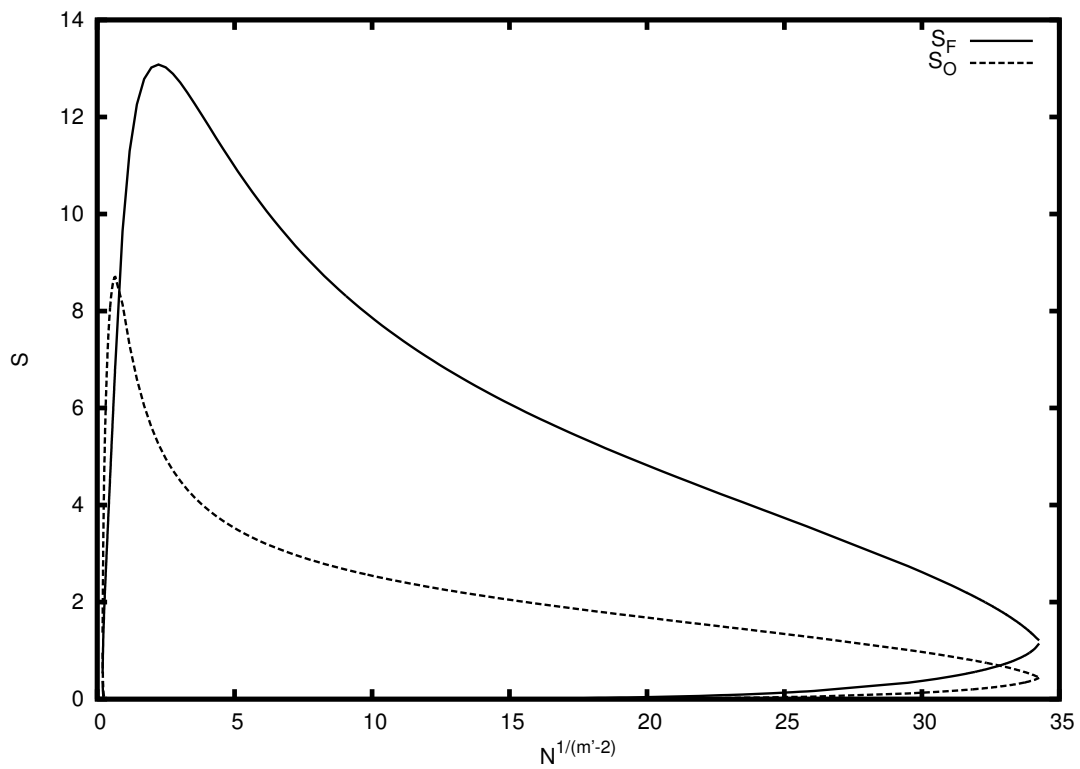


Figure A.11 - Reactants leakage $\times N^{1/(m'-1)}$.

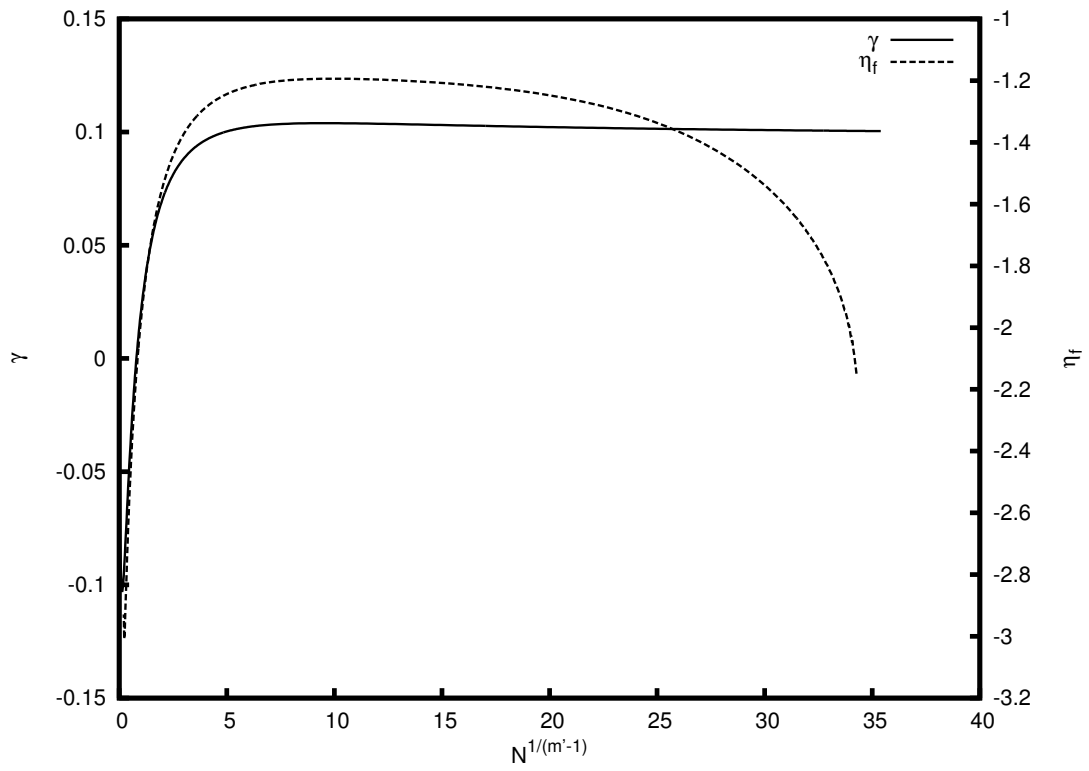


Figure A.12 - $\{\gamma, \eta_f\} \times N^{1/(m'-1)}$.

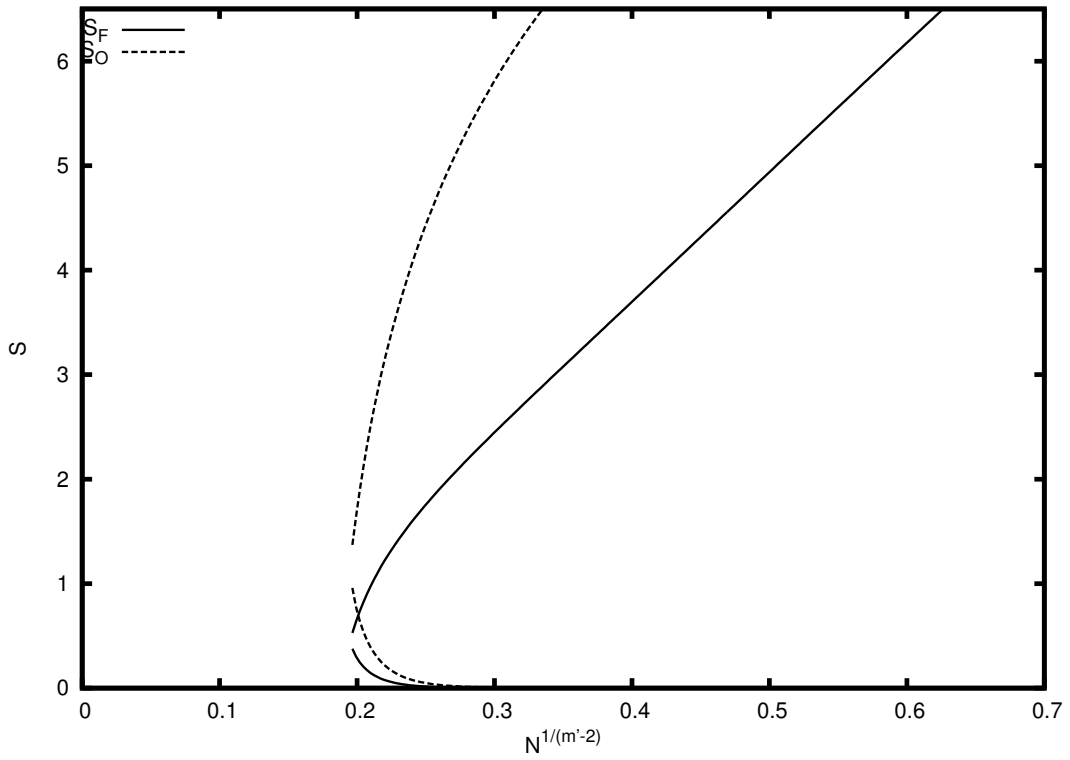


Figure A.13 - Low-velocity extinction points.

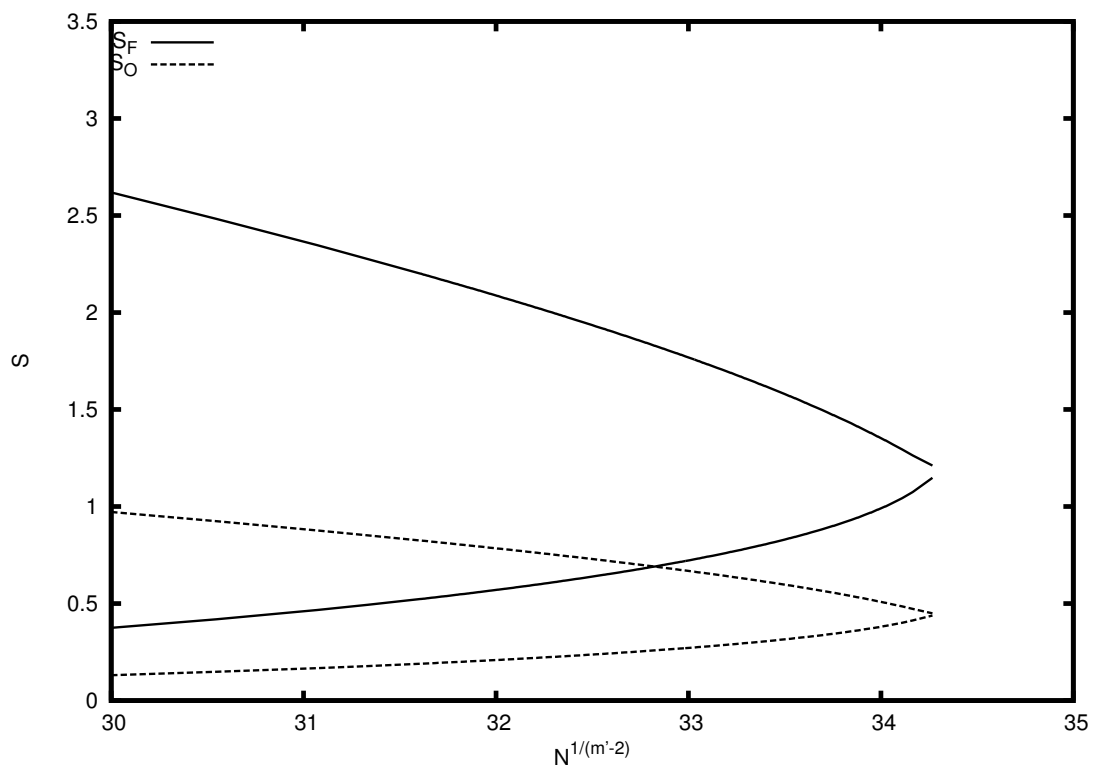


Figure A.14 - High-velocity extinction points for $N^{1/(m'-1)}$.

PUBLICAÇÕES TÉCNICO-CIENTÍFICAS EDITADAS PELO INPE

Teses e Dissertações (TDI)

Teses e Dissertações apresentadas nos Cursos de Pós-Graduação do INPE.

Manuais Técnicos (MAN)

São publicações de caráter técnico que incluem normas, procedimentos, instruções e orientações.

Notas Técnico-Científicas (NTC)

Incluem resultados preliminares de pesquisa, descrição de equipamentos, descrição e ou documentação de programas de computador, descrição de sistemas e experimentos, apresentação de testes, dados, atlas, e documentação de projetos de engenharia.

Relatórios de Pesquisa (RPQ)

Reportam resultados ou progressos de pesquisas tanto de natureza técnica quanto científica, cujo nível seja compatível com o de uma publicação em periódico nacional ou internacional.

Propostas e Relatórios de Projetos (PRP)

São propostas de projetos técnico-científicos e relatórios de acompanhamento de projetos, atividades e convênios.

Publicações Didáticas (PUD)

Incluem apostilas, notas de aula e manuais didáticos.

Publicações Seriadas

São os seriados técnico-científicos: boletins, periódicos, anuários e anais de eventos (simpósios e congressos). Constam destas publicações o Internacional Standard Serial Number (ISSN), que é um código único e definitivo para identificação de títulos de seriados.

Programas de Computador (PDC)

São a seqüência de instruções ou códigos, expressos em uma linguagem de programação compilada ou interpretada, a ser executada por um computador para alcançar um determinado objetivo. Aceitam-se tanto programas fonte quanto os executáveis.

Pré-publicações (PRE)

Todos os artigos publicados em periódicos, anais e como capítulos de livros.